


Summer 7-15-2019

Searching for Supermassive Binary Black Holes and their Gravitational Waves

Karishma Bansal
University of New Mexico

Follow this and additional works at: https://digitalrepository.unm.edu/phyc_etds

 Part of the [External Galaxies Commons](#), [Physics Commons](#), and the [Stars, Interstellar Medium and the Galaxy Commons](#)

Recommended Citation

Bansal, Karishma. "Searching for Supermassive Binary Black Holes and their Gravitational Waves." (2019).
https://digitalrepository.unm.edu/phyc_etds/215

This Thesis is brought to you for free and open access by the Electronic Theses and Dissertations at UNM Digital Repository. It has been accepted for inclusion in Physics & Astronomy ETDs by an authorized administrator of UNM Digital Repository. For more information, please contact amywinter@unm.edu.

Karishma Bansal

Candidate

Physics and Astronomy

Department, The University of New Mexico

This dissertation is approved, and it is acceptable in quality and form for publication:

Approved by the Dissertation Committee:

Dr. Greg Taylor, Chair

Dr. Kevin Stovall

Dr. Rouzbeh Allahverdi

Dr. Edl Schamiloglu

Defended June 21, 2019.

Searching for Supermassive Binary Black Holes and their Gravitational Waves

by

Karishma Bansal

Dual B.S.—M.S., Indian Institute of Science Education & Research,
Pune, 2014

M.S., University of New Mexico, 2018



DISSERTATION

Submitted in Partial Fulfillment of the
Requirements for the Degree of

Doctor of Philosophy
Physics

The University of New Mexico

Albuquerque, New Mexico

July, 2019

©2019, Karishma Bansal

All rights reserved except where otherwise noted

Dedication

To my parents

who didn't clip my wings for being a girl.

Acknowledgments

This dissertation would have never been possible without all the supports from my family, friends, and mentors.

First of all I would like to thank my supervisor Greg Taylor for constantly motivating and supporting me this entire time. From Greg, I have learned a great deal about managing time, writing papers, and most importantly, how to be a good researcher. He would always encourage me to work independently and develop my own ideas. I admire his diligence and willingness to guide his students. He was always there to guide me and help me when I felt stuck. Greg, I would be greatly indebted for your time and effort.

I would like to thank Kevin Stovall for teaching me many valuable skills for my work on pulsars. He was always there to address my concerns and patiently help me sort them out. I really enjoyed having discussion with him about work or science in general. It has been my pleasure working with him and having him as my mentor.

I am very grateful to Jayce Dowell, to whom I would run to get help with debugging my code or any other technical issue that needed to be addressed. I really admire his ability to tackle problems and his thoughtful suggestions for handling them.

When I joined UNM, I really lacked on writing skills. I wouldn't say that I have mastered it all but thanks to all my mentors and collaborators for their tremendous effort to help me become better at it. In this list, I would like to include my best friend Shreya Ray for introducing me to books outside academia and intriguing my interest in writing.

Of course, this thesis would be incomplete without mentioning my great friends who have been there to relieve my stress and helped me have a life beyond work. Rashmi, Pallavi, and Tanya - thank you all for bearing with me and lending me your ears when I needed to vent. Anirban and Gopi, who I have known since my first day at UNM. Thank you for hosting many amazing parties and enduring my craziness during this time. Anupam and Sayonee, thank you so much for being there for me and offering your place to stay. Savin, Akram, Megan, Satomi, Anastasia, Monica - who made my life in grad school smoother. I would also like to include my non-UNM friend - Matt, for his great help with cleaning my job applications and discussing about life in general. It has been wonderful to have you all as a part of my life.

I would like to give a big round of applause to all the organizers of Astronomy on Tap-Abq. It has been so much fun organizing the events with you all. A special thanks to Mark Gorski, who took this initiative and invited me to be a part of it. It has been an amazing experience having a platform to share my passion for astronomy with the general audience.

Alisa Gibson - Thank you so much for all the paperwork and administrative support. Michael - for helping with the conferences and getting reimbursements.

I would like to acknowledge the never ending support and love of my parents Dinesh Bansal and Pushpa Bansal. They have always pushed me to work harder and achieve higher goals in life. I cannot thank them enough for not stopping me from coming to the USA, when everyone else told them to do so, just because I am girl. My brothers - Rahul and Golu, for their love and constantly keeping in touch with me. I would like mention my Grandma, who passed away three years ago, for all the amazing stories when I was a little kid. I miss you Amma! Lastly, I would like to thank my partner and my closest friend, Kaleb Campbell, for his love and support. He has been very patient with me and comforted me when going got tough.

Thank you everyone!

Searching for Supermassive Binary Black Holes and their Gravitational Waves

by

Karishma Bansal

Dual B.S.—M.S., Indian Institute of Science Education & Research,

Pune, 2014

M.S., University of New Mexico, 2018

Ph.D., Physics, University of New Mexico, 2019

Abstract

The recent discovery of gravitational waves (GWs) by the LIGO collaboration has opened a new observing window on the universe, but it is limited to the GWs in the frequency range of 10 – 1000 Hz. The main motivation of this thesis is to consider the possibility of detecting low frequency (nHz) GWs. In the pursuit of these waves, we need to find their source of origin and build a detector with the required sensitivity. Low-frequency waves are expected as a result of coalescing binary supermassive black holes (SMBBHs). We hope to detect these waves in the near future using pulsar timing arrays (PTAs). Thus, this thesis can be divided into two parts: searching for SMBBHs and using pulsars for improving the sensitivity of PTAs.

SMBBHs are expected to form as a result of galaxy mergers. However, despite numerous attempts, so far we have been able to find only a handful of these systems. This raises various questions about the merger rate, the timescale of a merging process, and the sensitivity and resolving power of the available instruments. 0402+379 is the most compact confirmed SMBBH, with two compact cores at a separation of 7.3 pc.

We have studied this source at 5, 8, 15 and 22 GHz using the Very Long Baseline Array (VLBA) over a timeline of 12 years. With some assumptions about the orbit, we measure the orbital period $P \approx 28000$ years and SMBBH mass $M \approx 15 \times 10^9 M_{\odot}$. A strong frequency-dependent core shift is evident, which we use to infer magnetic fields near the jet base. Subsequently, we search for more compact SMBBHs so that we can study their orbital motion within our lifetime. We select a sample of 18 sources from the VLBA imaging polarimetry survey based on their morphology and host galaxy properties. We also include NGC7674, which was recently claimed to be an SMBBH candidate. We observe these sources at multiple frequencies using the VLBA.

PTAs consist of a large array of pulsars which are being used to detect the GWs. However, when the signal from a pulsar traverses the interstellar medium (ISM), its signal gets affected, contributing to PTA noise. In order to improve the sensitivity of PTAs, it is necessary to understand the properties of the ISM. The main effects of the ISM are dispersion, scattering, and scintillation. All these effects are strongly dependent on frequency such that they have a large impact at lower frequencies. Hence, in order to study these effects, we study a sample of eight pulsars at frequencies below 100 MHz using the Long Wavelength Array. This provides us with insights into the distribution of inhomogeneities in the ISM which we hope will help in improving the sensitivity of PTAs.

Contents

List of Figures	xiii
List of Tables	xix
List of Acronyms	xx
1 Introduction	1
1.1 Pulsars	2
1.1.1 Pulsar Energetics	2
1.1.2 Pulsar statistics	4
1.1.3 Pulsar Profile Properties	6
1.2 Interstellar medium	7
1.2.1 Dispersion	8
1.2.2 Scattering	10
1.2.3 Scintillation	13
1.2.4 Deviation from the thin-screen model	16
1.3 Low frequency Gravitational Waves	17
1.3.1 Supermassive Binary Black Holes	18

<i>Contents</i>	x
1.3.2 Pulsar Timing	20
1.4 Thesis Outline	23
2 Constraining the Orbit of SMBBH 0402+379	25
2.1 Introduction	26
2.2 Observations and Data Reduction	29
2.2.1 VLBA Observations	29
2.3 Measurement and Fits	30
2.3.1 Analysis	31
2.3.2 Magnetic Field Estimate	34
2.3.3 Orbital Models	35
2.3.4 Comments on the resolved SMBBH Population	38
2.4 Conclusion	39
3 A Search for Compact Supermassive Black Holes	52
3.1 Introduction	52
3.2 Candidate Selection	54
3.3 Observations and Data Reduction	54
3.4 Results	55
3.4.1 NGC7674	56
3.4.2 J1256+5562	57
3.5 Conclusion and Future Work	58
4 Scattering study of Pulsars below 100 MHz using LWA1	62

<i>Contents</i>	xi
4.1 Introduction	63
4.2 Observations	66
4.3 Analysis	68
4.3.1 Intrinsic Pulse Model	68
4.3.2 Pulse Broadening	70
4.3.3 DM Variation	73
4.4 Results	74
4.4.1 PSR B0329+54	74
4.4.2 PSR B0823+26	75
4.4.3 B0919+06	77
4.4.4 PSR B1822−09	78
4.4.5 B1839+56	80
4.4.6 B1842+14	81
4.4.7 B2217+47	82
4.5 Discussion & Conclusion	83
4.5.1 Scattering Spectral Index Distribution	84
4.5.2 Deviation from theoretical models	85
4.5.3 Time Evolution of Scattering parameters	87
4.6 Summary	89
4.7 Acknowledgements	90
5 Detection of Echoes in PSR B1508+55 using the LWA1	91
5.1 Introduction	91

<i>Contents</i>	xii
5.2 Observations and Data reduction	93
5.2.1 Average pulse profile evolution	94
5.2.2 DM Evolution	96
5.3 Variation in PSR B1508+55	96
5.3.1 Profile Evolution	98
5.3.2 DM Variation	100
5.4 Discussion	101
5.4.1 Properties of ISM structure	104
5.5 Conclusion	105
6 Conclusions and Future Work	107
6.1 Summary	107
6.2 Future Work	109
6.2.1 Search for SMBBHs	109
6.2.2 Role of Magnetic Field	109
6.2.3 Science at Low Frequencies	110
References	112

List of Figures

- 1.1 A toy model for pulsar emission and its magnetosphere: The radio emission originates from the magnetic poles in two narrow beams. It is caused by open field lines originating from the polar caps. The magnetosphere co-rotates with the pulsar within the light cylinder. Adapted from Lyne (2006). 3
- 1.2 $P - \dot{P}$ diagram. This figure shows the entire population of pulsars. It is evident from the plot that there are two types of pulsar population: the central region shows normal pulsars and the bottom left shows MSPs. Using their spin period (P) and spin period derivative (\dot{P}), their magnetic field strength on the surface, their age, and their spin-down energy can be obtained. The shaded region denotes the pulsar graveyard and its boundary is the death line. Credit: Michael Lam 5
- 1.3 The upper panel contains the average profile of PSR B0950+08. The lower panel shows the delay in pulse with decreasing frequency caused due to the dispersion effect. The phase delay wraps around four times indicating a strong effect at the observed frequency of 79.2 MHz. Credit: K. Bansal 9

1.4 Schematic of the interaction of pulse signal with the ISM: A pulsar emits spatially coherent EM radiation which interacts with the scattering screen at a distance of D_s from the pulsar. The scattering angle is a , which denotes the phase deviation in the straight line path of a ray caused due to scattering. The angle of observation (θ is the angular width of the source. As the distance to the pulsar is large ($D \sim \text{kpc}$), these angles (θ, a) are small. Credit: M. Meyer 11

1.5 This plot shows variation in pulse profile broadening with frequency for PSR J0742-2822. As we go towards the lower frequencies, the amount of scattering increases which results into a broadened profile. Here, due to high scattering, the profile becomes undetectable below 148.5 MHz. Adapted from [Kirsten et al. \(2019\)](#) 13

1.6 Interstellar Scintillation: The top panel is a dynamic spectrum for PSR B1133+16 and the bottom panel consist of their autocorrelation functions. It was observed with the Arecibo Observatory at 432 MHz. These plots have been adapted from [Stinebring et al. \(2019\)](#). 14

1.7 This figure shows the entire GW spectrum. The vertical axis indicates the amplitude of h of each expected GW which are observed by a different observatory depending on their frequency. The ground-based observatory is LIGO which made its first discovery in 2015. There are space-based interferometers which are supposed to operate in the 2030s. Detection of GW from PTAs is still in progress and hope to have detection in the early 2020s. Credit: North American Nanohertz Observatory for Gravitational Waves (NANOGrav) 18

1.8 Hellings and Downs curve for isotropic and stochastic GW background as a function of the angle between pulsars and the Earth ([Jenet and Romano, 2015](#)). 22

- 2.1 Naturally weighted 2015.43 VLBA maps of 0402+379 at 5, 8, 15 and 22 GHz. Designated C1 and C2, are the core components in 0402+379 (Maness et al., 2004, Rodriguez et al., 2006). Contours are drawn beginning at 0.15σ (a), 1σ (b), 1σ (c) & 1.5σ (d), and increase by a factor of 2 thereafter. (a) Note that the core components are slightly resolved here. There is a bridge between these two components, and we believe this is a jet emanating from C1, as has been discussed in this paper. (b) A jet emerging from C2, moving in the direction of hotspots can be identified here clearly. We have used this map to obtain the jet-axis angle. (c) A very faint jet emanating from C2, similar to 8 GHz map, can be seen here. (d) No jets are visible at this frequency. 46
- 2.2 We have plotted projected relative RA *vs.* DEC of component C2 with respect to C1 (at origin), at 5 GHz (c's), 8 GHz (x's), 15 GHz (u's), and 22 GHz (k's). This is the raw, uncorrected, modelfit positions. An offset in position with frequency can be seen due to the core-shift effect discussed in the text. 47
- 2.3 Position of C2 relative to C1 in time after removing the effect of the core shift. The black line is a proper motion fit; the best fit positions at each epoch are labeled by points along the line. 48
- 2.4 Plot of the core-shift measurement in distance from the central engine for 0402+379 as a function of frequency. Black circles are observed distance offset from estimated infinite frequency core position at each frequency, and the black solid curve is the fitted function, with $r_c = a(\nu^{(-1/k)})$ (See Table 2.5). 49
- 2.5 Orbital solutions for mass (red) and period (blue) as a function of inclination angle. Points mark solutions with the projected PA given by the label numbers (in degrees North through East). 50

2.6	Circular orbit fits for the four PA values marked in figure 5. All are consistent with the observed offset and proper motion (red). The mass, period and relative radial velocity for the solutions for each PA value are listed in the figure.	51
3.1	VLBA images of MRk231 at 15 GHz (a) and 22 GHz (b). Contours are drawn beginning at level 1σ and increasing by a factor of 2 thereafter. The data have been weighted with natural weighting scheme.	59
3.2	VLBA images of MRk231 at 2.3 GHz (left) and 5 GHz (right). Contour levels are the same multiples of the lowest contour. In both the maps, there are two lobes along the North-South direction and a central bright component. This figure has been adapted from Ulvestad et al. (1999).	60
4.1	Fitting example for B2217+47 epoch MJD 57372. Top to bottom plots show fitting of intrinsic pulse models convolved with an exponential scattering function to the observed data. For B2217+47, the noise in the data increases as we go towards the lower frequencies.	71
4.2	Example of α fit for PSR B2217+47 at epoch MJD 57372.	72
4.3	The top and middle panel consist of scattering index values (α) and scattering time at 69.4 MHz, respectively, over time for PSR B0329+54. The bottom panel consists of δ DM values (blue) and solar elongation angle (red) over time. All four measurements have been made at the same epochs for a span of about three years. For more details see Section 3.	74
4.4	α , τ_{sc} at 69.4 MHz, δ DM, and solar elongation angle for every epoch for PSR B0823+26	76
4.5	α , τ_{sc} at 69.4 MHz, δ DM, and solar elongation angle for every epoch for B0919+06	78

4.6	α , τ_{sc} at 62.0 MHz, δDM , and solar elongation angle for every epoch for PSR B1822–09	79
4.7	α , τ_{sc} at 57.2 MHz, δDM , and solar elongation angle for every epoch for B1839+56	80
4.8	α , τ_{sc} at 69.4 MHz, δDM , and solar elongation angle for every epoch for B1842+14	81
4.9	α, τ_{sc} at 69.4 MHz, δDM , and solar elongation angle for every epoch for B2217+47. We include scattering time to show its correlation with δDM (see section 4.7).	83
5.1	Average profiles of PSR B1508+55 at 49.8, 64.5, and 79.2 MHz.	95
5.2	Stacked residual profiles at 49.8 MHz (a) and 64.5 MHz (b) from all the available epochs. The reference profile (black) has been subtracted from the original data. The magenta points denote the location of the main component and the green dots denote the location of the trailing component, changing relative to the magenta points with time. For more details see Section 5.3.1.	97
5.3	Trailing component separation obtained from subtracting the main pulse component at two frequencies: 49.8 and 64.5 MHz.	99
5.4	Timing Residual before (top) and after (bottom) accounting for the change in DM. The y-axis changes scale by a factor of a little over two between the pre-fit and post-fit panels	100
5.5	Above plot shows δDM variation over time. δDM values represent change in DM compared to the average DM value of $19.616 \text{ pc cm}^{-3}$ for PSR B1508+55. The error bars on δDM values are smaller than the size of the points.	101

5.6 A simplified cartoon showing this scattering of pulsar signal from the ISM ionized gas cloud. The main component travels along D and the post-cursor along X1-X2. The angle δ is the deflection angle, which is equal to the refractive angle. This figure has been adapted from Michilli et al. (2018). 105

List of Tables

2.1	Observations	41
2.2	Stationary Gaussian Model Components	42
2.3	Variable Gaussian Model Components	43
2.4	Fitting Parameters	44
2.5	C2 Jet parameters	45
3.1	Observational parameters comparison	56
3.2	MRK 231 Gaussian Components	58
4.1	Selected Pulsars Observed with LWA1	67
4.2	IPM Frequency Parameters	70
4.3	Scattering Results	85

List of Acronyms

ISM	Interstellar Medium
IPTA	International Pulsar Timing Array
NANOGrav	North American Nanohertz Observatory for Gravitational Waves
EPTA	European Pulsar Timing Array
PPTA	Parkes Pulsar Timing Array
PTA	Pulsar Timing Array
GWs	Gravitational Waves
SMBH	Super Massive Black-hole
SMBBH	Super Massive Binary Black-hole
RMS	Root Mean Square
TOA	Time of Arrival
mHz	milliHertz
Jy	Jansky
SNR	Signal to Noise Ratio
VLBA	Very Long Baseline Array
VIPS	VLBA Imaging and Polarimetry Survey

Chapter 1

Introduction

“When you look at the stars and the galaxy, you feel that you are not just from any particular piece of land, but from the solar system.” - Kalpana Chawla

The title of this dissertation may sound a bit dispersed but that is actually the theme of this dissertation. This work is a combination of a study of pulsars and a search for SuperMassive Binary Black Holes (SMBBHs). Pulsars are rotating neutron stars which are abundant across our galaxy. On the other hand, SMBBHs are really massive black holes ($10^6 - 10^9 M_{\odot}$) and have thus far rarely been detected . Both of these sources are exotic and very different from one another in their physical properties, yet they are tied with a common thread - Gravitational Waves (GWs). In this chapter, we explore the basic aspects of all these different topics which lays the foundation of this dissertation. Section 1 gives an overview of pulsars and Section 2 details the interaction of the pulsar signal with their surroundings. In Section 3, we discuss GW astronomy, its sources and the role of pulsars in their detection. In Section 4, we present the outline of this thesis.

1.1 Pulsars

Neutron stars were first predicted by Walter Baade and Fritz Zwicky in 1934 (Baade and Zwicky, 1934). However, they were first discovered in 1967 by Jocelyn Bell, when she was a graduate student at Cambridge University. She found a periodic signal originating outside our solar system (Hewish et al., 1968). This radio source was soon theorized to be a rotating neutron star with a magnetic field (Gold, 1968). Since then many new discoveries have been made in the past four decades while understanding pulsar astrophysics. It has also enabled testing of the validity of Einstein’s general theory of relativity (Will, 2014). Due to their exotic nature, we continue to use them as laboratories to understand extreme conditions which cannot be created in the lab.

In simple terms, pulsars are rotating neutron stars. Their formation takes place when the outer layer of a massive star ($8 - 20M_{\odot}$) (Stairs, 2004) explodes and its core collapses during a supernova explosion. The core counteracts the gravitational collapse with the degeneracy pressure provided by the tightly packed neutrons. Their expected mass is about $1.4 M_{\odot}$ (Chandrasekhar, 1931) and the observed mass obtained from binary systems ranges between $1.2 - 2.1M_{\odot}$ (Kiziltan et al., 2013, Özel and Freire, 2016). Neutron stars are very compact and have a radius of about 10 km with a high density ranging between $10^{12} - 10^{14} \text{ gm cm}^{-3}$ (Lyne, 2006). The exact equation of state for a neutron star is still under investigation. Neutron stars have beamed emission along their magnetic axis. If there is a misalignment between the magnetic axis and the rotation axis, the signal arrives in the form of pulses. A rotating neutron star, with misaligned magnetic field axis, is known as a pulsar! The word pulsar is a contraction of the words “pulsating star”.

1.1.1 Pulsar Energetics

Pulsars emit across the entire electromagnetic spectrum ranging from radio waves to gamma-rays. However, the mechanism for radio emission differs from those at higher frequencies. In the canonical model (Fig. 1.1), pulsars have a bipolar magnetic

field, with closed and open field lines. The magnetosphere around the pulsar is filled with plasma and it co-rotates with the pulsar. However, this co-rotation breaks down before the light-cylinder where the speed of charged particles approaches the speed of light. The charged particles move along the open magnetic field lines and emit via the mechanism of synchrotron emission. This contributes to radio emission which is also highly polarized. However, the exact emission mechanism is still not understood.

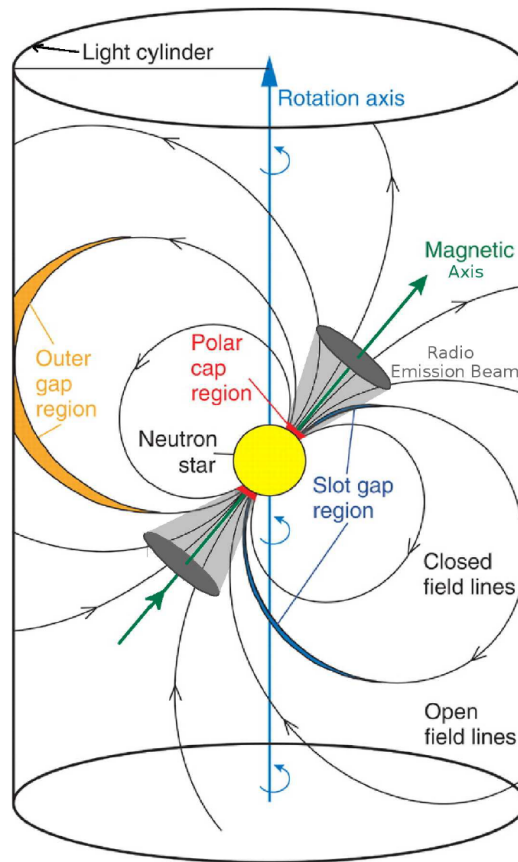


Figure 1.1: A toy model for pulsar emission and its magnetosphere: The radio emission originates from the magnetic poles in two narrow beams. It is caused by open field lines originating from the polar caps. The magnetosphere co-rotates with the pulsar within the light cylinder. Adapted from Lyne (2006).

The rotating magnetic dipole loses rotational energy due to magnetic dipole radiation. This causes a decay in the period of the pulsar over a sufficiently long timescale, and results in orbital period lengthening. The rate of increase in period, P

is $\dot{P} = dP/dt$, which is related to the loss of rotational kinetic energy (\dot{E}) given by

$$\dot{E} = 4\pi^2 I \dot{P} P^{-3}, \quad (1.1)$$

where I is the moment of inertia. The above equation is equal to the the loss of radiation power (Lorimer et al., 2005). Using these two relations, the evolution of the rotational period can be given by

$$\dot{P} = CP^{2-n}, \quad (1.2)$$

where C is a constant and n is the braking index. For a pure magnetic dipole model, $n = 3$. This braking index can be used to obtain the *characteristic age* (τ_c) of a pulsar using the following relation

$$\tau_c = \frac{P}{(n-1)\dot{P}}. \quad (1.3)$$

Typical *characteristic ages* of pulsars are from 100 kyr to 10 Gyr. Note that this does not represent the exact age of a pulsar. For example, the *characteristic age* of the Crab pulsar is 1240 years which is comparable to the actual age of this pulsar of about 950 years. This discrepancy is likely due to deviations from $n = 3$ which have been observed in numerous cases (e.g. Archibald et al., 2015).

Assuming the same spin-down model, the magnetic strength of a pulsar at the surface can be obtained by

$$B = 3.2 \times 10^{19} (P\dot{P})^{0.5} \text{Gauss}. \quad (1.4)$$

Note that this is a lower limit on the magnetic field as it has been obtained for an orthogonal rotator. The observed strength of the magnetic strength is between $10^{11} - 10^{13}$ Gauss for normal pulsars and between $10^8 - 10^{10}$ Gauss for millisecond pulsars (MSPs) (Lyne, 2006).

1.1.2 Pulsar statistics

Pulsars are highly periodic in nature and their period (P) can be measured with high precision. The currently available range of periods for pulsars is from 1.27 ms (Hessels

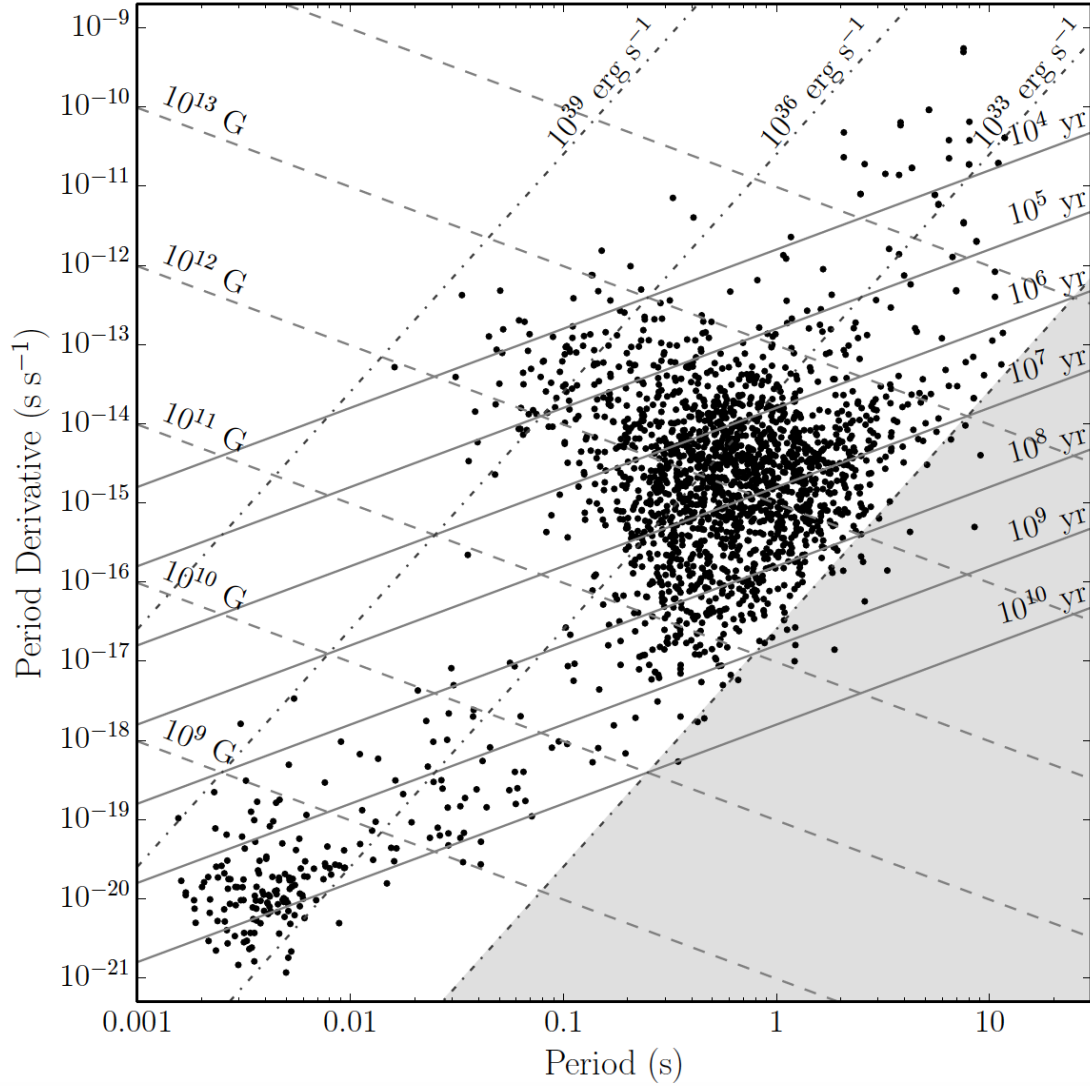


Figure 1.2: $P - \dot{P}$ diagram. This figure shows the entire population of pulsars. It is evident from the plot that there are two types of pulsar population: the central region shows normal pulsars and the bottom left shows MSPs. Using their spin period (P) and spin period derivative (\dot{P}), their magnetic field strength on the surface, their age, and their spin-down energy can be obtained. The shaded region denotes the pulsar graveyard and its boundary is the death line. Credit: Michael Lam

et al., 2006) to 23.5 seconds for the longest period (Tan et al., 2018). So far more than 2500 isolated pulsars and about 200 binary pulsars have been discovered. Based on the period of a pulsar, they can be classified into two categories: milli-second pulsars (MSPs) and normal-pulsars. MSPs, as the name suggests, have a period of

the order of a few milliseconds. Fig. 1.2 shows a distribution of pulsars based on their P and \dot{P} values. The central region consists of normal pulsars (~ 1 s) which are powered by rotation. As time progresses, normal pulsars move to the lower right side which represents the pulsar death-region. In this region, their emission mechanism shuts off and they are no longer detectable. The population on the lower left side represents the MSPs. Unlike normal-pulsars, these pulsars are believed to be recycled pulsars where an old neutron star accretes from its binary companion. This accretion causes an increase in the mass of the neutron star and increases its rotational speed. This is why MSPs are also known as “recycled” pulsars.

As pulsars spin down due to the loss of rotational energy, their period of rotation elongates. Apparently, MSPs have a lower spin-down rate as their magnetic field is weaker compared to normal pulsars which make them stable rotators. This is why they are used in the pulsar timing arrays (PTAs) (Section 3.2). To date about 260 MSPs have been discovered¹.

1.1.3 Pulsar Profile Properties

A pulsar emits a train of periodic pulses. The observed pulse profile shape depends on how the line of sight crosses the polar cap region as the pulsar rotates. The simplest model of the radio beam is a cone-shaped beam framed by the arrangement of dipole magnetic field lines (Radhakrishnan and Cooke, 1969). Although each pulse differs from another, an average over thousands of pulses at the same frequency forms a steady integrated profile. Each pulsar carries a unique pulse profile, which can be used as a fingerprint.

Pulse profiles of majority of the pulsars vary with frequency. The first frequency dependent effect is that the total width and separation between the profile components increases as we go towards lower frequencies. The variation is interpreted using the radius-to-frequency mapping (Cordes, 1978). According to this model, emission at higher frequencies originates closer to the surface of the pulsar leading to a narrower

¹<http://www.atnf.csiro.au/people/pulsar/psrcat/>

profile as compared to those at lower frequencies. This effect is seen more strongly in case of normal pulsars as compared to the MSPs.

Integrated pulses are complex in nature and consist of a number of distinct components. The average number of components in a normal pulse profile is about 3 and for an MSP is 5 (Kramer et al., 1998). Detection of additional components may require observations with higher sensitivity. Another frequency dependent effect is the variation in the number of components in the pulse profile. Based on the number of components, the structure of a magnetosphere can be discerned.

Pulsars are generally weak radio sources. The mean flux density of pulsars varies with the observing frequency. This dependence can be given by a simple power law : $S(\nu) \propto \nu^\alpha$. The typical range of spectral indices is between -4 and 0 with the average spectral index value of -1.4 ± 1.0 (Bates et al., 2013). Interestingly, large deviations from this simple power law have been observed as many pulsars show a turnover in spectra below 100 MHz (Bilous et al., 2016). In this thesis, we have used frequencies below 100 MHz (Chapter 4 & 5), where the turnover can be seen.

In addition to the frequency dependence, a few time-dependent variations in the integrated pulse profile have also been observed. These are caused either due to changes in the pulsar magnetosphere or due to their interaction with their surroundings. We further investigate these temporal variations in more detail in Chapter 5, where we explore the underlying cause of the variation in the pulse profile of PSR B1508+55.

1.2 Interstellar medium

The space between the stars is filled with gas, dust, and ionized plasma. When a pulsar signal traverses through the ionized interstellar medium (ISM), it deviates from its original path. The primary observable effects are dispersion, Faraday Rotation, scattering, and scintillation. Studying these phenomena helps us probe the characteristics of the ISM. For the purpose of this thesis, we will only focus on the ionized plasma since it interacts with radio waves and plays a key role in

causing phase deviations. Below we discuss all the effects mentioned earlier, with the exception of Faraday Rotation, which is beyond the scope of this thesis.

1.2.1 Dispersion

Dispersion is the largest contributing frequency dependent effect. For example, when you shine a light on a prism, it splits into its constituting colors as different frequencies travelling at different speeds. Similarly, when light traverses the ISM, it gets dispersed. This causes a frequency dependent delay in the arrival time of pulses such that the higher frequencies arrive earlier than lower frequencies. Fig. 1.3 shows a frequency dependent delay caused by dispersion in the pulse profile for PSR B0950+08. The difference between the pulse arrival time at two frequencies can be given by,

$$\delta t = t_2 - t_1 = K \cdot DM \left(\frac{1}{f_1^2} - \frac{1}{f_2^2} \right), \quad (1.5)$$

where t_2 and t_1 are the arrival times at two different frequencies and K is the dispersion constant equal to $e^2/2\pi m_e c$. DM is the dispersion measure in units of pc cm^{-3} . It is the integrated column density of free electrons along the line of sight to a pulsar, also defined as

$$DM = \int_0^D n_e dl, \quad (1.6)$$

where n_e is the electron density along the line of sight and D is the distance to the pulsar. Before averaging pulse profiles in frequency, we need to correct for the dispersion effect. Otherwise, the average profile gets smeared out. We correct for this frequency dependent delay using incoherent and coherent dedispersion methods. Interested readers may refer to [Stairs \(2002\)](#) for more detail about dedispersion. Correction for the dispersion delay helps in measuring the DM value, which can be used to obtain the mean electron density for pulsars where distance measurements are available. It can also be used to measure the distance to a pulsar assuming the electron density distribution from a model such as the NE2001 model ([Cordes and](#)

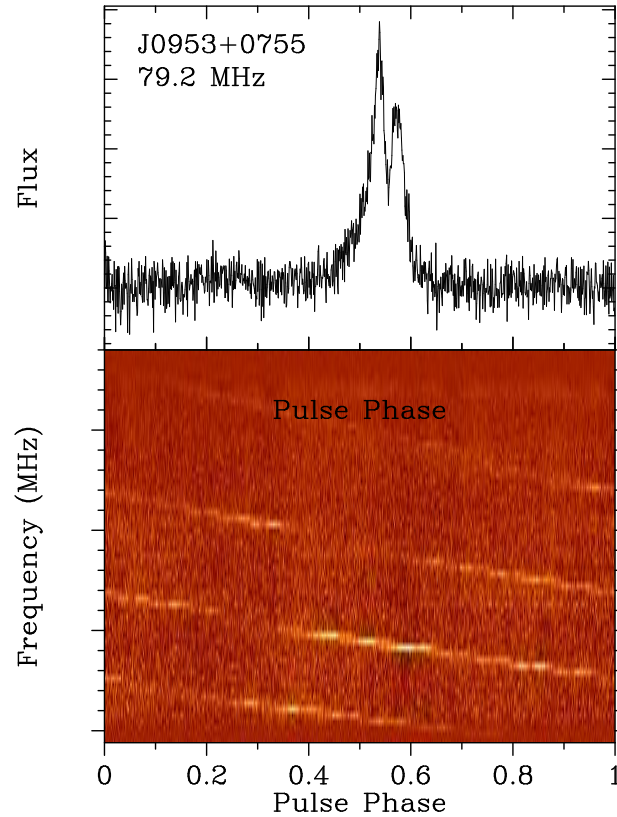


Figure 1.3: The upper panel contains the average profile of PSR B0950+08. The lower panel shows the delay in pulse with decreasing frequency caused due to the dispersion effect. The phase delay wraps around four times indicating a strong effect at the observed frequency of 79.2 MHz. Credit: K. Bansal

Lazio, 2002). Dispersion is also useful in distinguishing a terrestrial signal from those of astrophysical origin.

The DM value of a pulsar depends on its location in the Galaxy. If it is located near the Galactic center, the expected DM is quite high, whereas pulsars outside the Galactic plane have DM values below $\sim 250 \text{ pc cm}^{-3}$. For extragalactic sources, it is even higher as it has a contribution from both the ISM and the intergalactic medium.

In Chapter 4 and 5, we will discuss how we obtained the DM values using *TEMPO* (van Straten et al., 2012) in more detail. We also study the time-dependent variation

in the DM for all the sources in our sample. Variations in DM over time have been observed for multiple sources (e.g. the Crab Pulsar). It is due to a change in the line of sight caused by the relative motion of a pulsar with respect to the Earth through the turbulent ISM. It can also be due to solar winds which also contributes to changes in DM . In this thesis, we have studied eight pulsars at frequencies below 100 MHz. You can see from Equation 1.5 $DM \propto f^{-2}$, indicating that at low frequencies this effect is stronger. This implies that DM measurements below 100 MHz will be of high precision, enabling us to measure small changes in DM . Such DM variations can provide further insight into the turbulence of the ISM.

1.2.2 Scattering

The ISM is highly turbulent and inhomogeneous. It can be described using the thin-screen model (Williamson, 1972) which approximates that the random irregularities in the ISM between the source and the observer are concentrated into a thin screen. It also assumes that the size of the screen is infinite, implying that there is no loss of flux density due to scattering. Fig. 5.6 shows a schematic of the thin-screen model. Consider a pulsar at a distance D from the observer with a scattering screen at distance D_s from the pulsar. When the pulsar signal moves through this screen, it undergoes random phase scattering, modifying its original path and delaying the pulse signal. The time delay (t_{sc}) compared to an unscattered light ray is given by

$$t_{sc} = D_s \left(1 - \frac{D_s}{D}\right) a^2 / 2c, \quad (1.7)$$

where a is the scattering angle. This delay results in an asymmetric exponential temporal broadening in the pulse profile. Pulse broadening has a strong frequency dependence with pulse profiles at lower frequencies having broader tails. The magnitude of the scattering depends on the scale of inhomogeneities. These irregularities in the ISM cause a fluctuation in the refractive index which in turn affects the phase of a wavefront. Phase delay due to one irregularity of size d , with plasma fluctuation

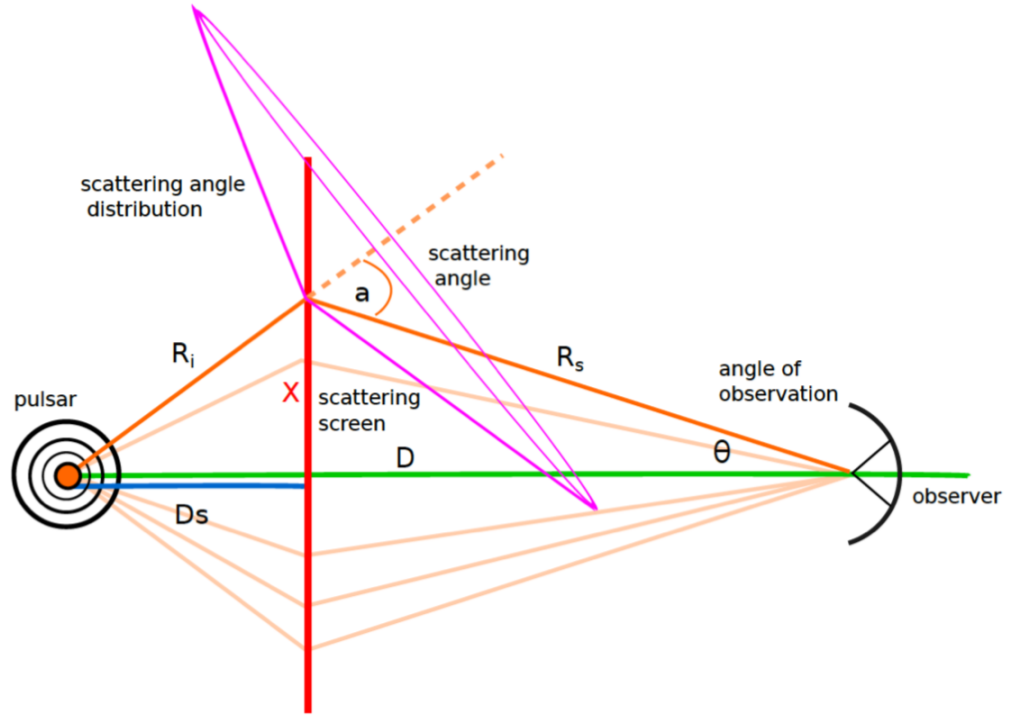


Figure 1.4: Schematic of the interaction of pulse signal with the ISM: A pulsar emits spatially coherent EM radiation which interacts with the scattering screen at a distance of D_s from the pulsar. The scattering angle is a , which denotes the phase deviation in the straight line path of a ray caused due to scattering. The angle of observation (θ) is the angular width of the source. As the distance to the pulsar is large ($D \sim \text{kpc}$), these angles (θ, a) are small. Credit: M. Meyer

electron density of δn_e , is

$$\phi = r_e \delta n_e d c / \nu, \quad (1.8)$$

where r_e is the classical electron radius. The rms phase delay due to various inhomogeneities along the entire line of sight is

$$\phi_{rms} = (D/d)^{1/2} \langle \Delta\phi^2 \rangle^{1/2} \propto r_e (Dd)^{1/2} \frac{\langle \Delta n_e^2 \rangle}{\nu}, \quad (1.9)$$

where D is the distance to the source. This will lead to the rms scattering angle (a) of

$$a_{rms} = \frac{\phi_{rms}/k}{d} \propto r_e \left(\frac{D}{d}\right)^{1/2} \frac{\langle \Delta n_e^2 \rangle^{1/2}}{\nu^2}. \quad (1.10)$$

The above equations are based on derivations in Lang (1971) and references therein. By substituting the value of a_{rms} in Equation 1.7, we obtain $t_{sc} \propto \nu^{-\alpha}$, showing a strong frequency dependence. α is the scattering index and its value depends on the distribution of inhomogeneity in the ISM. For a Gaussian distribution in electron density $\tau_{sc} \propto \nu^{-4}$. However, for Kolmogorov distribution this proportionality changes to $\nu^{-4.4}$ (Rickett, 1977, Romani et al., 1986).

Electron density variations for an isotropic and homogeneous medium can be described as power law wavenumber spectrum,

$$P_{\delta n_e} = \frac{C_{n_e}^2(z)}{(q^2 + k_o^2)^{\beta/2}} \exp\left(-\frac{q^2}{4k_i^2}\right), \quad (1.11)$$

where $C_{n_e}^2(z)$ is the scattering strength, q is the three dimensional wavenumber, and $1/k_o$ and $1/k_i$ are outer and inner scale of turbulence. These scales represent the boundary beyond which there is no turbulence. When the wavenumber $k_o \ll q \ll k_i$ the above equation gets simplified to $P_{\delta n_e} = C_{n_e}^2(z)q^{-\beta}$. An upper limit on the inner scale of turbulence of 10^8 m was obtained by Armstrong et al. (1994). The isotropic model remains valid as long as the diffractive scale of scattering is much smaller than inner scale limit of turbulence.

An example of pulsar scattering can be seen in Fig. 1.5. From the above formulation, and this figure, we can see that temporal broadening depends on the frequency and is significant for low-frequency observations. Hence, studying the temporal broadening at frequencies below 100 MHz (Chapter 4) will be useful to understand the underlying processes as long as the SNR is adequate. Scattering time also depends on the distance to the pulsar. In order to have a smaller effect on pulse arrival time, nearby MSPs ($D \leq 1$ kpc) are preferred. We will discuss this in more detail in Section 3.2.

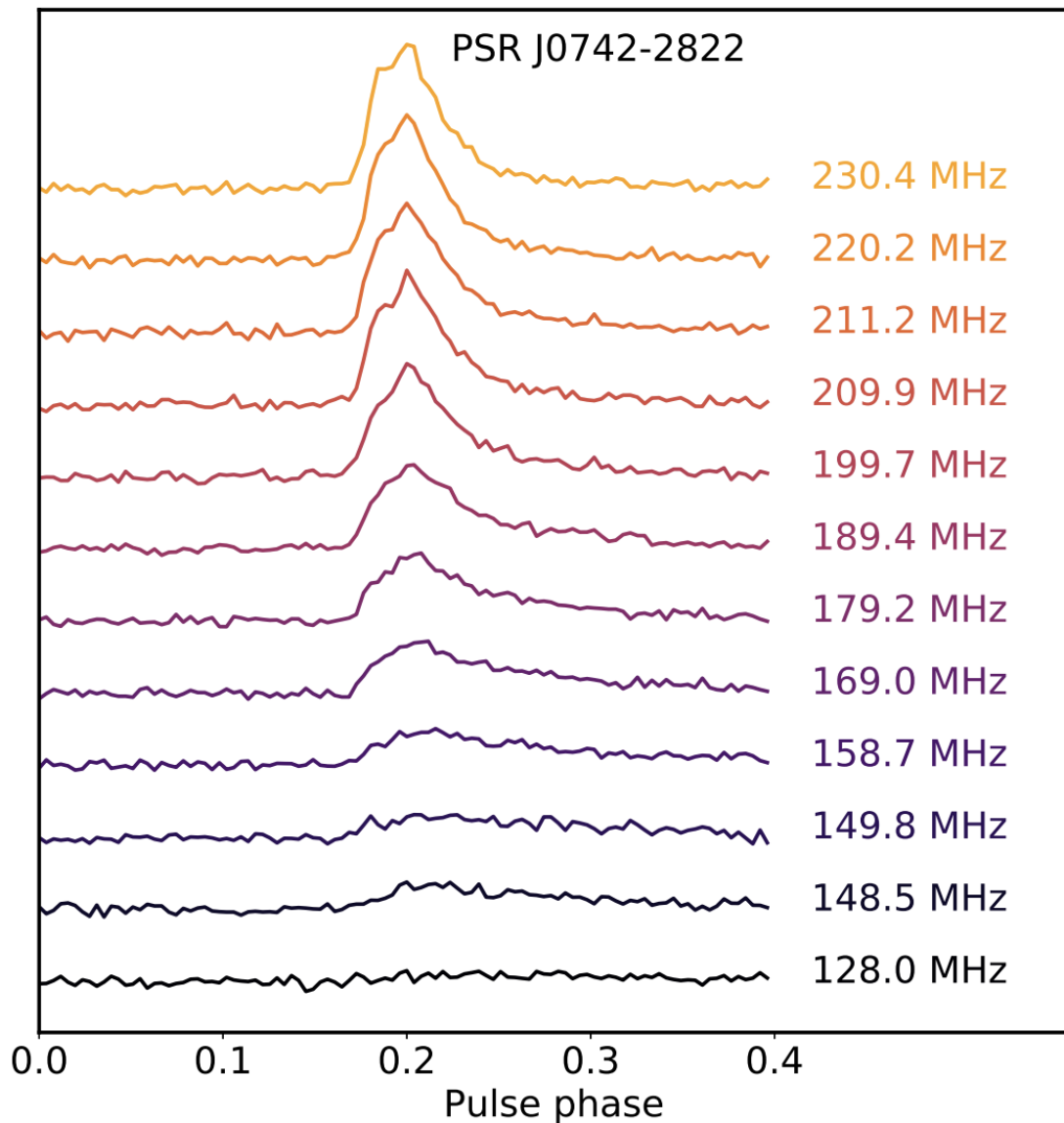


Figure 1.5: This plot shows variation in pulse profile broadening with frequency for PSR J0742-2822. As we go towards the lower frequencies, the amount of scattering increases which results into a broadened profile. Here, due to high scattering, the profile becomes undetectable below 148.5 MHz. Adapted from Kirsten et al. (2019)

1.2.3 Scintillation

Another effect of multi-path propagation is scintillation. This is a variation in the flux density of a source with time and frequency. Depending on the distance between

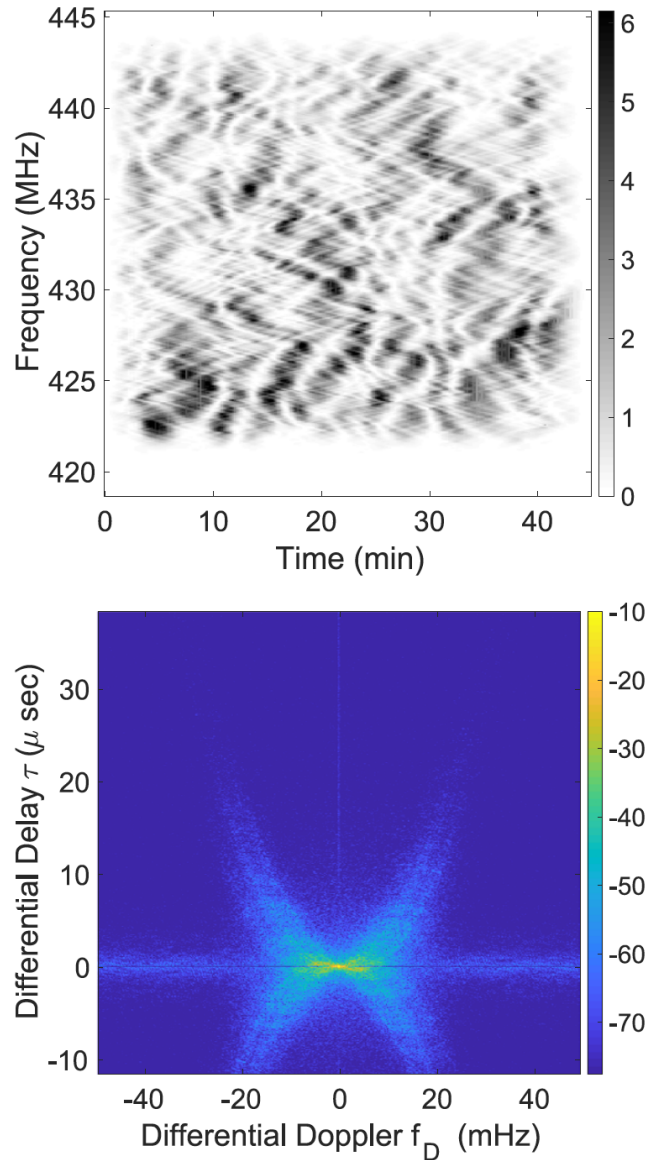


Figure 1.6: Interstellar Scintillation: The top panel is a dynamic spectrum for PSR B1133+16 and the bottom panel consist of their autocorrelation functions. It was observed with the Arecibo Observatory at 432 MHz. These plots have been adapted from [Stinebring et al. \(2019\)](#).

the source and observer, there are two kinds of scintillation: weak and strong. These regimes are determined on the basis of coherence radius defined as $s_0 = 1/(k\theta_0)$, where $k = 2\pi/\lambda$ and θ_0 is the size of a circular image on the thin screen. Within the coherence length, the phase difference is less than 1 radian. When the Fresnel scale

($r_F = (D/k)^{1/2}$) is in the far field limit, $r_F \gg s_0$, weak scattering takes place, and when it is in the near field zone, $r_F \ll s_0$, strong scattering takes place. In this thesis, all the observations fall into the strong scattering regime as these have been caused due to large phase perturbations.

Strong scintillation gets further divided into diffractive and refractive scintillation based on the time scale of variation in intensity. In the case of diffractive scintillation, the intensity changes over a few minutes to days whereas in case of refractive scintillation there are weaker variations in intensity over weeks to months. In all the scintillation types, depending on the phases of the wavefronts, constructive and destructive interference takes place. However, in order to have constructive interference, the points need to be within the coherence radius, implying

$$\delta\Phi = 2\pi\delta\nu t_{sc} = C_1, \quad (1.12)$$

where $\delta\nu$ is the coherence bandwidth (Cordes, 1986, Lyne and Rickett, 1968) and C_1 is a constant which is 1.16 for a Kolmogorov distribution (Cordes et al., 1985). This interference leads to the formation of bright patches in the dynamic spectra, also known as the ‘scintle’ (Fig. 1.6). A dynamic spectra is a 2-D observational plot which shows intensity as a function of frequency and time. These scintles form due to the relative motion of the pulsar, observer, and the thin-screen. The 2-d Fourier transform of the dynamic spectra is used to obtain the secondary spectrum. Stinebring et al. (2001) found that the scintles in the dynamic spectra result in scintillation arcs in the secondary spectra (bottom panel). These parabolic arcs are used to find the distance to the screen. Thus a secondary spectra plays an important role in providing insight into the sizes and distribution of scattering surfaces in the Galaxy. Scintillation measurements are useful for testing assumptions of the thin-screen model (Section 1.2.4). We utilize them to interpret the results from our scattering study at low frequencies (Chapter 4).

1.2.4 Deviation from the thin-screen model

Both scattering and scintillation have been studied for numerous sources. A large number of them have been found to show deviations from the isotropic model of ISM. For example, [Brisken et al. \(2009\)](#) studied scintillation in PSR B0834+06 at 322.5 MHz, where along with the parabolic arcs they also observe an elongated image of the pulsar. They suggest that these observations are the result of scattering due to highly anisotropic filaments in ISM. It is expected that scattering may have a preferred direction due to the presence of the magnetic field in the galaxy. This will lead to the extended images of point sources behind the scattering screen along one axis. However, the exact scale of anisotropy is unknown. In a few cases, multiple arcs and arclets have been observed ([Stinebring, 2006](#)). These imply the existence of multiple screens which contradicts the thin screen model where we consider only one screen.

The estimated scattering spectral index values for various pulsars are smaller than the predicted values ([Geyer et al., 2017](#), [Lewandowski et al., 2013, 2015](#), [Löhmer et al., 2001, 2004](#)), but also some values are larger than expected ([Rickett, 1990](#), [Tuntsov et al., 2013](#)). These deviations suggest anomalous scattering mechanisms and their corresponding geometries.

We discuss temporal broadening in more detail in Chapter 4, where we explore this phenomenon for seven pulsars. We also describe the methods we employ to obtain the spectral index as both scattering and pulse evolution have a frequency dependence, complicating the deconvolution. With the advantage of having simultaneous multi-frequency observations, we measure the frequency scaling index of scattering and its evolution over time for these pulsars. This study enables us to compare our results with theoretical predictions and probe the distribution of inhomogeneities in the ISM.

1.3 Low frequency Gravitational Waves

GWs were predicted by Einstein's general theory of relativity about 100 years ago. These are quadrupolar fluctuations in the curvature of space-time that are produced due to an accelerating mass. The first direct detection of GWs was made recently when [Abbott et al. \(2016\)](#) detected GWs from a binary black hole merger using the laser interferometry gravitational observatory (LIGO). This discovery has now opened a new window which astronomers hope to use to explore parts of the cosmos undetectable with our traditional methods - Electromagnetic (EM) waves. This is a remarkable achievement for which Barry C. Barish (Caltech), Kip S. Thorne (Caltech), and Rainer Weiss (MIT) were awarded the Nobel Prize in Physics in 2017.

There are several sources for GWs such as black hole mergers, black hole-neutron star mergers, neutron star mergers, and supermassive-black hole (SMBH) mergers. The frequency of the GWs depends on the interacting system. Just like EM waves that have a large range of frequencies, GWs also have a range of frequencies (Fig. 1.7). GWs from the stellar mass mergers have frequencies from ten to thousands of Hz. Both LIGO and VIRGO are sensitive to these frequencies and will continue detecting GWs from similar systems in the future. However, the merger of SMBHs in the center of merging galaxies results in GWs in the frequency range of nano-Hertz. These waves can be detected using an instrument known as the PTA.

Besides these two types of experiments, two space-based interferometers are also being developed: the Laser Interferometer Space Antenna (LISA) and a joint project between NASA and the European Space Agency. These instruments will be sensitive to GW frequencies on the scale of milli-Hertz (mHz). These instruments are designed primarily to observe mHz GWs from massive black hole binaries and extreme mass ratio inspirals (massive black holes with small compact object companions).

PTA observations will be complementary to both ground and space-based GW experiments. Recently LIGO was upgraded to improve their sensitivity. This process has helped them understand their system better. Similarly, a deeper understanding

of the PTA noise sources is required as the signal propagates through the ISM to the telescope to confidently detect the GWs.

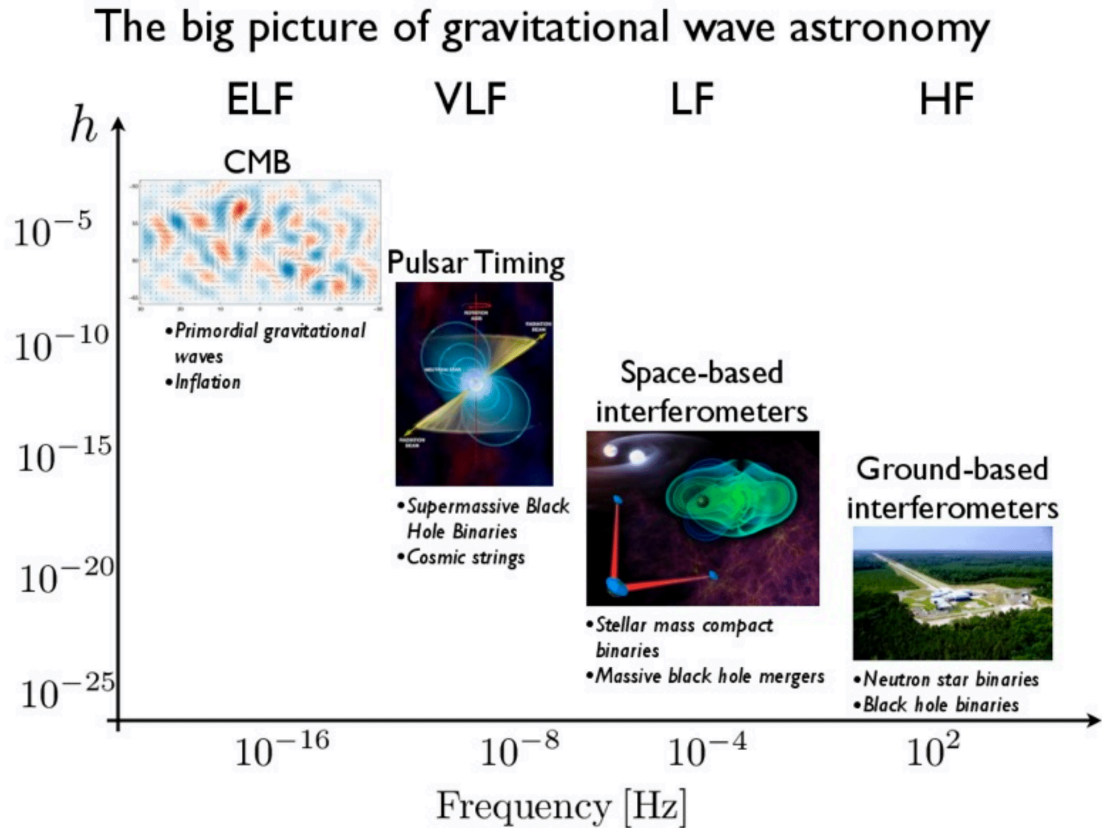


Figure 1.7: This figure shows the entire GW spectrum. The vertical axis indicates the amplitude of h of each expected GW which are observed by a different observatory depending on their frequency. The ground-based observatory is LIGO which made its first discovery in 2015. There are space-based interferometers which are supposed to operate in the 2030s. Detection of GW from PTAs is still in progress and hope to have detection in the early 2020s. Credit: North American Nanohertz Observatory for Gravitational Waves (NANOGrav)

1.3.1 Supermassive Binary Black Holes

There are primarily four types of black holes: Primordial black holes, Stellar mass black holes, Intermediate mass black holes, and Supermassive black holes (SMBH). Primordial black holes are the smallest of all the types and due to their small mass

they should radiate away as predicted due to Hawking radiation. They are expected to form when the universe was very young. Stellar mass black holes have masses ranging from about five to hundreds of times the mass of the Sun. These types of black holes form when a high mass star undergoes a supernova explosion such that it sheds away its outer layers and the core collapses. Although there were many known stellar black hole candidates, their existence was confirmed only recently when the LIGO first detected the GW signature. Intermediate black holes have mass ranging from few thousands to a few 100 thousand times the mass of the Sun. There is suggestive evidence for these black holes, however, they have not yet been confirmed. The last category consist of SMBHs. These black holes have masses ranging from $10^6 - 10^9 M_{\odot}$. These black holes reside at the heart of most of the large galaxies in the universe, including our own Galaxy, the Milky Way. Strong evidence of the existence of these black holes was found recently when the Event Horizon Telescope (EHT; Akiyama et al., 2019) imaged the shadow of a SMBH at the center of a nearby galaxy (M87), making it the first black hole image ever.

When both the merging galaxies have an SMBH at their respective centers, their merger is expected to form a supermassive binary black hole (SMBBH) system. SMBBHs are important for understanding the formation of galaxies, galactic dynamics, and of course, the future nano-hertz GWs. So far only a handful of SMBBHs are known despite the large number of merging galaxies. This has been one of the main driving questions behind the multitude of searches for these system. Hence, it is important that we understand their EM emission before we get evidence of their GW counterpart.

Galaxy mergers are of two types: major and minor. In major mergers, the interacting galaxies have comparable masses whereas in minor mergers one galaxy is significantly larger than the other. In case of a major merger, the dynamical friction drags both of the SMBHs to the center of the newly formed galaxy. The orbit of the SMBHs decays as they interact with the stars, gas, and dust in their surrounding and forms a gravitationally bound binary system. During the 3-body scattering with stars, a loss cone forms (Sesana et al., 2007) due to which further orbital decay stalls. This

is also known as the last-parsec problem. According to simulations, the further decay of the orbit is possible if the binary system either resides in a gas-rich environment where the gas may funnel down the system (Cuadra et al., 2009, Escala et al., 2004) or there is a triaxial symmetry (Khan et al., 2013, 2016). Once the binary system manages to evolve to mpc separation, GWs drive the further decay of the orbit; the black holes coalesce and then eventually merge (Begelman et al., 1980, Milosavljević and Merritt, 2003). Despite the last-parsec phase being theoretically the longest phase in the evolution of a galaxy merger, we have been unable to find sub-parsec SMBBH sources.

There are numerous observational explanations that account for the lack of their detections. First of all, the physical separation of the gravitationally bound SMBBHs is too small to image them directly. The second limitation arises if only one of the two black holes accretes sufficiently to be detectable. The rate of accretion depends on the amount of surrounding gas. Hence, a search for more SMBBHs will enable us to constrain the merger rates at various phases of a merger as we have no reliable estimate of how much time is spent in each stage. Moreover, it will provide insights into how gas and stellar population play a role in governing these stages.

Clearly, galaxy mergers play a key role in galaxy evolution. GW detection of SMBBHs combined with their EM counterparts (multi-messenger) will enable us to improve our understanding of how SMBHs co-evolve with their host galaxies as well as the dynamical interactions between binaries and their galactic environments. However, their co-detection in EM and GW will depend on the merger rate and the distribution of Active Galactic Nuclei (AGN) in the local universe as well as on the timescale of various stages.

1.3.2 Pulsar Timing

As mentioned earlier, pulsars emit regular pulses which makes them high precision astronomical clocks. A measurement of the arrival time of pulses is known as **pulsar timing**, which accounts for every rotation of a pulsar. Any deviation in the times of

arrivals (TOAs) of the pulses from the expected pulse profile model can be exploited to study various phenomena. These include mass determinations of neutron stars and testing of the general theory relativity and other theories of gravity (Will, 2014). It also constrains changes in the fundamental constants (Lazaridis et al., 2009, Zhu et al., 2015) and most importantly, in the future, it will be used as a detector for low-frequency (nanohertz) GWs (e.g., Arzoumanian et al., 2016).

The first step in obtaining the TOAs is to transform them into an inertial reference frame, typically the Solar system barycenter. The average pulse profile is used as a model for obtaining TOAs for subsequent observations. The TOAs need to be corrected for various delays such as DM, Romer delay, Einstein delay, and Shapiro delay caused due to the orbital motion of the Earth and effect of the solar bodies.

The uncertainty of a TOA measurement depends on the pulse width (W) and the signal to noise ratio (S/N) of the profile. It scales as

$$\sigma_{TOA} \propto \frac{W}{S/N} \propto 1/\sqrt{N_p}. \quad (1.13)$$

Low TOA uncertainty can be achieved by increasing the number of pulses and reducing the width of the profile. MSPs are ideal for this purpose as their rapid spin periods result in pulse widths that are much narrower than normal pulsars. A common σ_{TOA} for a MSP is $\sim 1\mu s$.

The timing model consists of rotation (P, \dot{P}), proper motion, parallax, and binary orbital motion of a pulsar. It also accounts for the effect of the ISM by including the DM. Interestingly, modeling all of these parameters for an individual pulsar is a large active area of research, which pulsar timing arrays are built upon. The deviations from this model are called timing residuals (R), given by

$$R = t_{obs} - t_{model}. \quad (1.14)$$

In the case of an ideal timing model, the timing residuals would be zero. However, timing residuals are non-zero due to both intrinsic and external processes. Intrinsic processes such as pulsar spin variations are caused by glitches or pulsar precession in a binary system. However, such variations are usually observed in normal pulsars but

rarely in MSPs. External effects are due to the inhomogeneous and turbulent ISM. Due to the relative motion of a pulsar through the ISM, the line of sight changes. This would affect its DM, as well as the pulse profile, which would subsequently affect TOAs. The turbulent ISM can contribute to the pulse shape due to multi-path scattering. We need to account for all these effects before we can observe the influence of GWs.

GWs deform the space as they propagate in different directions. They are quadrupolar which would cause stretching along one direction and shrinking along the perpendicular direction. This will cause a time-dependent variation in the separation between pulsars and the Earth, causing a deviation in the TOAs. The effect of a GW will be present in the time residuals of every pulsar. We expect that for pulsars in the same direction these deviations would correlate. This correlation depends on the angular separation between pulsars, also known as the famous Hellings-Downs curve (Hellings and Downs, 1983).

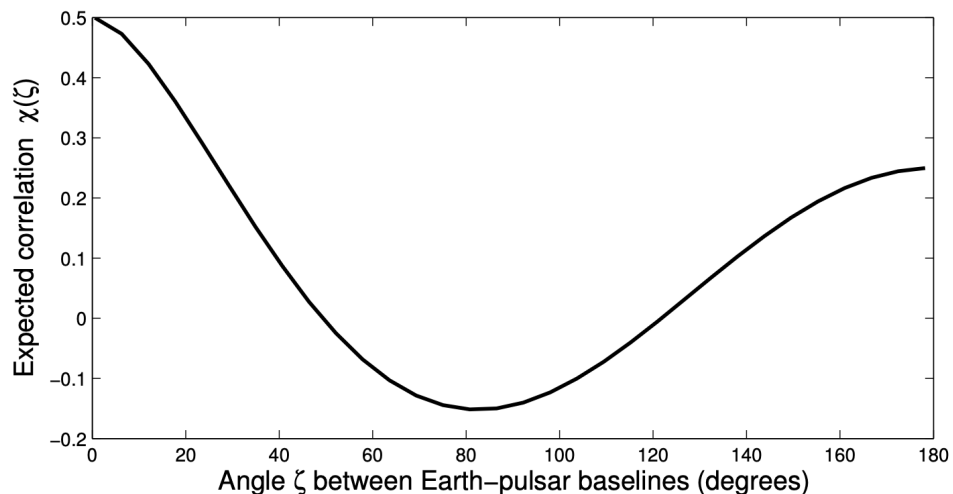


Figure 1.8: Hellings and Downs curve for isotropic and stochastic GW background as a function of the angle between pulsars and the Earth (Jenet and Romano, 2015).

Once we account for all the timing noise sources, we are left with timing residuals

which are expected to be the result of only the GWs. The curve in Fig. 1.8 tells what we should see correlation of timing residuals when they are affected due to the GWs. Our goal is to minimize the timing noise and detect the GWs with a high degree of confidence. The amplitude of the timing residuals caused by GWs from a binary system is on the scale of $\sim 100\text{ns}$ (Jenet et al., 2001). As the strength of GWs signal is weak, we need to use a large sample of MSPs to have high sensitivity. A PTA consists of a large array of MSPs which are being monitored concurrently. This increases the observation time to attain our goal of sensitivity.

There are three main PTAs across the entire planet; the European Pulsar Timing Array (EPTA; Kramer and Champion, 2013), NANOGrAV (McLaughlin, 2013), and the Parkes Pulsar Timing Array (PPTA; Manchester et al., 2013). All three collaborations combine their residuals in a global effort to form the International Pulsar Timing Array (IPTA; Manchester, 2013). We hope this work will be helpful in attaining the required limit for the pulsar timing arrays.

1.4 Thesis Outline

We have covered two important aspects of the search of Gravitational Waves from SMBBHs. The first aspect is the search for SMBBHs using the electromagnetic signature. A galaxy merger of two galaxies which host a SMBH at their respective centers should form a SMBBH. Despite there being millions of galaxies in the observable universe, we have only found a handful of SMBBHs. This raises questions about the general picture - what is the actual distribution of supermassive black holes in the universe? Assuming that SMBHs are abundant in nature, how do they grow in size? If they grow by the process of merging - what is the merger rate? Answering these questions will enable us to understand galaxy dynamics on a large scale.

Chapter 2 contains the study of the orbital motion of core components in the SMBBH system 0402+379. This is the most compact binary SMBBH with a separation of about 7 pc. We also estimate the magnetic field near the base of a core using

the “core-shift” effect. As we are interested in the orbital trajectory of SMBBHs, in Chapter 3, we attempt to search for more SMBBHs systems.

In Chapter 4, we study scatter broadening for a sample of seven pulsars for a span of about three years. We also measure the variation in DM for the same epochs. In chapter 5, we study the effect of ISM reflection in the case of PSR B1508+55, where we see a variation in the component separation over time.

Finally, we summarize our results and conclude this thesis in Chapter 6. We also discuss future prospects for the work presented here.

Chapter 2

Constraining the Orbit of SMBBH 0402+379

The contents of this chapter were originally published as part of Bansal et al. 2017, The Astrophysical Journal, 875 (2), 146

Abstract: The radio galaxy 0402+379 is believed to host a supermassive black hole binary (SMBBH). The two compact core sources are separated by a projected distance of 7.3 pc, making it the most compact resolved SMBBH known. We present new multi-frequency VLBI observations of 0402+379 at 5, 8, 15 and 22 GHz, and combine with previous observations spanning 12 years. These show a strong frequency-dependent core shift, which we use to infer magnetic fields near the jet base. After correcting for these shifts we detect significant relative motion of the two cores at $\beta = v/c = 0.0054 \pm 0.0003$ at $PA = -34.6^\circ$. With some assumption about the orbit, we use this measurement to constrain the orbital period $P \approx 3 \times 10^4 y$ and SMBBH mass $M \approx 15 \times 10^9 M_\odot$. While additional observations are needed to confirm this motion and obtain a precise orbit, this is apparently the first black hole system in a visual binary.

2.1 Introduction

It is commonly believed that the later stages of galaxy evolution are governed by mergers. It is very common for galaxies to collide and interact with each other. Considering that most galaxies in the universe harbor supermassive black holes (SMBH) at their centers (Richstone et al., 1998), it can be inferred that massive black hole pairs should be the outcome of such mergers through the hierarchical formation of galaxies (Begelman et al., 1980). This implies that SuperMassive Black Hole Binaries (SMBBH) should be relatively common in the universe. However, despite very extensive searches, very few such systems have been observed (Burke-Spolaor, 2011, Tremblay et al., 2016). The reason for this could be that black holes in a binary system either merge quickly, or that one of them escapes the system (Merritt and Milosavljević, 2005). Hence, understanding these SMBBH systems is important to understand a variety of processes ranging from galaxy evolution to active galactic nuclei (AGN) to black hole growth.

There are two types of galaxy mergers, major and minor. Major mergers result when the interacting galaxies are of similar sizes (mass ratio less than 3:1 (Stewart et al. (2009), and references therein)), whereas in the case of minor mergers one galaxy is significantly larger than the other. A crucial expectation related to galaxy mergers is the emission of gravitational waves. When galaxies merge, due to the dynamical friction between them, the black holes at their corresponding centers sink towards a common center. This leads to the formation of a binary system, such that its orbit decays due to the interaction between the stars, gas, and dust of both galaxies. The two black holes may reach a small enough separation that energy losses from gravitational waves allow the binary to coalesce into a single black hole (Begelman et al., 1980, Milosavljević and Merritt, 2003).

Numerous simulations have been performed to study these SMBH mergers. These simulations deal with various aspects such as black hole mass ratio, self or non-gravitating circum-binary discs, orbital spin, black hole spins, gas or stellar dynamics etc. (Barnes, 2002, Callegari et al., 2009, 2011, Dotti et al., 2007, Escala et al., 2004,

2005, Khan et al., 2011, Merritt and Milosavljević, 2005, Schnittman, 2013, Sesana et al., 2006). In spite of several attempts, attaining the required resolution (last parsec problem ~ 0.01 pc) to study the black hole coalescence has been challenging. The fate of the merger at the parsec scale depends on the amount of surrounding stars and gas, and their interaction with the binary. In the case of a stellar background, due to 3-body scattering, formation of loss cone takes place (Sesana et al., 2007), whereas, in the case of gas rich mergers tidal forces inhibit the gas from falling onto the binary, hence creating a gap (Dotti et al. (2012), and references within). The loss cone causes a decay period longer than the Hubble time (Merritt et al., 2007, Milosavljević and Merritt, 2003), and hardening can be attained for a triaxial stellar remnant with the loss cone being replenished (Merritt and Vasiliev, 2010) and an expected coalescence time of $\sim 10^8$ years (Khan et al., 2011). For gas-rich mergers, the gap doesn't inhibit gas flow (Roedig et al., 2012) and a massive circumbinary disc around the binary promotes the decay leading to a timescale for an equal mass binary $\sim 10^7 M_\odot$ that is less than the age of the Universe (Hayasaki, 2009). For higher mass black holes ($\sim 10^{8-9} M_\odot$) the timescales are greater. In a recent study by Khan et al. (2016), they report that for massive galaxies at high redshifts ($z > 2$) it takes about few million years for black holes to coalesce once they form a binary, whereas, at lower redshifts where nuclear density of host is lower, it may take longer time of order a Gyr.

Gravitational waves from merging black holes are expected as a result of Einstein's General Theory of Relativity (Einstein, 1916, 1918, Janssen et al., 2002, Kox et al., 1997)¹. In September 2015, the Laser Interferometer Gravitational Wave Observatory (LIGO) discovered a gravitational wave (GW) source GW150914, and identified it as a merging binary black hole (BBH) (Abbott et al. 2016a). Although the masses of the two BHs are much smaller ($\sim 30 M_\odot$) in comparison to SMBBHs ($\sim 10^7 - 10^{10} M_\odot$), this discovery provides the first observational evidence for the existence of binary BH systems that inspiral and merge within the age of the universe. It motivates further studies of binary-BH formation astrophysics, and with the upcoming detectors such

¹<http://einsteinpapers.press.princeton.edu/>

as evolving Laser Interferometer Space Antenna (eLISA, Amaro-Seoane et al. (2012)), it will be possible to detect low-frequency GW (around one mHz), emitted from the inspiral of massive black holes (Klein et al., 2016). While mergers of SMBBH's are expected to be common emitters of GW radiation, modulating pulsar timing observations have not yet detected any evidence for a GW signal (Arzoumanian et al., 2016). Pulsar timing observations, unlike LIGO, should be more sensitive to SMBBH mergers (Shannon et al., 2015). 0402+379, with a separation of 7.3 pc between its core components, is one of the most important precursors of GW sources, and is important to understand the reason behind the low incidence of such systems. From the elliptical morphology of the 0402+379 host galaxy (Andrade-Santos et al., 2016), we believe this object to be the result of a major merger.

The radio galaxy 0402+379 was first observed by Xu et al. (1995) as a part of the first Caltech Jodrell Bank Survey (CJ1), although at that time it was not identified as a SMBBH. This source first acquired attention as a Compact Symmetric Object (CSO) candidate (small AGN with jets oriented close to the plane of the sky such that the radio emission from the jets is detected on both sides of the core) in 2003, in the full polarimetry analysis by Pollack et al. (2003). Subsequently, Maness et al. (2004) studied this source at multiple frequencies using the VLBA² (Very Long Baseline Array), and on the basis of its properties, they classified it to be an unusual CSO. Rodriguez et al. (2006) studied this source in more detail and arrived at the conclusion that it is a SMBBH. This source contains two central, compact, flat spectrum and variable components (designated C1 and C2, see Fig. 2.1), a feature which has not been observed in any other compact source. This is one of the only spatially resolved SMBBH candidates (Deane et al., 2014, Gitti et al., 2013). The milliarcsecond scale separation requires high resolving power available only with a telescope such as the VLBA. Although other systems like RBS 797 and J1502+1115 (a triple system) with a separation of about 100 pc have been detected, no system other than 0402+379 has been resolved at parsec scales. We believe that this SMBBH is in the process of merging.

²The National Radio Astronomy Observatory is operated by Associated Universities, Inc., under cooperative agreement with the National Science Foundation.

Rodriguez et al. (2006) imaged this source at multiple frequencies, studying the component motion at 5 GHz, but finding no significant detection of core displacement. In this paper, we incorporate new 2009 and 2015 epochs of 0402+379 VLBA observations at 5, 8, 15 and 22 GHz, while re-analyzing the 2003 and 2005 observations. These data show strong evidence for a frequency dependent core-shift effect (Lobanov, 1997, Sokolovsky et al., 2011). After accounting for this effect, our data set allows a detection of the relative motion of the two cores, making this the first visual SMBBH. We comment on the implications for the orbital period and masses. Throughout this discussion, we assume $H_0 = 71 \text{ kms}^{-1}\text{Mpc}^{-1}$ so that $1 \text{ mas} = 1.06 \text{ pc}$.

2.2 Observations and Data Reduction

2.2.1 VLBA Observations

Observations were conducted on December 28, 2009 and June 20, 2015 with the VLBA at 4.98, 8.41, 15.35, and 22.22 GHz. For the 2015 observations, the total time on source was 70 min at 5 GHz, 260 min at 8 GHz, 290 min at 15 GHz, and 330 min at 22 GHz. 3C84 and 3C111 were observed for bandpass and gain calibration, respectively. The data recording rate was 2048 Mbps with two bit sampling. Each frequency was measured over eight intermediate frequencies (IFs) such that every IF consisted of a bandwidth of 32 MHz across 64 channels in both circular and their respective cross polarizations.

Standard data reduction steps including flagging, instrumental time delay, bandpass corrections, and frequency averaging were performed with the NRAO Astronomical Image Processing System (AIPS) (Ulvestad et al., 2001, van Moorsel et al., 1996). For all iterative self-calibration methods the initial model was a point source. Further cleaning, phase and amplitude self-calibration were executed manually using Difmap (Shepherd et al., 1995). The source structure was later model-fitted in the visibility (u, v) plane with Difmap using circular and elliptical Gaussian components.

Fully calibrated VLBI archival data from the 2003 epoch (Maness et al., 2004) at 15 GHz, and the 2005 (Rodriguez et al., 2006) epochs at 5, 8, 15 and 22 GHz, have been included to study the core component motion with frequency and time. The visibilities were imaged and model fitted in Difmap, as with the 2009 and 2015 data, to obtain the core positions. The calibrator 3C111 has been observed in the same configuration across all four epochs. Details of the observations can be found in Table 2.1 .

2.3 Measurement and Fits

The new 2015 data set provides the most sensitive measurement of the source geometry. Using model fitting in Difmap to the visibilities we determine the Gaussian size, axis ratio and position angle for each core component. These measurements are listed in Table 2.2. Additional Gaussian components are included in each model to account for the extended structure. We then follow Rodriguez et al. (2006) and Maness et al. (2004) in fixing these parameters in fits to the other epochs, while allowing only the positions and fluxes of C1 and C2 to vary. These are listed in Table 2.3, with the relative positions listed as angular separation r and position angle θ measured north through east. The reported flux density errors combine the map rms σ_{rms} and an estimated systematic error in quadrature: $\sigma_S = [(0.1S_\nu)^2 + \sigma_{\text{rms}}^2]^{1/2}$.

The effective position errors are more difficult to estimate. The statistical errors $\approx a/2(S/N)$ (Fomalont, 1999) are very small ($\sim 2 \mu\text{as}$), and systematic effects certainly dominate. We made an initial check on these errors, by re-doing the previous Stokes I map analysis in Stokes LL and RR. 0402+379 is an unpolarized source so we expect data from both Stokes RR and LL to yield similar distance measurements. Another way to obtain these error estimates is to split the data in time or frequency. However, these maps would have a different (u,v) coverage, thus making it difficult to make a comparison between them. If the polarization-dependent structure differences are small as expected, then any measured differences can be attributed to systematic errors. This technique has been discussed previously by

Roberts et al. (1991) and McGary et al. (2001). Decomposing the relative positions into RA(x) and DEC(y), we find that the median shifts in the core centroid positions are $\sigma_x = 7 \mu\text{as}$ and $\sigma_y = 8 \mu\text{as}$ for the higher frequencies, and $\sigma_x = 31 \mu\text{as}$ and $\sigma_y = 34 \mu\text{as}$ at 5 GHz.

2.3.1 Analysis

The core component flux density arises from the surface at which the self-absorption optical depth is unity (Blandford and Königl, 1979). Since this is strongly frequency dependent, we expect an asymmetric extended structure, such as the jet base which defines the core, to have a frequency-dependent centroid. This effect is very obvious in the raw positions (Fig. 2.2), where the lower frequency centroids are shifted to the NE along the larger scale outflow position angle (Fig. 2.1a). Similar shifts have been detected in a number of AGN (Lobanov, 1997, Sokolovsky et al., 2011). Since we are measuring position relative to C1, any extension to that source may also contribute to the relative core shift; this need not be at the same position angle. However the combined shift appears to be dominated by C2 and we indeed find that the frequency-dependent shift is along the 47° (N-E) position angle of the C2 outflow. According to Lobanov (1997) the shift can be parameterized as $r_c = a\nu^{-1/k}$, where a is the shift amplitude and k depends on the jet geometry, particle distribution and magnetic field. For example a conical jet with a synchrotron self-absorbed spectrum gives $k = 1$ (Lobanov, 1997).

By correcting to an infinite frequency we can mitigate the effect of this core shift on the position of the nucleus (Fig. 2.3). We are of course especially interested in the relative motion of C1 and C2 and so our model includes a fiducial relative position (at epoch 2000.0) as well as relative proper motion in RA and DEC. Thus our model has six fit parameters (if we include the core shift position angle as a fit parameter, we do indeed obtain $46 \pm 1^\circ$, but prefer to fix this via the larger scale jet axis). Our data set are the 13 r, θ (x, y) position pairs over four epochs and four frequencies, so the fit has $26 - 6 = 20$ degrees of freedom (DoF).

Using our measurements and the position error estimates above, we performed a χ^2 minimization to determine the model parameters. These are listed in Table 2.4. The parameter error estimates are somewhat subtle. Since the fit minimum has $\chi^2/\text{DoF} = 2.78$, we must have systematic errors beyond those estimated above. The conventional approach is to uniformly inflate all errors until the effective $\chi^2/\text{DoF}=1$. This is equivalent to estimating errors using the χ^2 surface with increases of $+1, +2 \dots \times \chi^2/\text{DoF}$. We list these “1 σ ” and “2 σ ” confidence intervals in Table 2.4.

However, this uniform inflation assumes that all errors have a Gaussian distribution and are equally underestimated. This is unlikely to be true. An alternative approach is to estimate errors via a bootstrap analysis (Efron 1987). This has the virtue of using only the actual data values (not the error estimates), but does pre-suppose that the observed data values are an unbiased draw from an (unknown) error distribution about the true values. Although our set of 13 position pairs is somewhat small for a robust bootstrap, we generated 10,000 re-sampled realizations of the data set, replacing five pairs in each realization with random draws from the remaining pairs. Each realization was subject to the full least-squares fit for all model parameters. The histograms of the fit values for the individual parameters were used to extract 95% confidence intervals for each quantity. These confidence intervals are listed in Table 2.4. They accord fairly well with the inflated χ^2 estimates.

In general, the parameters appear well-constrained. The core-shift coefficients a and k are estimated to $\sim 3\%$ accuracy (Table 2.4). The epoch position range is somewhat larger in the bootstrap error analysis, evidently as a result of the substantial offset of the 2009.9 position from the general trend.

The coefficient k depends on the shape of electron energy spectrum, magnetic strength and particle density distribution (Lobanov, 1997). If $k=1$, it implies that the jet has a conical shape, where synchrotron self-absorption is the dominant absorption mechanism. We have obtained $k = 1.591 \pm .232$ (via the bootstrap technique), in accordance with the literature (Sokolovsky et al. (2011)) where the highest reported k value is ~ 1.5 . This implies that our observations are consistent with the synchrotron self-absorption mechanism.

The core-shift depends mainly on the frequency as well as the magnetic field and spectral index (Lobanov, 1997). All our measurements are derived from the same frequencies over time, however, there is a possibility of variation with magnetic field and spectral index. We calculated the spectral index for three epochs (2005, 2009 and 2015) using the peak intensities, and we have found these values to range from -0.58 to -0.98 and -0.43 to -0.50 for C1 and C2 respectively. From these ranges of spectral index, we can see that the variation over 10 years is quite small (~ 0.4). To our knowledge, no time varying core-shift offsets have been reported in the literature. For our analysis, we assume that the core-shift is constant over time.

In Fig. 2.3 we plot the relative C2 core position, shifted to infinite frequency according to the best-fit a and k , for each of the 13 observation frequencies and epochs. The plotted error ellipses for the 8, 15 and 22 GHz observations are the formal σ_x and σ_y from the polarization analysis. There are large outliers, especially the 2009.9 epoch. However, the overall shift is quite significant with motion detected in both RA and DEC, at $> 3 \sigma$ in the χ^2 analysis and at well over 95% confidence in the bootstrap analysis. Additional epochs, especially at high frequency will, however, be needed to make the motion visually clear.

To compare these above results, we also studied the motion of jet components. We find that the bright southern jet components continue to move away from the core, consistent with the previous results (Rodriguez et al., 2006). For the weaker northern hotspot, the agreement is not as good, as it seems to exhibit inconsistent motion for some frequencies. However, this may be the result of errors in the previous measurements based on 5 GHz observations.

Using our best-fit μ_{RA} and μ_{Dec} , we shift the raw data points (Table 2.4) to epoch 2000.0. For each frequency, we obtain an average relative RA and DEC, which are subsequently subtracted from the fiducial 2000.0 point (Table 2.4) to obtain the distance from the core (r_c). This has been plotted to demonstrate our fitted frequency dependence, shown in Fig. 2.4. The plotted errors have been obtained by error propagation using the above stated errors (σ_x and σ_y).

2.3.2 Magnetic Field Estimate

The core-shift effect is useful to deduce various jet related physical parameters, including the magnetic field strength. Lobanov (1997) and Hirotani (2005), for example provide a derivation that assumes equipartition between the particle and magnetic field energy densities in the jet. An alternate formulation by Zdziarski et al. (2015) avoids the equipartition assumption, using the flux density F_ν at a jet axis distance h to estimate the magnetic field strength as

$$B_F(h) = \frac{3.35 \times 10^{-11} D_L[\text{pc}] \delta \Delta\theta[\text{mas}]^5 \tan\Theta^2}{h[\text{pc}] (\nu_1^{-1} - \nu_2^{-1})^5 [(1+z)\sin i]^3 F_\nu[\text{Jy}]^2} \quad (2.1)$$

where z is redshift, D_L is the luminosity distance in pc, $\delta = [\Gamma_j(1 - \beta_j \cos i)]^{-1}$ is the Doppler factor, Γ_j is the minimum Lorentz factor, β_j is the jet bulk velocity factor (obtained from Rodriguez et al. (2009)), i is the inclination angle, $\Delta\theta$ is the observed angular core shift (Lobanov 1998), and $\Theta = \arctan \frac{\sqrt{d^2 - b_\phi^2}}{2r}$ is the jet half opening angle (Pushkarev et al., 2012). From the latest 8 GHz map, we have obtained the full width at half maximum of a Gaussian fitted to the transverse jet brightness component, $d = 4.130 \pm 0.017$ mas (minor axis of jet); the beam size along the jet direction, $b_\phi = 1.26$ mas; and the distance to the core along the jet axis, $r = 26.320 \pm 0.017$ mas. Since the extended jet components are not readily detected at 15 and 22 GHz, we assume the same opening angle for all frequencies. Table 2.5 gives our estimated values for these parameters, with the origins in the footnotes. The numerical constant in the above equation has been obtained for $p = 2$, where p is index of the electron power law (see Zdziarski et al. (2012, 2015)).

From a weighted linear fit of $\delta\theta$ against $\nu_1^{-1} - \nu_2^{-1}$, we obtain a slope = 1.128 ± 0.152 and intercept = 0.008 ± 0.010 . Instead of calculating $\frac{\delta\theta}{\nu_1^{-1} - \nu_2^{-1}}$ for each frequency separately, its slope has been used in calculating the magnetic field strength. Our fit indicates a magnetic field strength 0.71 ± 0.25 G at $h = 1$ pc, similar to that for other jets (O’Sullivan and Gabuzda, 2009).

2.3.3 Orbital Models

Our measured proper motion $\mu_{\text{RA}} = -0.89 \pm 0.07 \mu\text{as/y}$, $\mu_{\text{Dec}} = 1.29 \pm 0.10 \mu\text{as/y}$ (symmetric width of the 95 % CL bootstrap range) corresponds to a proper motion μ of $1.57 \pm 0.08 \mu\text{as/y}$ at $PA_{\mu} = -34.6 \pm 2.9^{\circ}$ (if we use the “1 σ ” χ^2 errors, the amplitude uncertainty is $\pm 0.38 \mu\text{as/y}$). Thus this is at least a 4 σ detection. It is consistent with the non-detection of a proper motion in Rodriguez et al. (2006), where 15 years of 5 GHz data (1990-2005) were used to estimate $\mu = 6.7 \pm 9.4 \mu\text{as/y}$; our higher frequency data and core-shift correction are essential for measuring the much smaller motion.

We now ask if this proper motion is consistent with a shift due to the relative orbits of the two BH. At $z = 0.055$, it corresponds to a projected space velocity of $\beta = v/c = 0.0054 \pm 0.0003$, so a Keplerian analysis suffices. First, the ratio $2\pi r/\mu = 2\pi \times 7.02 \text{ mas}/0.00157 \text{ mas/y} = 28,000 \text{ y}$ gives a characteristic orbital timescale. Thus over our 12 y baseline, the core position PA has rotated by less than a degree. This does not allow us to fit for precise orbital parameters. In particular, we have four measurements from the VLBI analysis (relative position and proper motion) while we need six parameters to define the relative orbit.

We note that the above derived $\sim 28000 \text{ y}$ period is rather close to the Earth’s spin axis precession period of $\sim 26000 \text{ y}$, we believe this to be a coincidence. The differential astrometry performed here should not be expected by precession as that term has been removed with the correlator model and affects both the sources in an identical way.

If we assume circular motion ($e = 0$), then we can determine the relative orbit in terms of one additional free parameter. In practice it is easiest to select the PA of the projected orbit normal (measured N through E) and then resolve the relative positions x and y (in mas) and relative velocities v_x and v_y (in mas/y) in this rotated coordinate system. Then the orbit parameters are

$$v = (v_x^2 - v_x v_y x/y)^{1/2}$$

$$\begin{aligned}
a &= -(x^2 - x y v_x / v_y)^{1/2} \\
\cos(i) &= [-y v_y / (x v_x)]^{1/2} \\
\theta &= \pi + \text{atan} \left([-y v_x / (x v_y)]^{1/2} - [1 - y v_x / (x v_y)]^{1/2} \right)
\end{aligned}$$

where a and v are the relative orbit radius and velocity, i is the inclination and θ gives the phase at our observation epoch. In fact it is more interesting to plot the total mass $M = v^2 a / G$ and period $P = 2\pi a / v$ against the orbit inclination i (Fig. 2.5). Note that with our assumption of a circular orbit only fairly large inclinations are consistent with our C1-C2 offset and relative motion (Fig. 2.3). Typical orbital periods are indeed 20-30ky, but the masses required by our apparent velocity are quite large $\geq 15 \times 10^9 M_\odot$. With our nominal fit errors, the minimum mass is $M_g = 15.4 \pm 1.3$. If one relaxes the $e = 0$ assumption, smaller masses are allowed, but then the solution is nearly unconstrained.

The orbital eccentricity grows as the orbit shrinks since both stars and gas extract energy and angular momentum from the binary. For a stellar background, it depends on the mass ratio, with equal mass binaries producing orbits that are usually circular or slightly eccentric with $e < 0.2$ (Merritt et al., 2007). If a pair during the binary formation starts out with a non-zero eccentricity it may never become circular instead it tends to become more eccentric (Matsubayashi et al., 2007). In the case of gas driven mergers, it depends on the disc thickness and the SMBBH's location inside the disc. The critical value of e is reported to be ~ 0.6 , such that system with high eccentricities tend to shrink to this value (Armitage and Natarajan, 2005, Cuadra et al., 2009, Roedig et al., 2012). In the case of 0402+379, it has been found to be embedded in cluster gas (Andrade-Santos et al., 2016), which makes it likely to have a non-zero eccentricity.

In Rodriguez et al. (2009) HI absorption measurements were used to infer kinematic motion about an axis inclined $\sim 75^\circ$ to the Earth line of sight, passing through C2, the origin of the kpc-scale jets. If we look at the solution derived here we see that the $PA = 47^\circ$ axis corresponds to $i = 71.3^\circ$ (Fig. 2.5 & Fig. 2.6), in reasonable agreement with the HI estimate. The binary spin can be different from the orbital

angular momentum, however, it's been found that if the amount of gas accreted is high (1-10% of the black hole) on the timescales of binary evolution, it can change according to the orbital axis (Schnittman (2013), and references therein). Binary orbital axis and individual black hole spins tend to realign due to interaction with external gas except when the mass ratios are extreme ($\gg 1$) whereas, torques from stars can cause misalignments of the binary orbit orientation from the disc (Miller and Krolik, 2013). For this fit we have $P = 49$ ky and $M = 16.5 \times 10^9 M_{\odot}$.

Because we find a large proper motion μ we expect the orbital motion to induce a substantial radial velocity in the relative orbit. Some values are given in Fig. 2.6 and for $PA = 47^{\circ}$ we expect a relative $v_r = 700$ km/s. While the HI measurements do show velocity differences of this order, we do not see such large velocities in the optical line peaks. Examining the Keck spectra in Romani et al. (2013) we see that the stellar features of the elliptical host center on $16,618 \pm 53$ km/s, while the Seyfert I-type narrow-line core emission centers on $16,490$ km/s. Narrow line emission extends several arcsec from the core spanning ~ 300 km/s while in the unresolved kpc core the velocity dispersion is ~ 750 km/s. Thus, while at least $2 \times 10^{10} M_{\odot}$ lies within the central kpc, we do not see multiple components shifted by > 500 km/s. However, the full line width does accommodate such velocities and the wings of the $H\alpha$ complex are centered at $\sim 17,020$ km/s suggesting that fainter broad line emission might include components spread over > 1000 km/s. Further v_r above is the relative velocity; if only the heavier component has bright optical emission, then the broad line velocity shift from the background galactic velocity (arguably near the center of mass velocity) will be reduced to mv_r/M_{Tot} . Indeed, Rodriguez et al. (2009) assume that the jet-producing C2 core is the dominant mass and the center of rotation. If this core also dominates the broad line emission, then we expect that our VLBI relative velocity is dominated by the motion of C1 and the optical radial velocity shift from the host velocity may be small.

We must also compare with other core mass estimates. As noted above the optical lines indicate several $\times 10^{10} M_{\odot}$ in the central kpc. HI absorption velocities require $> 7 \times 10^8 M_{\odot}$ (Rodriguez et al., 2009). And finally the host bulge luminosity also

indicates a large hole mass $M_{\bullet} \sim 3 \times 10^9 M_{\odot}$ (Romani et al., 2013). All of these suggest substantial hole mass. The very large $M_9 \sim 15$ masses implied by our fits are not excluded but do stretch the available mass budget.

2.3.4 Comments on the resolved SMBBH Population

The process of hierarchical merging should make close SMBBH common, but to date few candidates at sub-kpc separations have been seen. The resolved (massive) SMBBH seem to be preferentially in galaxy clusters or their products. For example the SMBBH candidate RBS 797 (Gitti et al., 2013) resides in a cool-core cluster at $z=0.35$. 0402+379 itself lies in a massive galaxy and dense X-ray halo (likely a fossil cluster) at $z = 0.055$. So such environments seem to be a good place to look for additional systems. Another path to discovering multi-BH nuclei has been described by Deane et al. (2014) who find J1502+1115 to be a *triple* system, with a closest pair separation of 140 pc at redshift $z=0.39$. Compact radio jets in the closest pair of this source exhibit rotationally symmetric helical structure, plausibly due to binary-induced jet precession. However the total number of resolved compact cores at pc scales seems very small with 0402+379 remaining the only clear example out of several thousand mapped sources (Burke-Spolaor, 2011, Tremblay et al., 2016).

Of course systems of even smaller separation are of the greatest interest since at $r \sim 0.01$ pc losses from gravitational radiation will dominate and the merging binaries can be an important signal in pulsar timing studies (Ravi et al., 2015). At present, we rely on arguments about evolution of the wider systems to infer the existence of merging SMBBH. If such evolution occurs we might hope for a discovery of an intermediate $r \sim 0.1$ pc scale massive $> 10^9 M_{\odot}$ system at low z where sufficient resolution for a kinematic binary study is possible with high frequency VLBI. Such a binary would have $P < 10^3$ y and a well-constrained visual orbit should be achievable, making possible a precision test of the SMBBH nature (Taylor, 2014). However, we should note that our study of the galactic halo of 0402+379 (Andrade-Santos et al., 2016) implies that it has stalled at its present 7 pc separation for several Gyr, so

the path between resolvable and gravitational radiation-dominated SMBBH may not always be smooth.

2.4 Conclusion

In this study of 0402+379, we have focused on two aspects: frequency dependent core-shift and secular relative core motion. Both effects are observed, but the measured values present interpretation challenges.

The strong observed core-shift matches well with the large-scale jet axis. It also provides quite typical estimates for the jet base magnetic field of $\sim 0.45 - 0.95$ G. However the core-shift index 1.591 (1.556-1.823 95% CL range) is somewhat large (expected $k \sim 1$), with the highest reported value in literature is $k \sim 1.5$ (Sokolovsky et al., 2011). This may be an artifact of our constant core-shift fit assumption, as perturbations could arise from the epoch-to-epoch variation in the underlying core component fluxes.

After accounting for this core shift the infinite frequency relative positions of the C1 and C2 cores undergo a statistically significant secular proper motion. The motion corresponds to $\beta = 0.0054 \pm 0.0003$ and, if orbital, it represents the first direct detection of orbital motion in a SMBBH, and promotes this system to a visual binary. Although we do not have sufficient observables to solve for an orbit, we can find plausible orbits, even assuming $e = 0$. Intriguingly such orbits align well with the large scale jet axis and have similar inclination to those estimated with HI absorption VLBI. But the required masses are quite large (highest reported mass is 21 billion M_{\odot} , McConnell et al. (2011)). To test our orbital picture, additional VLBI epochs to confirm the consistency of the proper motion will be essential, and further studies of the core dynamics, especially at sub-kpc scales will also be very important. We should not forget that including a finite orbital eccentricity can allow smaller masses, but we will need additional kinematic constraints to motivate such solutions.

Thus discovery of possible orbital motion in 0402+379 presents the exciting

prospect of probing a SMBBH's kinematics. Certainly, extensions to our high frequency VLBI campaign can improve the measurements, but this proper motion is perhaps the most exciting as a spur to searches for tighter, faster and more easily measured examples of resolved SMBBHs.

Acknowledgements:

This research has made use of NASA's Astrophysics Data System. English translations of Einstein (1916) and Einstein (1918) made available via The Digital Einstein Papers of the Princeton University Press aided the preparation of this paper. The National Radio Astronomy Observatory is a facility of the National Science Foundation operated under cooperative agreement by Associated Universities, Inc.. Partial support for this work was provided by the National Aeronautics and Space Administration through Chandra Award Number GO4-15121X issued by the Chandra X-ray Observatory Center, which is operated by the Smithsonian Astrophysical Observatory for and on behalf of the National Aeronautics Space Administration under contract NAS8-03060.

Table 2.1: Observations

Frequency (GHz)	Date	Integration time (min)	BW (MHz)	Polarization	IF	Reference
4.98	01/24/2005	69	8	2	4	Rodriguez et al. (2006)
4.98	12/28/2009	286	32	4	4	This paper
4.98	06/20/2015	70	32	4	8	This paper
8.15	06/13/2005	69	8	2	4	Rodriguez et al. (2006)
8.15	12/28/2009	261	32	4	8	This paper
8.15	06/20/2015	261	32	4	8	This paper
15.35	03/02/2003	478	16	2	4	Maness et al. (2004)
15.35	01/24/2005	122	8	2	4	Rodriguez et al. (2006)
15.35	12/28/2009	292	32	4	8	This paper
15.35	06/20/2015	286	32	4	8	This paper
22.22	06/13/2005	251	8	2	4	Rodriguez et al. (2006)
22.22	12/28/2009	325	32	4	8	This paper
22.22	06/20/2015	334	32	4	8	This paper

Table 2.2: Stationary Gaussian Model Components

Frequency (GHz)	$a(\text{C1})$ (mas)	$b/a(\text{C1})$	$\phi(\text{C1})$ ($^{\circ}$)	$a(\text{C2})$ (mas)	$b/a(\text{C2})$	$\phi(\text{C2})$ ($^{\circ}$)
5	0.563	0.000	82.80	1.270	0.130	6.60
8	0.451	0.420	74.00	0.420	0.490	8.60
15	0.249	0.360	77.00	0.230	0.000	21.40
22	0.218	0.160	78.90	0.170	0.390	27.80

Fixed model parameters of Gaussian components for C1 and C2 of the model brightness distribution at each frequency. These are: a , semi-major axis; b/a , axial ratio (where b is semi-minor axis); Φ , component orientation for both C1 and C2. All angles are measured from North through East.

Table 2.3: Variable Gaussian Model Components

Epoch	Frequency (GHz)	$S_\nu(C1)$ (Jy)	$S_\nu(C2)$ (Jy)	r (mas)	θ ($^\circ$)
2005.07	5	0.057 ± 0.005	0.014 ± 0.001	6.942	-75.70
2009.99	5	0.058 ± 0.005	0.016 ± 0.001	6.841	-75.93
2015.43	5	0.060 ± 0.006	0.013 ± 0.001	6.884	-75.79
2005.45	8	0.067 ± 0.006	0.016 ± 0.002	6.913	-76.46
2009.99	8	0.052 ± 0.004	0.017 ± 0.002	6.920	-76.42
2015.43	8	0.083 ± 0.008	0.018 ± 0.002	6.913	-76.33
2003.17	15	0.070 ± 0.007	0.020 ± 0.002	6.929	-76.96
2005.07	15	0.054 ± 0.005	0.016 ± 0.002	6.959	-76.81
2009.99	15	0.029 ± 0.003	0.012 ± 0.001	6.985	-76.96
2015.43	15	0.058 ± 0.005	0.015 ± 0.001	6.956	-76.77
2005.45	22	0.037 ± 0.003	0.011 ± 0.001	6.950	-77.08
2009.99	22	0.020 ± 0.002	0.011 ± 0.001	6.984	-77.16
2015.43	22	0.040 ± 0.003	0.012 ± 0.001	6.969	-77.04

Variable model parameters of Gaussian components for C1 and C2 of the model brightness distribution at different epoch and frequency. These are as follows: S_ν , flux density at each frequency; r , θ , polar coordinates of the center of the component C2 relative to the center of component C1 (it has been assumed to be at a fixed position). Errors in flux have been estimated using both flux systematics and map rms ($\sqrt{((0.1 * S_\nu)^2 + rms^2)}$).

Table 2.4: Fitting Parameters

Parameters	Value	Technique		χ^2	
		Bootstrap (95%)		1 σ	2 σ
ΔRA_0 (mas)	-6.863	-6.892, -6.855		-6.859, -6.868	-6.858, -6.869
ΔDEC_0 (mas)	1.474	1.448, 1.478		1.470, 1.478	1.468, 1.480
μ_{RA} (μ as/y)	-0.887	-0.970, -0.831		-1.245, -0.549	-1.389, -0.405
μ_{DEC} (μ as/y)	1.286	1.200, 1.401		0.878, 1.672	0.713, 1.836
a (mas)	0.756	0.700, 0.818		0.739, 0.777	0.731, 0.785
k	1.591	1.556, 1.823		1.565, 1.617	1.555, 1.628

Fitted parameters values (Column 2) and their corresponding confidence intervals obtained from two different technique: bootstrap analysis (Column 3) and χ^2 minimization (Column 5 & 6). ΔRA_0 and ΔDEC_0 are infinite frequency core offsets at epoch 2000.0; μ_{RA} and μ_{DEC} are proper motion estimates; a and k are core-shift fitting parameters ($r_c = a \nu^{(-1/k)}$).

Table 2.5: C2 Jet parameters

Redshift z	Luminosity Distance D_L (Mpc)	Half opening angle Θ ($^\circ$)	Bulk Velocity factor β_{app}	Inclination angle i ($^\circ$)	Lorentz factor Γ_j	Doppler Factor δ
0.055	242.2 ^a	4.29 ^b	0.4 ^c	71.3 ^d	1.077 ^e	1.11 ^f

^a Luminosity distance was obtained for cosmological model : $H_0 = 71 \text{ kms}^{-1}\text{Mpc}^{-1}$, $\Omega_\Lambda = 0.73$, $\Omega_M = 0.27$

^b Pushkarev et al. (2012)

^c Rodriguez et al. (2009).

^d Section 2.3.1.

^e Lorentz factor, $\Gamma_j = (1 + \beta_{app}^2)^{\frac{1}{2}}$ (Zdziarski et al., 2015).

^f Doppler factor, $\delta = [\Gamma_j(1 - \beta_j \cos i)]^{-1}$ (Zdziarski et al., 2015).

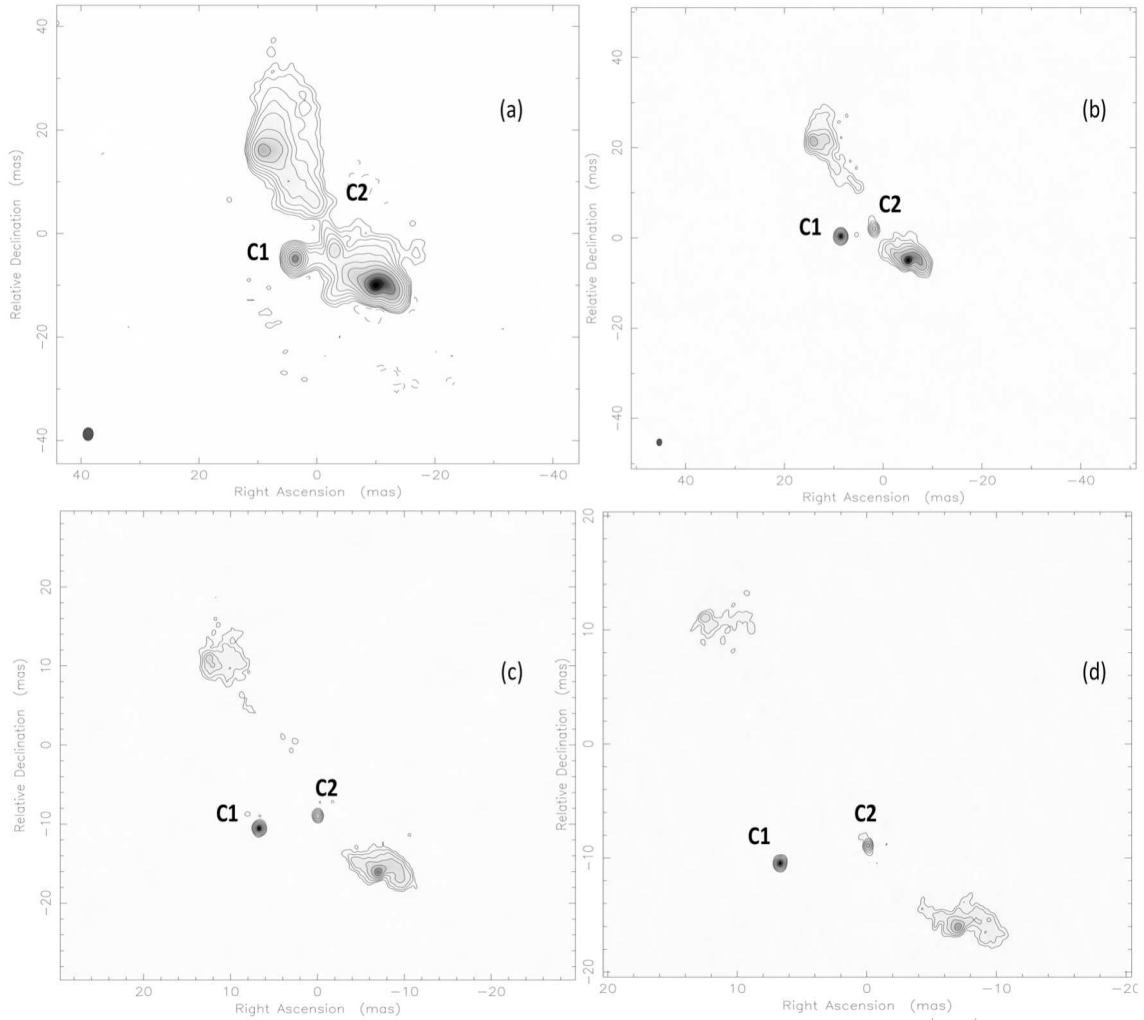


Figure 2.1: Naturally weighted 2015.43 VLBA maps of 0402+379 at 5, 8, 15 and 22 GHz. Designated C1 and C2, are the core components in 0402+379 (Maness et al., 2004, Rodriguez et al., 2006). Contours are drawn beginning at 0.15σ (a), 1σ (b), 1σ (c) & 1.5σ (d), and increase by a factor of 2 thereafter. (a) Note that the core components are slightly resolved here. There is a bridge between these two components, and we believe this is a jet emanating from C1, as has been discussed in this paper. (b) A jet emerging from C2, moving in the direction of hotspots can be identified here clearly. We have used this map to obtain the jet-axis angle. (c) A very faint jet emanating from C2, similar to 8 GHz map, can be seen here. (d) No jets are visible at this frequency.

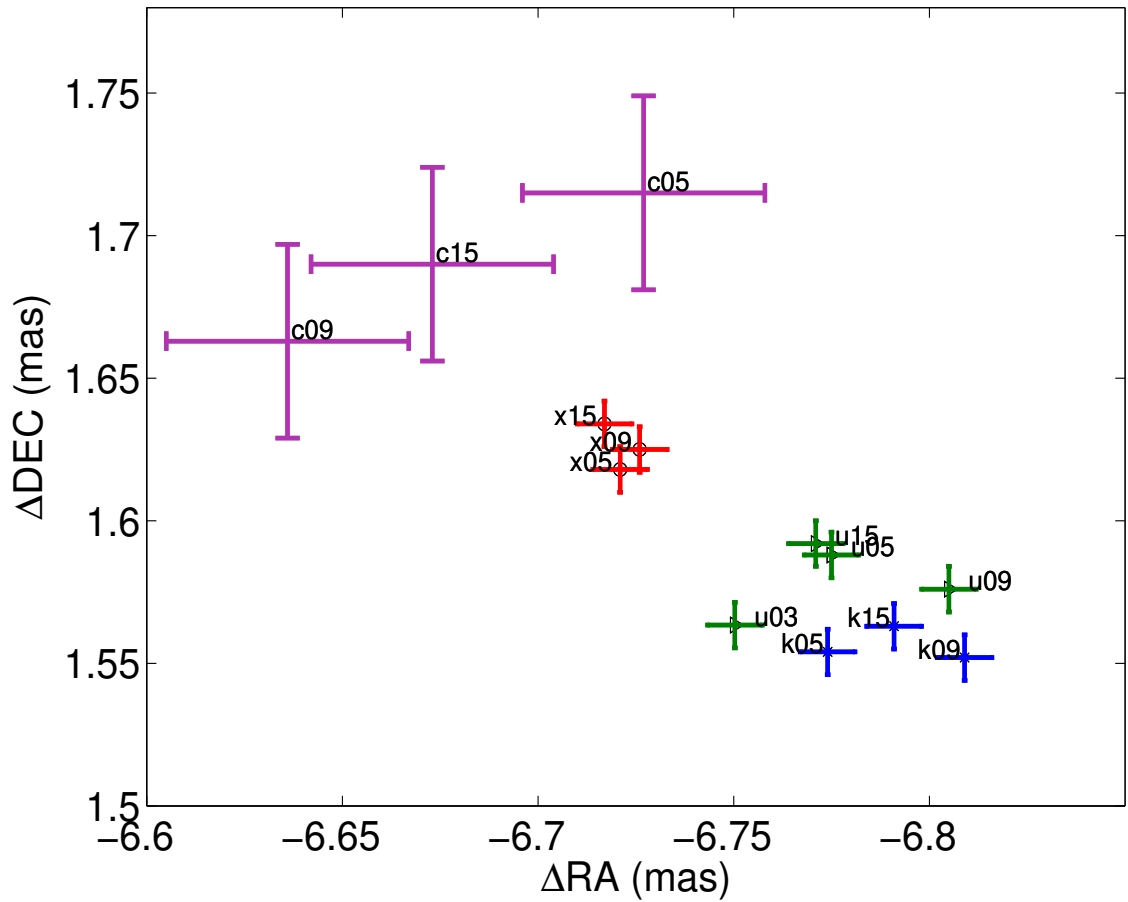


Figure 2.2: We have plotted projected relative RA *vs.* DEC of component C2 with respect to C1 (at origin), at 5 GHz (c's), 8 GHz (x's), 15 GHz (u's), and 22 GHz (k's). This is the raw, uncorrected, modelfit positions. An offset in position with frequency can be seen due to the core-shift effect discussed in the text.

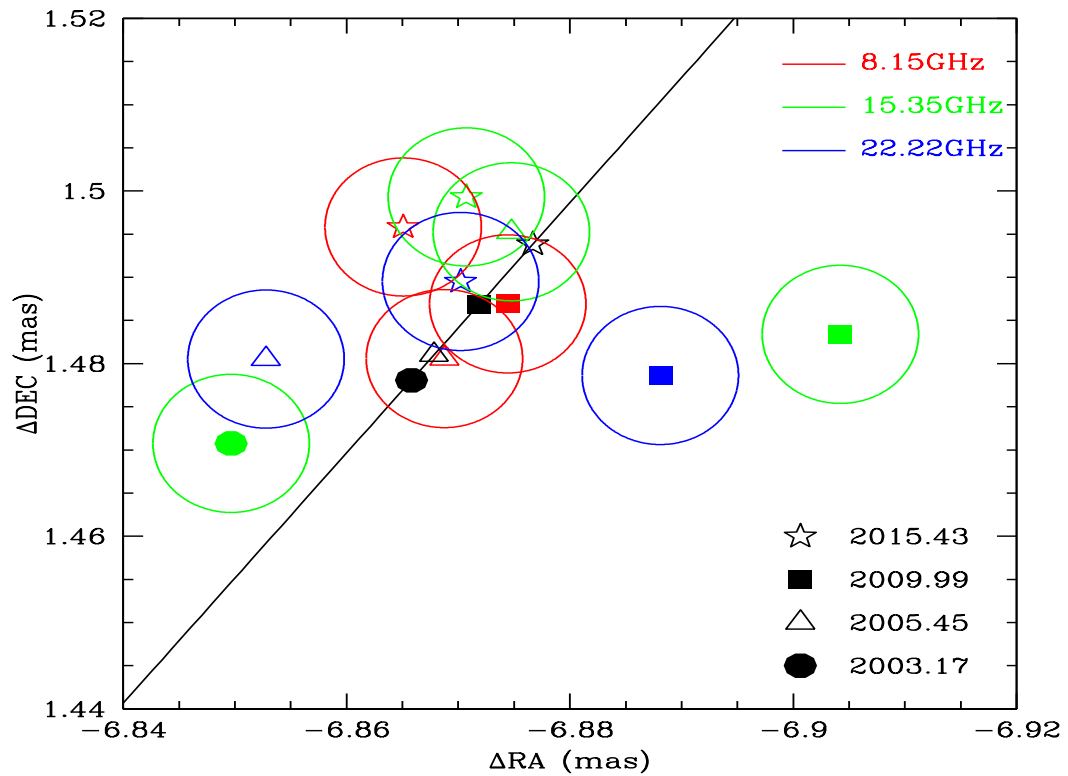


Figure 2.3: Position of C2 relative to C1 in time after removing the effect of the core shift. The black line is a proper motion fit; the best fit positions at each epoch are labeled by points along the line.

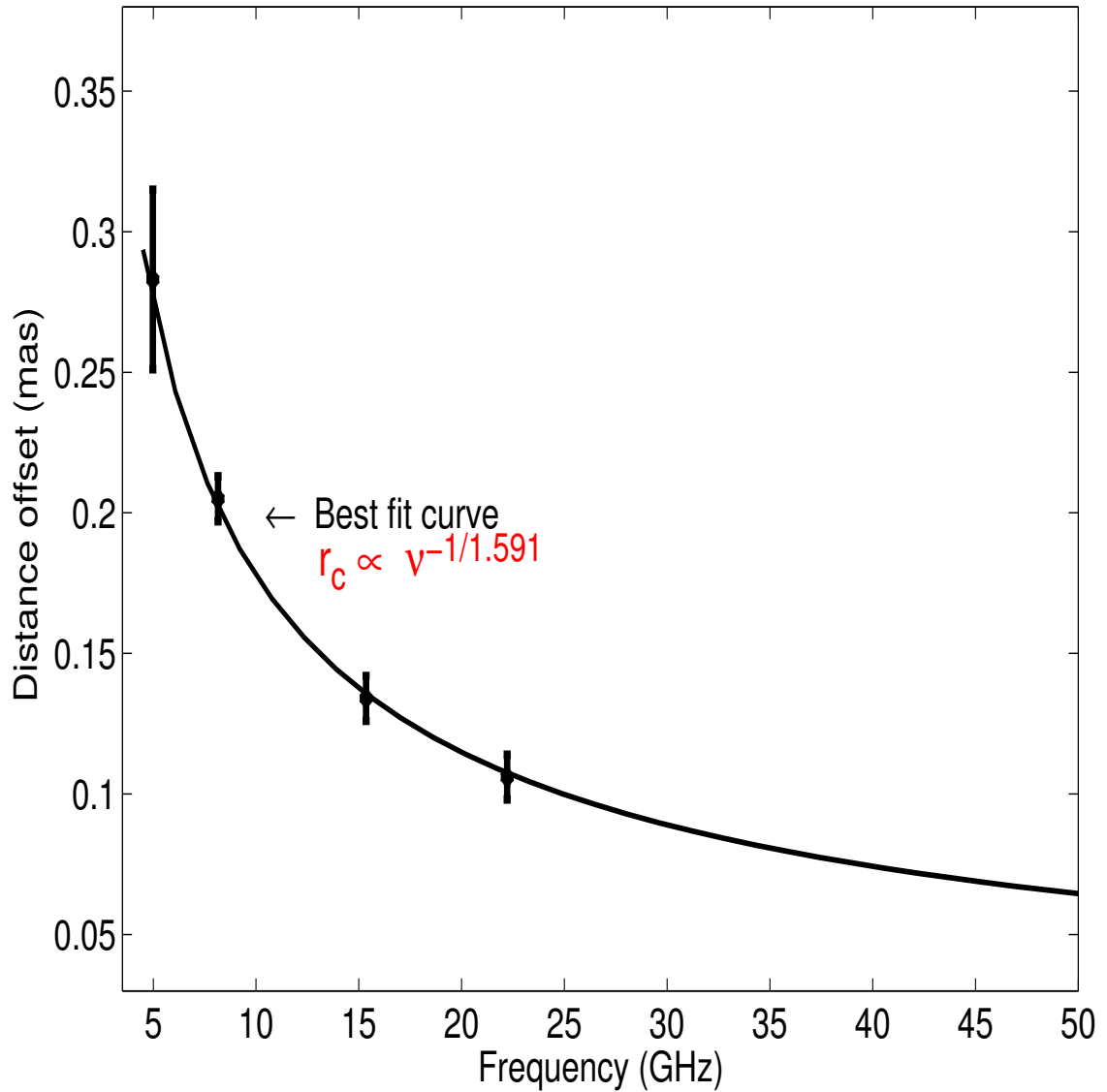


Figure 2.4: Plot of the core-shift measurement in distance from the central engine for 0402+379 as a function of frequency. Black circles are observed distance offset from estimated infinite frequency core position at each frequency, and the black solid curve is the fitted function, with $r_c = a(\nu^{(-1/k)})$ (See Table 2.5).

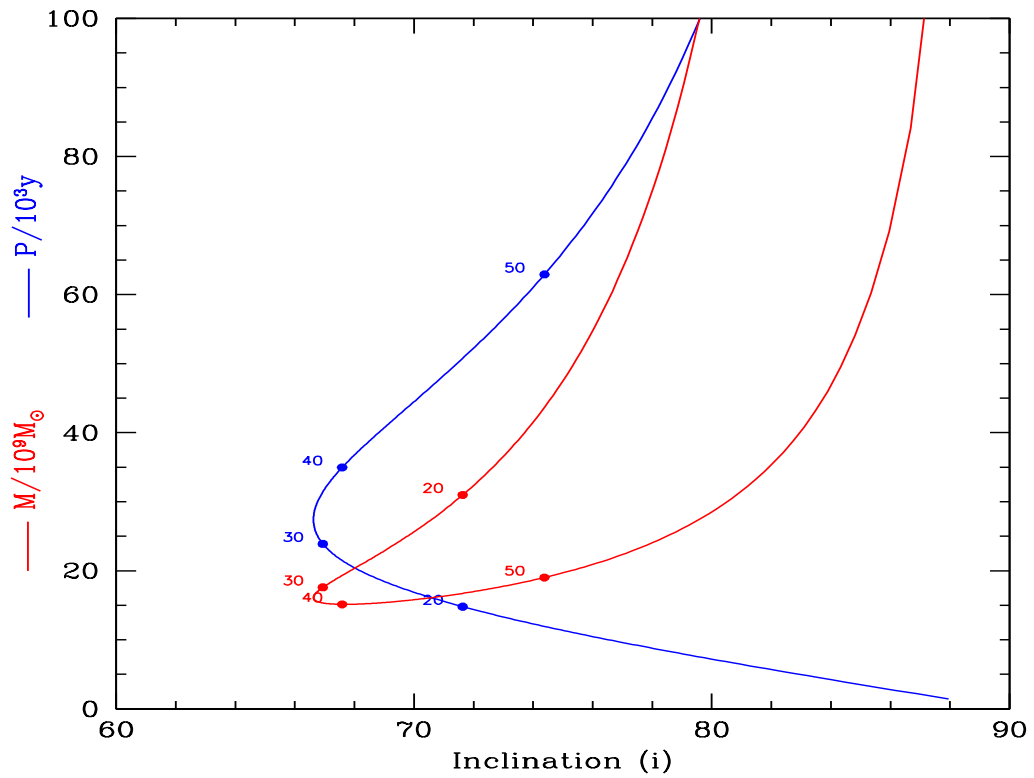


Figure 2.5: Orbital solutions for mass (red) and period (blue) as a function of inclination angle. Points mark solutions with the projected PA given by the label numbers (in degrees North through East).

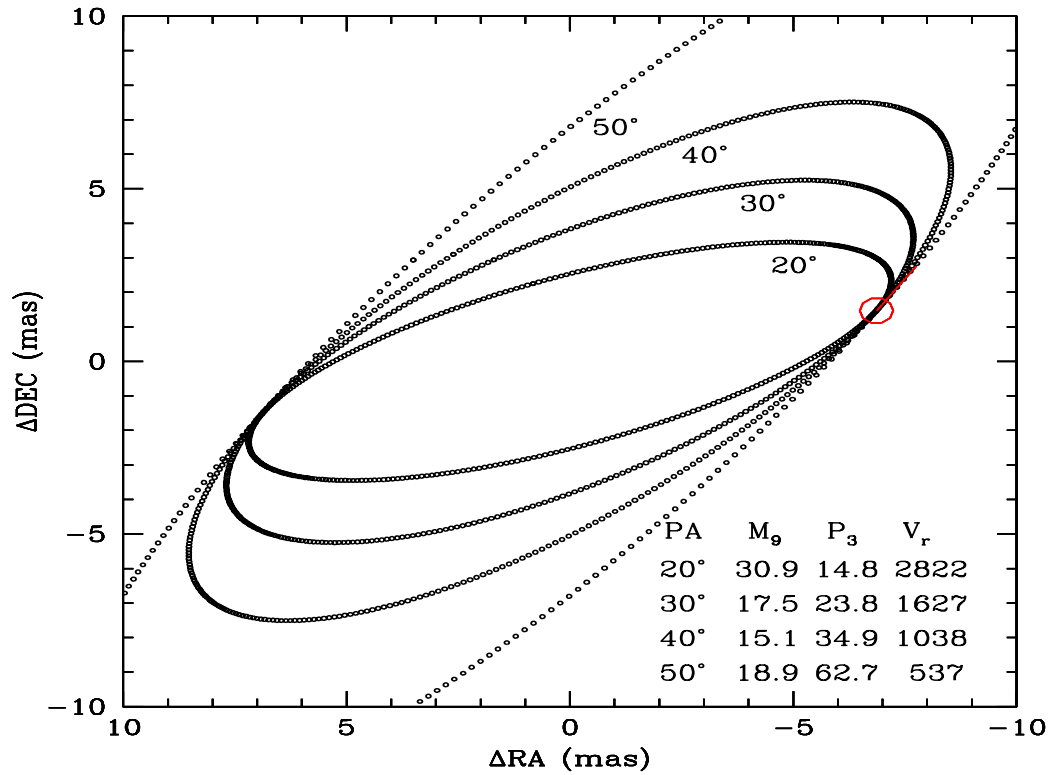


Figure 2.6: Circular orbit fits for the four PA values marked in figure 5. All are consistent with the observed offset and proper motion (red). The mass, period and relative radial velocity for the solutions for each PA value are listed in the figure.

Chapter 3

A Search for Compact Supermassive Black Holes

In this chapter, we report on a search for compact binary supermassive black holes. In our recent study of the most compact supermassive binary black hole (SMBBH) 0402+379, we found the orbital period to be ~ 28000 years. In order to study the orbital dynamics of SMBBHs within our lifetime, we need to search for compact systems that have a shorter orbital period, on the timescale of a few thousand years. For this purpose, we have selected a sample of 19 sources, of which 18 sources were previously observed using the very long baseline array (VLBA) at 5 GHz in the VLBA Imaging and Polarimetry Survey (VIPS). We now study these sources at higher frequencies, 15 and 22 GHz, using the VLBA to determine their true nature. Understanding the growth of black holes is of great interest in this new era of multi-messenger astrophysics as these are the preferred targets for planned gravitational wave observatories.

3.1 Introduction

Most large galaxies are thought to harbor a supermassive black hole (SMBH) (Richstone et al., 1998) at their center including our own Milky Way. Recently, the Event

Horizon Telescope for the first time imaged a SMBH residing inside M87 (Akiyama et al., 2019). This is a remarkable feat which also confirms the existence of supermassive black holes. Considering the cold dark matter cosmology model, galaxies are expected to evolve via the process of merging (Begelman et al., 1980). When both merging galaxies have an SMBH at their respective centers, it is expected to form an SMBBH system. Based on the separation between SMBHs, these systems can be classified into two categories: Dual AGNs (DAGN, \sim kpc) and SMBBHs (\sim pc). Despite numerous attempts, only a handful of systems have been found (Burke-Spolaor, 2011, Tremblay et al., 2016). This raises questions such as how do SMBHs evolve inside a merger? How often do galaxies collide? Does a collision give rise to a binary system, and how quickly do these black holes merge after binary formation? There is substantial evidence that the growth of a galaxy and SMBH are inter-related (Kormendy and Ho, 2013). Hence, understanding these SMBBH systems is crucial to understanding a variety of processes ranging from galaxy evolution in general to the evolution of black holes inside them.

Gravitational waves from merging black holes are expected as a result of Einstein's General Theory of Relativity. With the recent discovery of GWs (Abbott et al., 2016), their existence has been confirmed and a new exploring window has opened. However currently, this window is limited to the search of stellar mass black holes. While mergers of SMBBHs are expected to be common emitters of GW radiation, they have not yet detected any evidence for a GW signal. With the upcoming detectors such as evolving Laser Interferometer Space Antenna (eLISA, Amaro-Seoane et al. (2012)), it will be possible to detect low-frequency GWs (\sim mHz). Additionally, pulsar timing observations would be more sensitive to SMBBH mergers (Shannon et al., 2015) with nHz GWs .

In this study, our aim is to search for compact SMBBHs at redshift below 0.1 so that we are not too far away to attain the required resolution (at least 0.5 mas \sim 1pc) and sensitivity for their detection. These studies are also important to understand jet structures. For example, Bansal et al. (2017) studied the core-shift effect which enabled them to measure the magnetic field near the core. To pursue these goals, we

select a sample of 19 sources and observe them with the VLBA at 15 and 22 GHz. In Section 2, we describe the criteria used for candidate selection. Section 3 details the observations and data reduction technique. In Section 4, we discuss our results followed by conclusions and future work in Section 5.

3.2 Candidate Selection

Candidates were selected by redshift, galaxy bulge size, and on the basis of possible secondary nucleus or suggestion of a second axis. We have employed this rough estimate to cull the 1127 VLBI-imaged VIPS sources (Helmboldt et al., 2007), using cataloged redshifts and host magnitudes. VLBA studies and indications of a complex structure such that they could host double nuclei. In practice a large fraction of the short period candidates passed this inspection and, upon examination most were hosted by high mass ellipticals or S0s, often with substantial X-ray halos, further bolstering the likelihood of large hole mass. A few showed signs of a recent interaction. These are thus prime candidates for further VLBI study. Of course, these selection criteria do not guarantee that the sources host an SMBBH. However, they greatly increase the odds that if an SMBBH is present and resolved at scales below our 5 GHz limit, it will likely have an orbital period at least an order of magnitude less than that of 0402+379.

3.3 Observations and Data Reduction

We observed 19 sources using the VLBA at two frequencies 15.24 and 22.1 GHz. The data recording rate was 2048 Mbps with two-bit sampling. Each frequency was measured over eight intermediate frequencies (IFs) such that every IF consisted of a bandwidth of 32 MHz across 64 channels in dual polarization.

These sources were divided into four sections in the sequential order of their RA to have a better spatial (u,v) coverage. The first and second section was observed

on October 11, 2018. DA193 was used for fringe fitting and bandpass calibration. The third section was observed on November 8, 2018. Since the fringe finder for this section (J1423+4802) was not observed across all the antennas, we used another bright source in our sample J14197+5423. The fourth section was observed on November 29, 2018. Although 3C345 was observed as a fringe finder, data from antenna 3 (Hancock) was missing when this source was observed. So we instead used J2327+0940 which is a bright source and has been observed for long (~ 8 min) observation time intervals. List of observed sources, their redshift, and observation time at both the frequencies have been included in Table 3.1.

Initial data reduction was performed using the Astronomical Image Processing System (AIPS). This includes identifying the bad data points using POSSM plot and then subsequently flagging them using UVFLG. In VLBA, antennas are separated by a large distance which requires fringe correction to correct for the delay in the observations. We corrected for this phase delay using FRING which uses a bright source for a time range where it has been observed across all the antennas. These solutions were later applied to the remaining sources. Using the same time range of the fringe finder, bandpass solutions were obtained using BPASS. We then used VLBAUTIL, a script which applies a-priori amplitude corrections and digital sampling corrections. After applying the initial phase and amplitude calibration, we averaged the frequency channels in each IF and split out each source file.

Difmap was used for further cleaning and self-calibration. A point source model was used for iterative self-calibration except for NGC7674, which was phase-referenced using J2327+0940. NGC7674 is a weak source at both 15 and 22 GHz, hence cannot be self-calibrated.

3.4 Results

In this study, we attempted to search for SMBBHs in a sample of 19 sources using the VLBA. Since VLBA provides high resolution, we anticipated detecting SMBBHs

Table 3.1: Observational parameters comparison

Source	Redshift	Obs. Time	
		15 GHz (min)	22 GHz (min)
J07375+5941	4.062E-02	62	80
J08392+2850	7.902E-02	60	73
J09096+1928	2.796E-02	63	86.5
J09433+3614	2.233E-02	63	82.1
J11412+5953	1.147E-02	64	72.2
J11473+3501	6.289E-02	57.5	66
J11488+5924	1.079E-02	63.8	65.5
J11579+5527	3.646E-03	64	67
J12030+6031	6.533E-02	64.2	66.8
J12201+2916	2.254E-03	62.1	65.3
J12302+2518	1.350E-01	48.1	65
J12562+5652	4.146E-02	60.4	63.2
J13176+4115	6.614E-02	60.4	64.5
J14118+5249	7.647E-02	60.2	64
J14197+5423	1.520E-01	61.2	55.5
J16044+1744	4.093E-02	48	78.8
J16062+1814	3.694E-02	48	78.1
J17283+5013	5.499E-02	43	73.5
NGC 7674	2.892E-02	26	37.7

Notes: Redshift of each source; Duration of observation at 15 and 22 GHz.

while resolving them. Unfortunately, we do not detect any SMBBH. However, during our data reduction, we came across two interesting sources: NGC 7674 and Mrk 231. Below we discuss them in more detail.

3.4.1 NGC7674

NGC7674 was recently studied by [Kharb et al. \(2017\)](#), where they used archival VLBA data at 15 GHz. They reported a detection of two compact cores at a projected separation of 0.35 parsec, suggesting a compact SMBBH. The specified peak values for these cores, C1 and C2 are 0.74 and 0.76 mJy/beam. We have observed this source at two frequencies 15.24 and 22.1 GHz. To compare our results, we looked at the coordinates as mentioned in [Kharb et al. \(2017\)](#) for C1 and C2 and have

obtained the pixel value at $x = -17.2y = -14.8$ (mas) of 0.236 mJy/beam and at $x = -17.4, y = -14.8$ (mas) of 0.291 mJy/beam at 15 GHz. The rms noise for our data is 110 micro-Jy/beam as compared to 200 micro-Jy/beam as reported in Kharb et al. (2017), implying higher sensitivity for our data. Similarly, we see no detection at 22 GHz. This implies that previously suggested cores (Kharb et al., 2017) are likely not black holes but two noise bumps.

3.4.2 J1256+5562

Mrk 231 is a nearby ultraluminous infrared galaxy with relativistic jets. In this study, we have observed this source at two frequencies where it shows two bright components enveloped inside a lobe (Fig. 3.1). This observation appears very similar to 0402+379, which also consists of two bright components. This raised our interest in this source and we decided to further investigate it.

Mrk231 has also been studied at 2.3, 5, and 8 GHz using the VLBA (Taylor et al., 1999, Ulvestad et al., 1999), where it shows two lobes along the North-South direction (Fig. 3.2: Morganti et al., 2016) and an unresolved central component. These lobes get resolved out when observed at higher frequencies such as 15 GHz. The central unresolved component also starts to resolve in the 15 GHz map. We compare the 15 GHz map in Ulvestad et al. (1999) with our recent observation after accounting for the beam size. It appears that both the components align, suggesting no change in their relative position over about 20 years. This is consistent with the relative motion study in Reynolds et al. (2017), where they carried out a multi-epoch study of MRK 231 at 8, 15, 22, and 43 GHz using the VLBA. In their analysis, both the components are resolved at 43 GHz and show no relative motion over a timescale of about 9 years.

The component C1 shows nearly flat spectra with a turnover near 12 GHz, an indication of a compact core. On the other hand, C2 has a steeper spectrum (Reynolds et al., 2017, Ulvestad et al., 1999), likely a jet component. We fit for the Gaussian components at both 15 and 22 GHz using model fitting in Difmap (see Table 3.2)

Table 3.2: MRK 231 Gaussian Components

Components	Flux (mJy)	Major Axis (mas)	Ratio	Phi (deg)	Frequency (GHz)
C1	15.24	154.62	0.408	0.249	70.844
C2	15.24	219.40	0.258	0.747	-68.6962
C1	22.12	62.62	0.120	0.0	50.88
C2	22.12	107.3	0.246	0.6589	-55.486
C3	22.12	30	0.360	0.525	70.48

Model fitting components for MRK 231 at 15 and 22 GHz; their flux density; major axis size & ratio of major and minor axis, phase angle.

for the component details). At 15 GHz, there are only two components (C1 and C2) whereas there are three components at 22 GHz as component C1 splits into two (C1 and C3). The phase angle of C3 aligns with that of C2, suggesting a connecting jet. Reynolds et al. (2017) report detection of C1 and C2 and a flare emission component emanating from C1 directed towards C2. We note that this emission component was observed only at 43 GHz which differs from our observations. They also detected a change in the flux density of C2. From these observations, they suggested this flare is along the jet axis directed towards the secondary component.

In a separate study of MRK 231, Yan et al. (2015) suggest this source to be an SMBBH on the basis of its unique optical-UV spectrum. However, its true status can only be determined once we detect motion between C1 and C2. For a binary supermassive black hole, we expect it to move perpendicular to the line joining them which would not be true if C2 is a jet component.

3.5 Conclusion and Future Work

In this study, we have selected a sample of 18 sources from VIPS on the basis of their interacting morphology and an additional source NGC 7674, an SMBBH candidate. No SMBBHs were found. A non-detection of SMBBH in this sample raises various questions. First of all what morphology should be considered while searching for

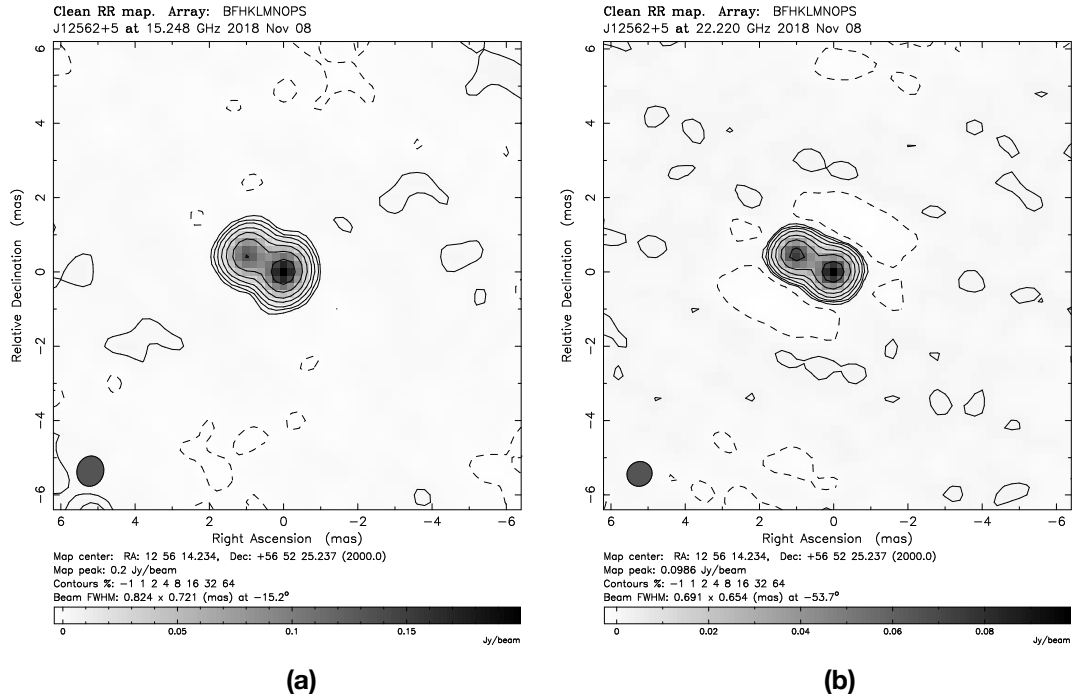


Figure 3.1: VLBA images of MRk231 at 15 GHz (a) and 22 GHz (b). Contours are drawn beginning at level 1σ and increasing by a factor of 2 thereafter. The data have been weighted with natural weighting scheme.

these candidates? We have selected sources which showed signs of a merger. A non-detection suggests that sources can show interactions without it being in an SMBBH. Or possibly the SMBBHs are still present in the lobe but require a higher resolution. In Mrk 231, we estimated the mass of the lobe using its luminosity and size and used it to obtain an estimate of the orbital period. However, as we go towards higher frequencies, the lobe starts to resolve out and actual luminosity will be lower implying lower mass and longer period.

Having defined the status of NGC7674 further strengthens the conjecture that these sources are rare or difficult to detect. A detection of GWs with PTAs will certainly confirm the SMBH mergers as well as help deduce their timescale. However,

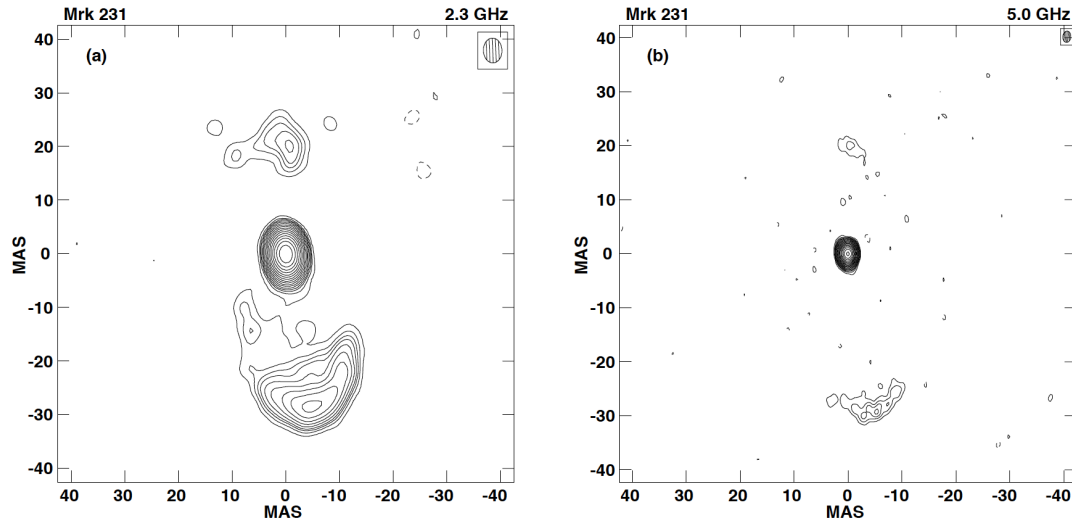


Figure 3.2: VLBA images of MRk231 at 2.3 GHz (left) and 5 GHz (right). Contour levels are the same multiples of the lowest contour. In both the maps, there are two lobes along the North-South direction and a central bright component. This figure has been adapted from [Ulvestad et al. \(1999\)](#).

the electromagnetic counterpart will enable us to probe their dynamics and deduce merger rates. Since only 10% of the quasars are radio loud, a multi-frequency approach extending to other frequencies such as optical, gamma-rays would be worth pursuing. In the literature, there are various different ways to search for these sources. First in the list is searching for double Broad Line Regions (BLR) as an initial test. Although this is not a foolproof technique as a Doppler shift in rotating discs or accretion discs around isolated SMBHs carries a similar signature. Another method includes periodic variation in luminosity. Several candidates including OJ287 and PKS 2247-131 have been identified using this technique where they show a variation in optical and gamma-ray flux, respectively, on the timescales of decades. In the future, a new search method can be developed which searches for a periodic variation at higher frequencies and then follow them using the VLBI techniques.

The analysis of our sample is still in progress. Our next goal is to classify these sources on the basis of their source structure such as extended jet sources, short jet sources, compact symmetric objects, or point source. This will help us further

investigate their morphology and understand their dynamics.

For the sources which have extended structures or CSO candidates, we plan on model-fitting them. This will be used to obtain their core-shift measurement. Core-shift values at two frequencies can be used to obtain the magnetic field near the core. Obtaining absolute position is not possible since we do not know where the central core lies. Hence, another component/source is required to obtain a relative position of the core. We note that it is important that the other component does not show core-shift effect along the same axis to avoid any confusion.

–

Chapter 4

Scattering study of Pulsars below 100 MHz using LWA1

The contents of this chapter were originally published as part of Bansal et al. 2019, The Astrophysical Journal, 875 (2), 146

Abstract: Interstellar scattering causes pulsar profiles to grow asymmetrically, thus affecting the pulsar timing residuals, and is strongest at lower frequencies. Different Interstellar medium models predict different frequency (ν) and dispersion measure (DM) dependencies for the scattering time-scale τ_{sc} . For Gaussian inhomogeneity the expected scaling relation is $\tau_{sc} \propto \nu^{-4} DM^2$, while for a Kolmogorov distribution of irregularities, the expected relation is $\tau_{sc} \propto \nu^{-4.4} DM^{2.2}$. Previous scattering studies show a wide range of scattering index across all ranges of DM. A scattering index below 4 is believed to be either due to limitations of the underlying assumptions of the thin screen model or an anisotropic scattering mechanism. We present a study of scattering for seven nearby pulsars ($DM < 50 \text{ pc cm}^{-3}$) observed at low frequencies (10 – 88 MHz), using the first station of the Long Wavelength Array (LWA1). We examine the scattering spectral index and DM variation over a period of about three years. The results yield insights into the small-scale structure of ISM as well as the applicability of the thin screen model for low DM pulsars.

4.1 Introduction

The interstellar medium (ISM) consists of an ionized and turbulent plasma which causes a delay in time and variations in the phase of radio signals. The subsequent interference gives rise to a diffraction pattern and broadens the apparent size of a source. Some observable ISM effects are dispersion, scattering, angular broadening, and interstellar scintillation. The dispersion causes a delay between the pulse arrival times of the upper and lower ends of a broadband pulsar signal. The scattering of a pulse signal causes temporal broadening, making average profiles grow asymmetrically broader at lower frequencies (e.g. Lewandowski et al., 2013, 2015, Löhmer et al., 2001, 2004). Pulsars are compact sources and emit short periodic pulses making them good sources for studying and understanding these propagation effects.

Assuming that the scattering occurs due to a thin screen between the observer and the source, the pulse broadening function can be expressed in terms of an exponential function $\sim \exp(-t/\tau_{sc})$ with scattering parameter τ_{sc} (Scheuer, 1968). This is also known as the thin-screen model where different ISM models of electron density fluctuations predict different frequency dependencies for the scattering parameter given by $\tau_{sc} \propto \nu^{-\alpha}$, where α is the scattering time spectral index. This model considers an isotropic homogeneous turbulent medium. For Gaussian inhomogeneity (Cronyn 1970; Lang 1971), the scaling relation is:

$$\tau_{sc} \propto \nu^{-4} DM^2, \quad (4.1)$$

while for a purely Kolmogorov distribution of inhomogeneities (Romani et al., 1986), the expected relation is:

$$\tau_{sc} \propto \nu^{-4.4} DM^{2.2}. \quad (4.2)$$

In both Equation 1 and 2, ν and DM are frequency and dispersion measure, respectively. The DM is given by $\int n_e dl$, where n_e is the electron density and dl is the path

length along the line of sight (LOS). Measurements of DM have helped us understand the distribution of free electrons and estimate pulsar distances in our Galaxy (Cordes and Lazio, 2002, Yao).

The amount of observed scattering can be estimated by assuming a spectrum of electron density fluctuations. A simple power-law model is given by:

$$P_{ne}(q) = C_{ne}^2 q^{-\beta}, \quad (4.3)$$

where q is the amplitude of a three dimensional wavenumber and C_{ne}^2 is the fluctuation strength along a given LOS. The above simplification is valid when the inverse of wave-number q ($1/q$) is much larger than the inner scale, and much lower than the outer scale Lambert and Rickett (1999). The value of β ranges between 2 and 4 and is related to the scattering spectral index via:

$$\alpha = \frac{2\beta}{(\beta - 2)}. \quad (4.4)$$

This simplified version of the scattering strength (Equation 4.3) may not be valid for real cases which are difficult to predict since we do not have information about the inner/outer scales. When the diffractive scale drops below the inner scale, the dependence becomes quadratic. This change in diffractive scale with observing frequency leads to flatter spectra in comparison to the theoretical value at lower frequencies (see Lewandowski et al., 2015, Rickett et al., 2009).

In previous scattering studies, while the average value of α seems to agree with the theoretical models, for individual pulsars large deviations have been detected across all ranges of DM (Lewandowski et al., 2015). For large DMs ($> 300 \text{ pc cm}^{-3}$), Löhmer et al. (2001) report a mean value for α of 3.400 ± 0.013 obtained from frequencies between 600 MHz and 2.7 GHz. The authors explain that this could be due to the presence of multiple screens between the pulsar and the observer. Lewandowski et al. (2013, 2015) report α in the range of 2.61 – 5.61, obtained for a sample of 60

pulsars. They also see α values below 2.61 but discarded them due to poor data quality. Geyer and Karastergiou (2016) simulated anisotropically scattered data and fit it with the isotropic model which results in α values less than the theoretically predicted values as well as the effect of non-circular scattering screens leading to low α values (~ 2.9). Scattering spectra with $\alpha < 4$ have been interpreted as a limitation of assumptions underlying the thin scattering model. Plausible deviations from the thin screen assumptions include a truncated scattering screen (Cordes and Lazio, 2001), the impact of an inner cut-off scale (Rickett et al., 2009), and anisotropic scattering mechanisms (Stinebring et al., 2001).

Moreover, ISM scattering accounts for one of the largest time-varying sources of noise in timing residuals of pulsars, which are used by pulsar timing arrays (PTAs) to detect gravitational waves from supermassive binary black holes (for more details see Arzoumanian et al., 2018, Ferdman et al., 2010, Shannon et al., 2015). Despite pulsars exhibiting steep spectra which imply higher flux at lower frequencies (Sieber, 1973), a large population of pulsars at lower frequencies are marginalized from the PTA analysis, where dispersion and scattering effects are greatest. These reasons further motivate us to undertake a study of propagation effects with pulsars at low frequencies. In this paper we focus on the scattering effects for a sample of pulsars observed at low frequencies (10 – 88 MHz), using the first station of the Long Wavelength Array (LWA1). We examine the scaling relations for scattering with time and frequency. We model for both the frequency dependence of the scattering time as well as the DM since α depends on both.

This paper has been organized in the following manner. In Section 2 we describe our observations and preliminary data reduction; in Section 3, we describe the scattering analysis methods. In Section 4, we describe our results for our sample of seven pulsars and Section 5 contains a detailed discussion and comparison with previous observations.

4.2 Observations

The LWA1 (Taylor et al., 2012) is a radio telescope array located near the Karl G. Jansky Very Large Array in central New Mexico. It consists of 256 dual-polarized dipole antennas operating in the frequency range 10 – 88 MHz. The outputs of the dipoles can be formed into four fully independent dual-polarization beams such that each beam has two independent frequency tunings (chosen from the range 10 – 88 MHz) with a bandwidth of up to 19.6 MHz in each tuning. The ability of the LWA1 to observe multiple frequencies simultaneously provides a powerful tool for studying frequency dependence of pulsar profiles (Ellingson et al., 2013). At these low frequencies, the pulses experience scattering and dispersion effects to a much greater extent than at higher frequency. Thus, the LWA1 can be used to make very precise measurements of these effects for studying the ISM properties.

The LWA Pulsar Data Archive¹ (Stovall et al., 2015) contains reduced data products for over 100 pulsars (Stovall et al., in prep) observed since 2011. The data products used for this study are produced by coherently de-dispersing and folding the raw LWA data using DSPSR². We used archival observations at four frequency bands: 35.1, 49.8, 64.5, and 79.2 MHz. The archival data have already been corrected for DM effects via coherent de-dispersion, and consist of 4096 phase bins for each of 512 spectral channels. The data are saved in the form of 30-second sub-integrations.

We excise RFI using a median zapping algorithm that removes data points with intensity more than six times compared to the median within a range of frequency channels. These files are then further reduced in two ways, one is to obtain total average profiles with two to four channels (depending on the signal to noise ratio of a pulsar) for scattering studies and the other with eight channels for obtaining the pulse time of arrivals (TOAs) for measuring the DM variation over time. For scattering study, we reduce the number of phase bins to 256 to smooth the average profiles. These tasks are performed using the PSRCHIVE command `pam` (van Straten et al.,

¹<https://lda10g.alliance.unm.edu/PulsarArchive/>

²<http://dspsr.sourceforge.net/index.shtml>

2012). We also remove the baseline from the observed profiles and then normalize them by their peak amplitude.

Table 4.1: Selected Pulsars Observed with LWA1

Source	DM_{LWA1} (pc cm^{-3})	Period (s)	Distance (kpc)	PM_{RA} (mas/yr)	PM_{Dec} (mas/yr)
B0329+54	26.7639(1)	0.71452	1.00	17.0(0.3)	-9.5(0.4)
B0823+26	19.4789(2)	0.5307	0.32	61.0(3)	-90.0(3)
B0919+06	27.2986(5)	0.4306	1.10	18.8(.9)	86.4(0.7)
B1822-09	19.3833(9)	0.7690	0.30	-13(11)	-9(5)
B1839+56	26.774(1)	1.6529	2.19	-30(4)	-21(2)
B1842+14	41.498(1)	0.3755	1.68	-9(1)	45(1)
B2217+47	43.488607(5)	0.5385	2.39	-12(8)	-30(6)

Notes: The list of sources studied in this paper. DM and Period values have been obtained from [Stovall et al. \(2015\)](#). Values for the Distance, PM_{RA} and PM_{Dec} have been obtained from ATNF³ pulsar catalogue.

In our preliminary study of scattering, we obtain archival data for seven pulsars (Table 4.1) for all the available epochs since the commission of LWA1. For each pulsar, we split each frequency band into two channels except for two pulsars: PSR B1822-09 and PSR B1839+56. For PSR B1822-09 we have used four channels to compare our results with previous studies by [Krishnakumar et al. \(2015\)](#). In case of PSR B1839+56, we have reduced the data to four channels to improve our sample size as the S/N at higher frequency bands (64.5 and 79.2 MHz) is poor. The analyzed frequency range was cut for all the pulsars with regard to full LWA capabilities due to S/N issues coming from the shape of pulsar spectra and/or sensitivity. We list center frequencies used for each pulsar in Table 4.2.

These seven pulsars were previously noted to have profile shapes below 100 MHz that are consistent with the effects of interstellar scattering ([Stovall et al., 2015](#)) and we follow the same data reduction procedure for all of them (see Section 4.3).

³<http://www.atnf.csiro.au/people/pulsar/psrcat/> .

4.3 Analysis

After obtaining the average profiles for each pulsar, we follow the same technique as reported in Krishnakumar et al. (2015, hereafter, KK15) to model scattering on this dataset. This formulation is based on the simple thin screen model (Williamson, 1972). The observed pulse profile can be expressed as a convolution of the frequency dependent intrinsic pulse $P_i(t, \nu)$ with the impulse response, characterizing the pulse scatter broadening in the ISM, $s(t)$ the dispersion smear across the narrow spectral channel $D(t)$, and the instrumental impulse response, $I(t)$. This results in $P(t) = P_i(t, \nu) * s(t) * D(t) * I(t)$, where $*$ denotes convolution. Following the same analysis as in KK15, we ignore the effect of $I(t)$ as our instrument is stable in time on the timescale of each observation. $D(t)$ can also be ignored as we use coherent dedispersion which corrects for dispersion smearing in the narrow spectral channel.

4.3.1 Intrinsic Pulse Model

The average pulse profile of a pulsar varies intrinsically with frequency in the number of components, their width, amplitude ratio, and separation between them. Hence, it is important to account for frequency dependent effects. Since the intrinsic pulse profile of a pulsar is unknown, we obtain an expected intrinsic profile model (IPM) at our frequency of interest using higher frequency average profiles for each source in Table 4.1. We assume the effects of scattering at higher frequencies are too small to affect the pulse shape. Average profiles at multiple frequencies enable us to obtain frequency dependent variation in the parameters affecting the pulse shape. For the IPM, we obtain average pulse profiles at frequencies ranging between $\sim 100 - 410$ MHz from the European Pulsar Network (EPN⁴). However, if one of the profiles in the above frequency range has poor signal to noise ratio (S/N) or two average profiles are close in frequency (143 and 151 MHz), it is difficult to accurately determine the frequency evolution. In such cases, we either consider no frequency evolution (see

⁴<http://www.epta.eu.org/epndb/>

Table 4.2) or include our 79.2 MHz data (highest central frequency in the LWA1 band) depending on its S/N. Differences in these average profiles apart from the intrinsic frequency effects of interest can also stem from different telescopes, instrumentation, observation date, and duration.

We model these profiles using a sum of Gaussians as explained in Kramer et al. (1994). The number of Gaussian components increases with each iteration and is limited to a maximum of five. We use various criteria to limit the number of Gaussian components, for example, the iteration stops when the amplitude of the residual maxima is $< 5\%$ of maximum peak intensity or the chi-square value increases with the addition of a new Gaussian component.

We assume that the number of components does not change within the selected range of frequencies (79.2 – 410 MHz). Once we obtain a set of Gaussian parameters for a profile at one of the frequencies (preferably LOFAR high band since it offers high S/N), we use these parameters as an initial condition and apply them to rest of the frequency profiles. We then fit for changes in the main component width based on a power law in frequency (for the list of parameters, see Table 4.2), as pulsars have broader pulse profiles at lower frequencies (Lyne, 2006). We also assume that spacing between the components and their relative amplitudes do not vary within our frequency selection. We consider the radius-to-frequency mapping only for the pulse width. Two pulsars (PSR B0329+54 & PSR B0919+06) in our sample have more than two components which makes determining the evolution of the component separation very complicated. In order to have consistent analysis we refrain from applying radius-to-frequency mapping for the remaining pulsars.

Table 4.2: IPM Frequency Parameters

Pulsar	Epochs (MJD)	Number of Components	Frequencies Used (MHz)	Frequency Dependence (a, b)
B0329+54	57144 – 58254	4	40.0, 44.9, 54.7 59.6, 69.4, 74.3	0.00655, -0.0811
B0823+26	57219 – 57899	2	44.9, 54.7, 59.6 69.4, 74.3	...
B0919+06	57312 – 58139	3	44.9, 54.6, 59.6 69.4, 74.3	...
B1822–09	57232 – 57919	1	47.3, 52.2, 57.2 62.0, 67.0, 71.8	0.0188, -0.166
B1839+56	57225 – 58209	1	27.8, 32.6, 37.6 42.4, 47.4, 52.2 57.2, 62.0	...
B1842+14	57242 – 58210	2	49.7, 59.6, 69.4 74.2, 84.1	0.461, -0.917
B2217+47	57242 – 58085	1	44.9, 54.6, 59.6, 69.4, 74.3, 84.1	0.127, -0.602

Notes: This table lists the range of epochs that have been included in this study for each pulsar; the number of Gaussian components; list of frequencies used for each pulsar, and frequency modeling parameters for the main component width to obtain the IPM given by $a \times \nu^b$ (discussed in Section 4.3.1).

4.3.2 Pulse Broadening

From the high-frequency models described above, we derive the frequency dependence and a new IPM is obtained for all the LWA1 center frequencies separately. The IPM is convolved with an exponential function with a scattering time (τ_{sc}) to obtain a template. This new template is a function of relative flux, phase offset, and scattering timescale. We then use a least square fitting algorithm to fit the template to the observed pulse profiles. This fitting uses the standard deviation of observed pulse profile as the uncertainty and estimates error bars on the fitting parameters. We

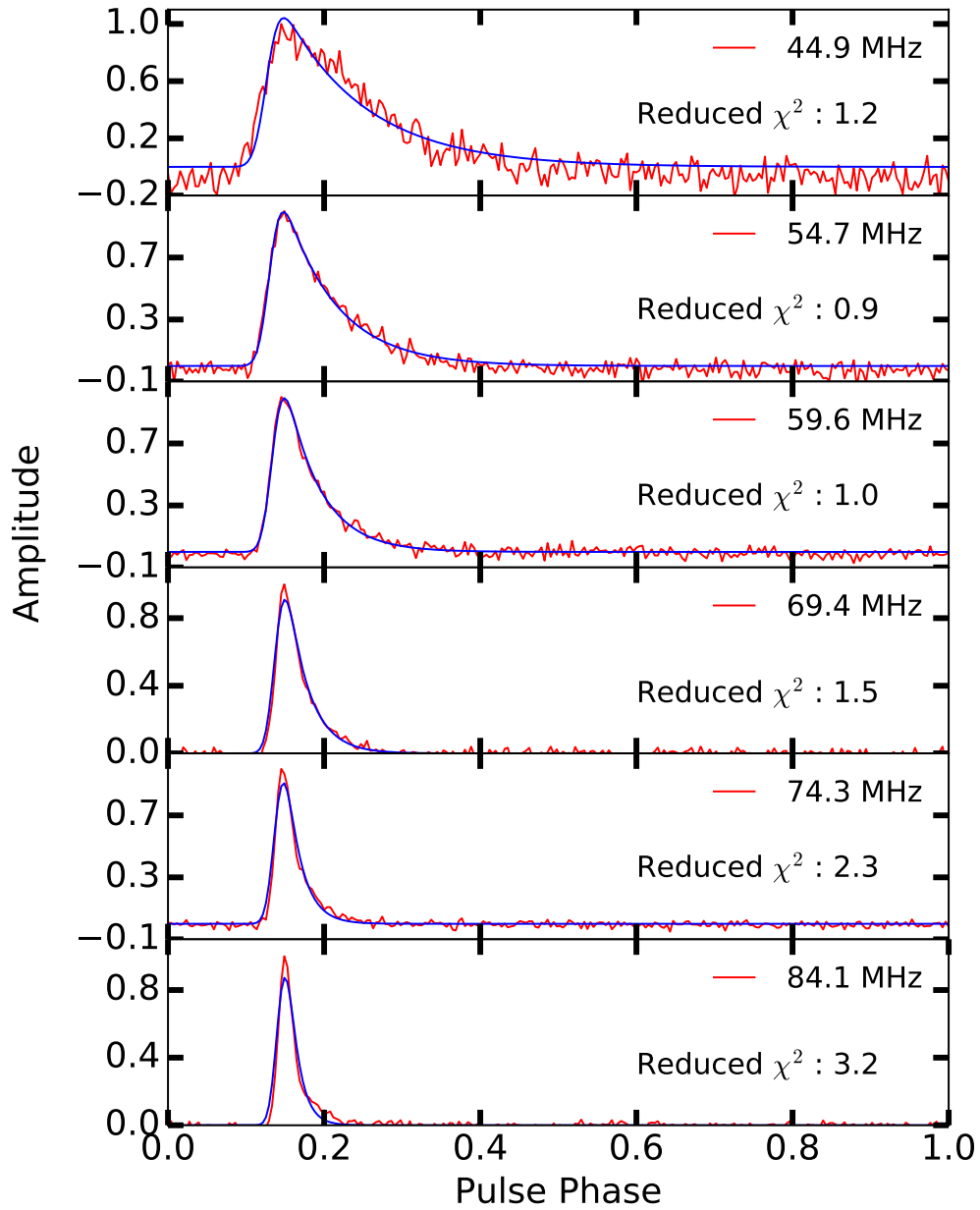


Figure 4.1: Fitting example for B2217+47 epoch MJD 57372. Top to bottom plots show fitting of intrinsic pulse models convolved with an exponential scattering function to the observed data. For B2217+47, the noise in the data increases as we go towards the lower frequencies.

assume that error on the template is negligible compared to the uncertainty in the data and will not affect the fitting parameters.

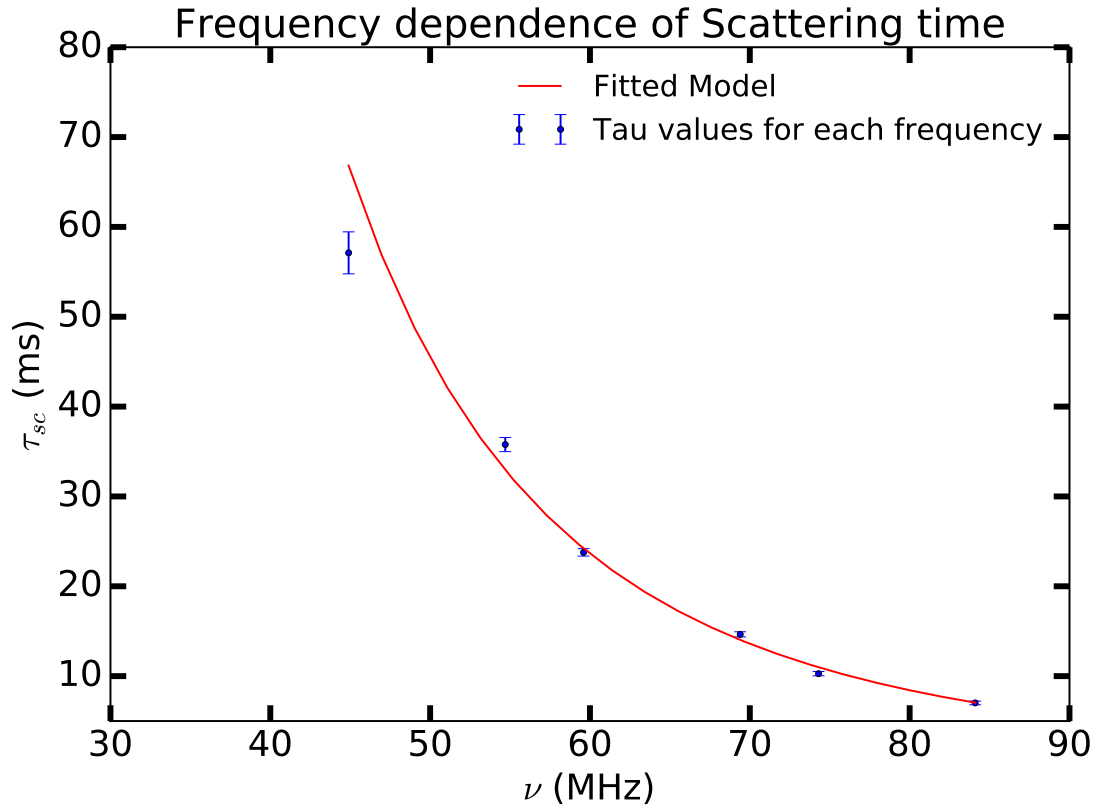


Figure 4.2: Example of α fit for PSR B2217+47 at epoch MJD 57372.

To align the pulse phase of the template and data, we use a low pass filtering technique to smooth the data. To do this, we first calculate the Fourier transform of the average profile. Then we filter out all the frequencies $> 30\%$ of the maximum frequency (f_{\max}) and rescale the intensities for frequencies between $20 - 30\%$ of f_{\max} by $(N - n_i)/N$ where n_i is the index of the frequency point and N is the total number of points within the specified frequency range. Intensities at frequency $< 10\%$ of the f_{\max} are scaled by 1. We include these two frequency ranges to avoid sharp edges. We then take the inverse Fourier transform of the filtered profile and use that to find the peak location. Since this filters out all the high Fourier frequencies, noise interferes less with determining the phase of the peak.

We plot the fitting examples for PSR B2217+47 at all six frequencies in Fig. 4.1 to demonstrate our procedure. As can be seen, our templates (Fig. 4.1) fit the observed dataset with a reduced chi-square in the range of $1 - 3$ for all frequencies. Subsequently,

we use τ_{sc} obtained from Fig. 4.1 to obtain an α value for PSR B2217+47 (Fig. 4.2). Similarly, we have obtained an IPM for all the pulsars in our sample and used them to fit our observations.

4.3.3 DM Variation

Since the scattering time can be related to DM (see Equation 4.1 and 4.2) along the LOS, it is important to study if there are any variations in DM over the duration of our observations. For our study, we measure δ DM using the pulsar timing software TEMPO⁵ DMX parameters. These measure an offset of DM from a fiducial value for multiple epochs each having a specified time span. We used a time span of about three years.

For the DM analysis, the number of frequency channels in the archive files is reduced to eight for each epoch at two frequencies, 64.5 and 79.2 MHz, using the PSRCHIVE task `pam`. We only use the higher frequencies since they have a better S/N. The TOAs for these profiles are obtained using `pat` (a PSRCHIVE algorithm). For the timing model, we first apply ephemeris changes using the task `pam` to make sure that all of the epochs have the same ephemeris, and then average profiles across all the epochs for each frequency using `psradd`, followed by smoothing the profile using `psrsmooth`. We then align the 64.5 MHz and 79.2 MHz pulse models, before obtaining the TOAs. We have converted the TOAs to the solar system barycentre using the DE405 model (Standish, 1998). The time difference between the observed TOA and the timing model gives timing residuals for each observation. We combine these timing residuals from both the frequencies into one file and fit for the above-listed parameters.

⁵<http://tempo.sourceforge.net/>

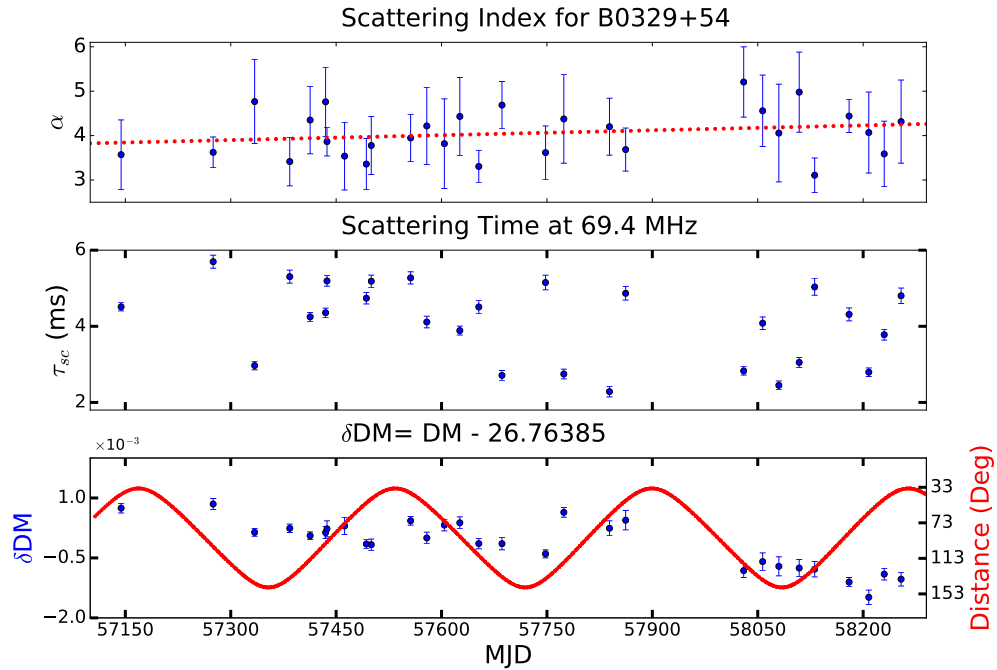


Figure 4.3: The top and middle panel consist of scattering index values (α) and scattering time at 69.4 MHz, respectively, over time for PSR B0329+54. The bottom panel consists of δDM values (blue) and solar elongation angle (red) over time. All four measurements have been made at the same epochs for a span of about three years. For more details see Section 3.

4.4 Results

We have studied scattering in seven pulsars using the LWA1 data. Below we discuss our results for each pulsar individually.

4.4.1 PSR B0329+54

PSR B0329+54 is known to have 9 emission components, one of the highest number of components for any pulsar (Gangadhara and Gupta, 2001). We have used four components where the amplitude of these components is above 5% of the main component amplitude. The frequency evolution for the main component has been obtained from three frequencies: 79.2, 143, and 408 MHz (obtained from EPN).

We have plotted α , τ_{sc} , δDM , and the solar elongation angle in Fig. 4.3. The measured median α value is 4.05 ± 0.14 . This estimate is in agreement with the prediction of the Gaussian distribution where the α value is expected to be 4.0. The fitting to the α value over time yields a slope equal to $0.13 \pm 0.11 \text{ year}^{-1}$. This is consistent with there being little or no variation in the scattering index with time.

PSR B0329+54 has been found to have periodic variation in its timing residuals with two different periods likely due to the presence of potential planets (Starovoi and Rodin, 2017) in its orbit. This contributes to the timing noise, hence, we have obtained the DM values for this pulsar in a slightly different manner. Instead of fitting for δDM across all epochs simultaneously, we have fit for each epoch individually. Fig. 4.3(b) shows the variation in δDM values with an overall change of about $0.0015 \text{ pc cm}^{-3}$ over a span of about 3 years. These variations do not correlate with the solar elongation angle (Fig. 4.3c) where the trend is periodic. We do not expect this pulsar to exhibit variation in DM due to the solar wind since the closest distance of approach is 34.2° . This pulsar is also known to exhibit mode switching (Chen et al., 2011), where the relative amplitude of the component changes and the total pulse width becomes narrower as the profile components change their phases. These mode changes are simultaneous across frequency but non-uniform (Bartel et al., 1982), hence, will introduce a frequency-dependent variation in timing residuals. Apart from mode change, it is also known to have planets in its orbit which will again affect the timing residuals. Hence, this apparent variation in δDM is not due to any physical change in ISM, but instead the high timing noise of this pulsar.

4.4.2 PSR B0823+26

PSR B0823+26 pulse profile consists of a main pulse, post-cursor, and an inter-pulse (Rankin and Rathnasree, 1995). The amplitude of both inter-pulse and post-cursor is less than 5% of the main pulse. However, we note there are two additional wing components on both sides of the main pulse that are above 5% of the main pulse's amplitude at 143 MHz and 151 MHz. It is difficult to obtain frequency dependency

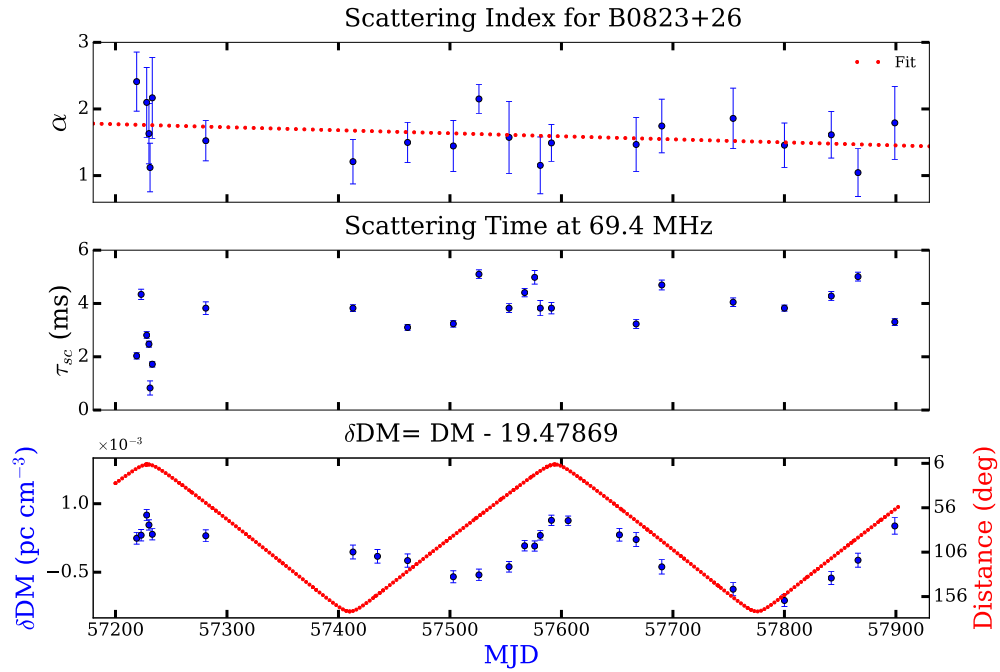


Figure 4.4: α , τ_{sc} at 69.4 MHz, δDM , and solar elongation angle for every epoch for PSR B0823+26

from only these two nearby frequencies especially when it involves multiple components. Hence, for the IPM, we have used the profile at 151 MHz and considered no frequency evolution.

This pulsar is known to exhibit nulling, detected in LOFAR observations (Sobey et al., 2015), which causes several observations without any pulse, hence, have been excluded from this analysis. We have plotted the α and DM values over time in Fig. 4.4 top and bottom plots, respectively. The estimated median α value for this pulsar is 1.55 ± 0.09 , which is quite small in comparison to the expected theoretical value. We fit a trend to the α values over time and have found the slope value to be $-0.16 \pm 0.13 \text{ year}^{-1}$. This is consistent with there being little or no variation in the scattering index over time.

From the δDM plot (Fig. 4.4b), we see a periodic variation of $\sim 1.7 \times 10^{-3} \text{ pc cm}^{-3}$ over a period of about half a year. This periodicity in DM can be attributed to

the solar wind, due to its close proximity to the Sun (Fig. 4.4c). The closest distance of approach for this pulsar is about 7° .

4.4.3 B0919+06

The number of components in B0919+06 is a matter of some debate since this pulsar is known to exhibit abnormal emission which causes flares a few degrees in phase before the normal emission (Han et al., 2016, Rankin et al., 2006). The timescale of this emission is about 15 seconds and expected to occur once in 1000 pulses. Since for our analysis we average an hour long archival observation in time, we do not detect it. The Gaussian fitting of the 135 MHz profile yields three components and the 408 MHz profile shows only two components, where the post-cursor component is missing. Due to this we only derive the IPM from 135 MHz with no frequency evolution. Since 135 MHz is closer to the frequencies we are working with as compared to 408 MHz which is six times larger. This provides us best possible fits for this pulsar.

The average α value is 2.88 ± 0.18 . The slope value is $-0.28 \pm 0.15 \text{ year}^{-1}$. The epochs ranging from MJD 57744 to 57903, either have poor data quality or fewer number of frequencies, hence, have not been included in the fitting plot. For B0919+06, the scattering time ($\sim 5 \text{ ms}$) is small in comparison to PSR B2217+47 and B0329+49 ($\sim 30 \text{ ms}$) at the frequencies of LWA1. This could imply that pulsars with similar DM values (PSR B0329+54) have different scattering timescales, as it also depends on the location of a source in the galaxy.

This pulsar appears to have a steep spectrum at the LWA frequencies and, consequently, the S/N deteriorates when we go towards the higher end of the spectrum. Hence, we ignore the last channel (84.1 MHz) for scattering index estimation. For some of the epochs, the average profile fits poorly with the model for the mid-range frequencies and we get a lower scatter timescale for a higher frequency. It seems that this may be attributed to the error in τ_{sc} and these error bars may be underestimated.

The δDM plot (Fig. 4.5c) exhibits variation over time with no overall change in

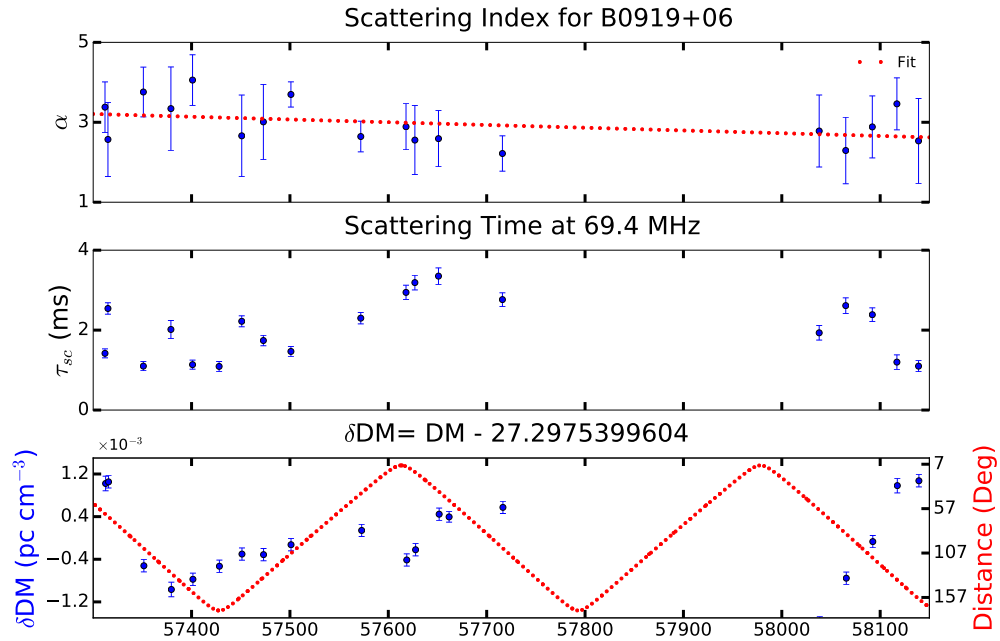


Figure 4.5: α , τ_{sc} at 69.4 MHz, δDM , and solar elongation angle for every epoch for B0919+06

δDM value. The minimum solar elongation angle for this pulsar is 8.36° . Thus, we expect the variation in δDM due to the solar winds (Fig. 4.5c) to be periodic which does not align with our δDM observations. This pulsar is known to show variation in the frequency derivative (Perera et al., 2014). The observed trend in δDM can, therefore, be explained as a combined effect of both the solar wind and the varying frequency derivative.

4.4.4 PSR B1822–09

PSR B1822–09 is a single component pulsar. We have obtained frequency evolution from these four frequencies: 87, 149, 400, and 408 MHz. For this pulsar, we have reduced the data to four channels instead of 2 to compare our results with Krishnakumar et al. (2017) (hereafter, KK17 and see Section 5.1), as they also reduced it to four channels for their analysis. We have plotted α , δDM , and relative solar

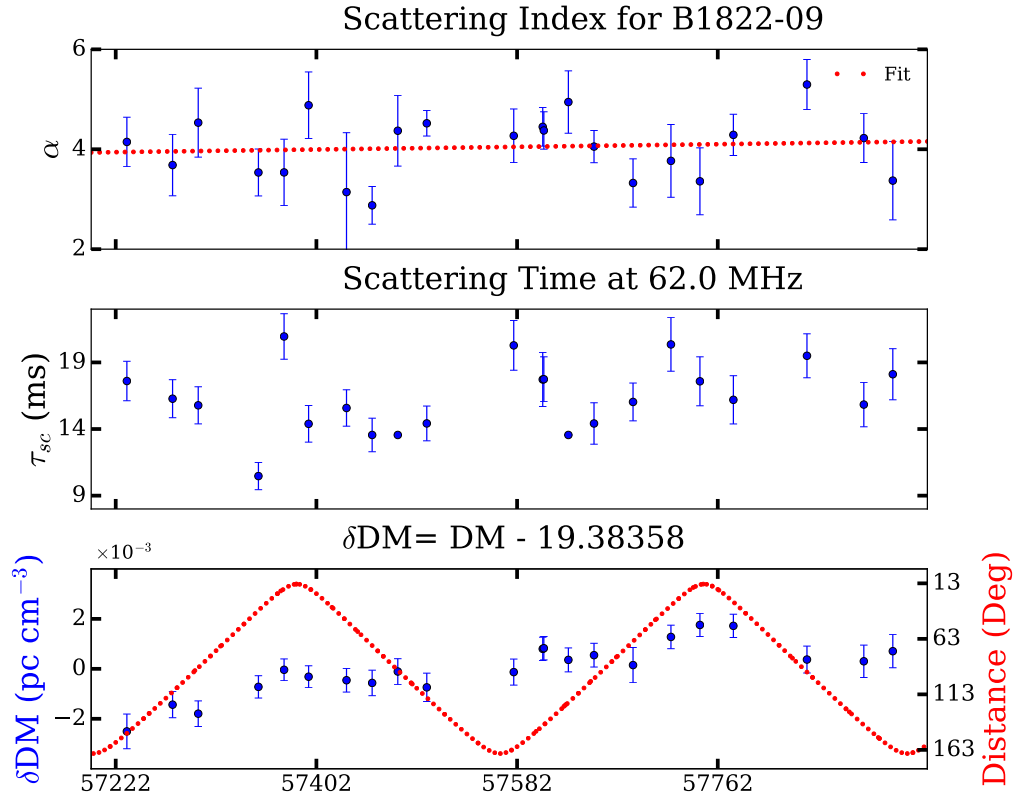


Figure 4.6: α , τ_{sc} at 62.0 MHz, δDM , and solar elongation angle for every epoch for PSR B1822–09

distance over the observation time in Fig. 4.6. The median α value is 4.18 ± 0.13 . This value falls in the range of both the Kolmogorov and Gaussian models. The scattering index remains constant over the duration of our observations with a slope equal to $0.11 \pm 0.25 \text{ year}^{-1}$.

PSR B1822–09 is a nearby pulsar with a DM of 19.38 pc cm^{-3} (Table 4.1). Its minimum solar elongation angle is about 13 degrees. As can be seen in the Fig. 4.6c, there is an overall increment in δDM value of $4.8 \times 10^{-3} \text{ pc cm}^{-3}$ over a span of about three years. Additionally, there are smooth rises and dips with a magnitude of 2.4×10^{-3} over a span of 167 days, which are due to change in the solar separation angle. The transverse speed of 22 km s^{-1} , implying that LOS of this pulsar remains

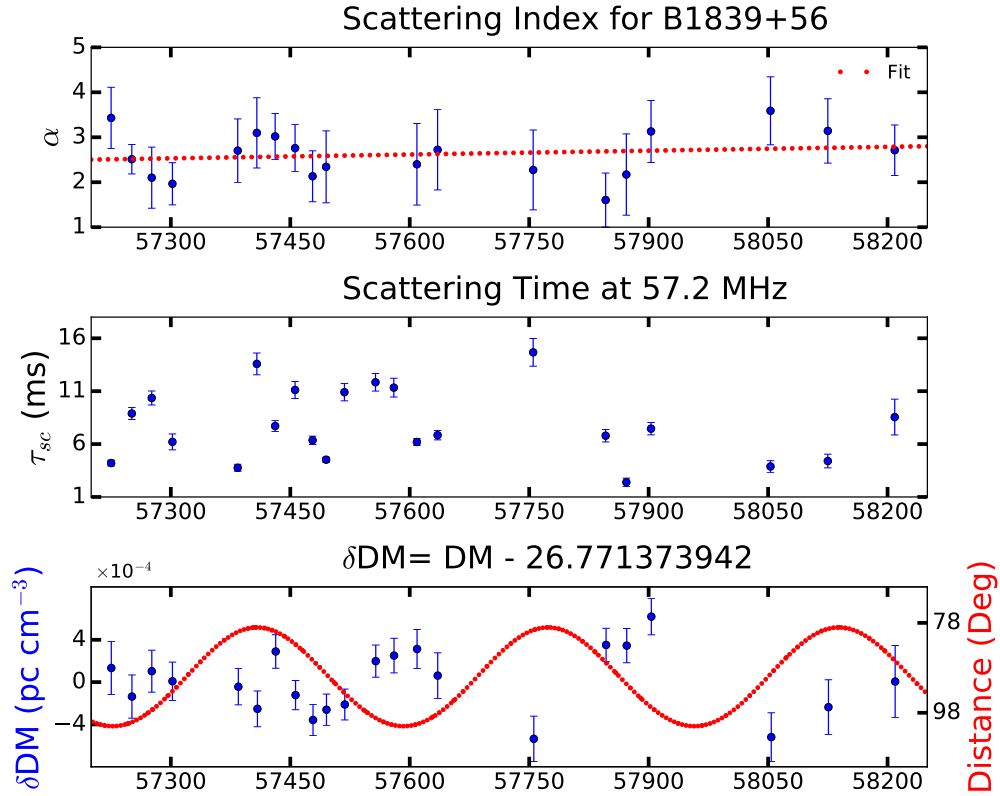


Figure 4.7: α , τ_{sc} at 57.2 MHz, δDM , and solar elongation angle for every epoch for B1839+56

the same. The overall increase in δDM implies turbulence in the ISM along the LOS. Since the LOS remains the same, the scattering index remains constant

4.4.5 B1839+56

PSR B1839+56 is another single component pulsar. We have derived the IPM using 143 MHz profile. Due to poor S/N at 79.2 MHz, we were unable to obtain frequency evolution for this pulsar. We have plotted the α , δDM values, and relative solar distance for this pulsar in Fig. 4.7. The median value of α is 2.70 ± 0.16 . The α remain mostly constant with an estimated slope of $0.10 \pm 0.05 \text{ year}^{-1}$.

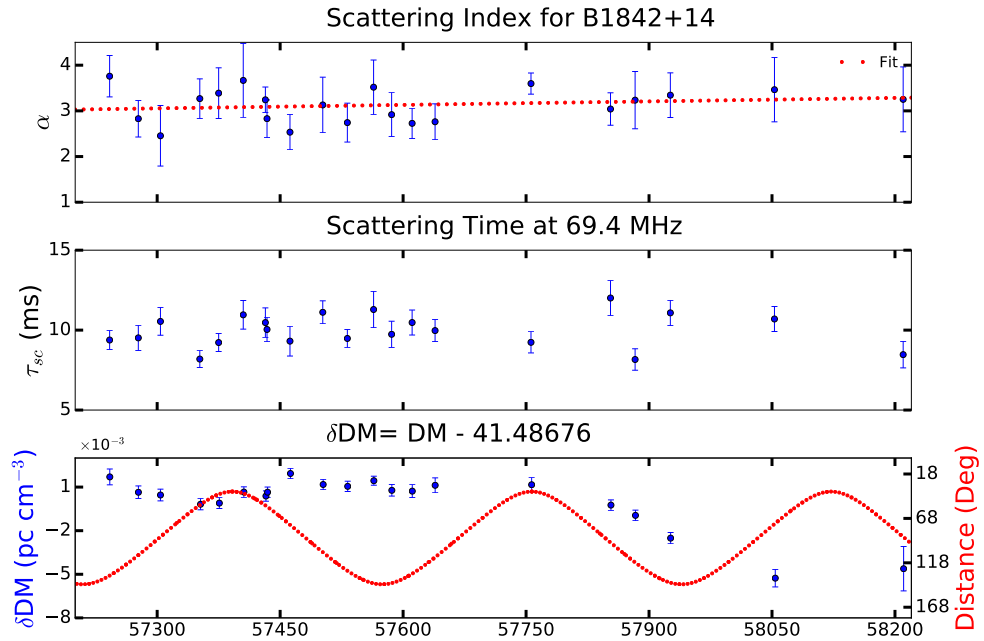


Figure 4.8: α , τ_{sc} at 69.4 MHz, δDM , and solar elongation angle for every epoch for B1842+14

The δDM values for B1839+56 are small compared (of the order of $10^{-4} \text{ pc cm}^{-3}$) to the other pulsars (of the order of $10^{-3} \text{ pc cm}^{-3}$) discussed in this paper. Also, these error bars are comparable to the variation in δDM , thus, implying insignificant variation in DM over time.

4.4.6 B1842+14

This is a double component pulsar at LWA frequencies. The IPM has been obtained using the LOFAR data at 143 MHz and the LWA profile at 79.2 MHz. We only use frequency evolution of the main component as discussed in Section 3.1. We have plotted α , τ_{sc} at 69.4 MHz, δDM , and relative solar distance in Fig. 4.8. The median α value is 3.24 ± 0.11 . The α remains constant over the duration of our observations with a fitted slope value equal to $0.09 \pm 0.12 \text{ year}^{-1}$.

From the δDM plot (Fig. 4.8c), we see a moderately constant δDM until epoch MJD 57756 and a linear change of $5.8 \times 10^{-3} \text{ pc cm}^{-3}$ over 455 days. This does not correlate with the solar elongation angle and the closest angular distance of this pulsar to the Sun is about 37° , which is too far away to affect the DM significantly. The transverse velocity of this pulsar is about 365 km s^{-1} (Table 4.1), which would affect the LOS, hence, the δDM . We note that this change in LOS does not affect scattering index.

4.4.7 B2217+47

PSR B2217+47 is typically known to have a single component below 300 MHz (Kuzmin et al., 1998), however, recently it was found to have an additional component (Pilia et al., 2016). This component changes its relative position to the main component over time (Michilli et al., 2018). Since we do not have all the frequency data for the same epoch, we choose to ignore this component and only use the main component for IPM. We obtain the frequency evolution of the pulse component using 79.2, 143, and 151 MHz. This pulsar also has the highest S/N in our sample (Stovall et al., 2015).

For PSR B2217+47, we have plotted α values for all epochs to see if there is any variation over time (Fig. 4.9a). The median α is 3.58 ± 0.10 . The green dotted line represents the linear fit with an estimated slope of $-0.44 \pm 0.10 \text{ year}^{-1}$, which implies a decrement in α at a level of 4.4σ .

Fig. 4.9c shows a variation in δDM values over time. The overall variation in δDM is about 0.005 pc cm^{-3} over a span of 661 days. To understand the variation in DM, we plot the solar elongation of this pulsar during our observation period (Fig. 4.9c), which changes periodically, different from both α and δDM trends. The closest angular distance of PSR B2217+47 from the Sun is about 50° which does not affect the pulsar DM significantly. Since both scattering index and δDM values vary with time, we test if they are correlated using Spearman rank-order correlation. We estimate the correlation index between the α and δDM values equal to -0.56

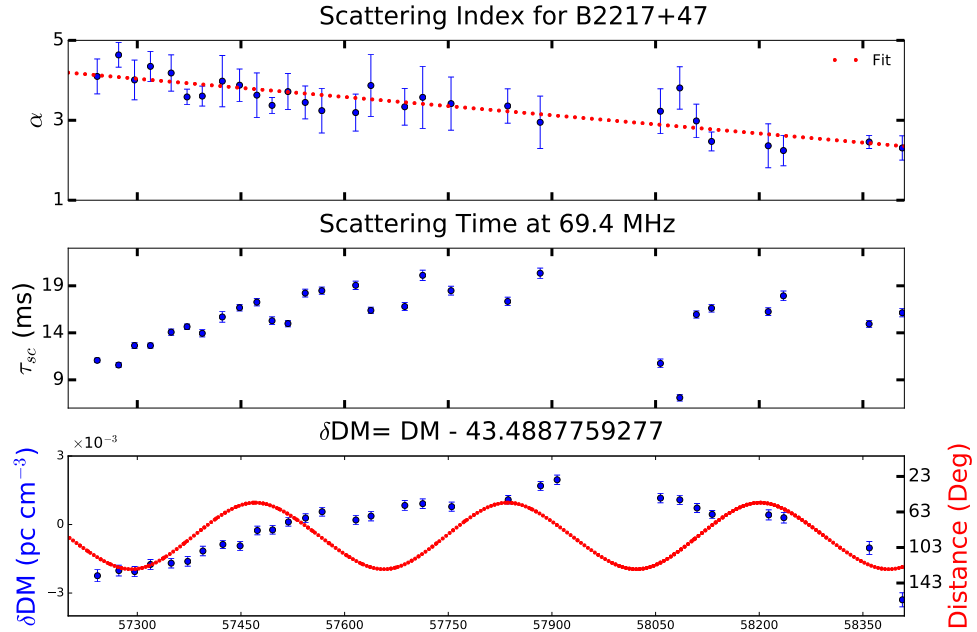


Figure 4.9: α, τ_{sc} at 69.4 MHz, δDM , and solar elongation angle for every epoch for B2217+47. We include scattering time to show its correlation with δDM (see section 4.7).

(P-value = 0.003), implying a negative correlation between them. We also estimate the correlation index between δDM values and scattering timescales at multiple frequencies. For the higher frequency bands, there is a positive correlation with the similar magnitude as α , thus confirming our expectation that variation in DM affects the scattering timescale (see Equation 4.1 and 4.2).

4.5 Discussion & Conclusion

We will now summarize our results and discuss what information is gained from time evolution of scattering parameters. We will also discuss how our results align with the thin screen model and the underlying assumptions.

4.5.1 Scattering Spectral Index Distribution

Assuming that the scattering time follows a power law (see Equations 4.1 and 4.2), we performed a weighted least-squares fit to estimate the spectral indices for the pulsars in our sample. Our results show that α values except for two pulsars in our sample show deviations from the theoretical power law. Scattering spectral index allows us for an estimate of electron density index (β ; see Equation 4.4). Table 4.3 summarizes the scattering spectral index median value and β for our sample of pulsars. Since Equation 4.4 is only applicable for $\alpha > 4$, we have been able to obtain this only for PSR B0329+54 and PSR B1822–09 (see Xu and Zhang, 2017 for more details).

The α measurements for PSR B0329+54 and PSR B1822–09 are consistent with the theoretical value of 4.4 for a Kolmogorov distribution. Our median α value for these pulsars slightly differs from α values of 4.3 ± 0.1 and 5.0 ± 0.5 , respectively, as reported in KK17. The reason for this discrepancy is likely a result of a different IPM. They have used the 87 MHz profile with no frequency evolution for the IPM whereas we have used a higher frequency (151 MHz) with frequency evolution (refer Section 4.3 and 4.4). We also note that assuming no frequency evolution overestimates the τ_{sc} and hence, the value for α .

PSR B0823+26 has the lowest value of α , 1.55 ± 0.40 among all the pulsars. We compare this observation with scattering measurement done by Kuzmin and Losovsky (2007) where they report the α value for this pulsar is 3.68 (no error bar reported). This is quite different from our observation, however, their value was obtained using only two frequencies, which makes it less reliable. Another way of obtaining scattering spectral index is by using spectral dependence of the decorrelation bandwidth, as done by Daszuta et al. (2013) for PSR B0823+26. The decorrelation bandwidth is related to the scattering time by $2\pi\tau_{sc}\delta\nu_d = C_1$, where ν_d is the decorrelation bandwidth. They have found this value to be 3.94 ± 0.36 , which also differs significantly from our observation. However, this decorrelation bandwidth measurement is at higher frequencies (> 300 MHz) which raises a question of if the scattering index varies with frequency.

Other pulsars with a large α deviation from theoretical expectations are B1839+56 and B0919+06 with estimated median values of 2.70 ± 0.16 and 2.88 ± 0.18 , respectively. We compare our α measurement for B0919+06 with Kuzmin and Losovsky (2007), where they have reported a value of 3.05 ± 0.08 . This agrees with our measurement within the error bars, and compared to PSR B0823+26 is likely to be more reliable since it was obtained using three frequencies.

PSR B2217+47 has a median α value of 3.58 ± 0.10 . This is lower than the theoretical value for a Gaussian distribution of 4, but closer to that theoretical expectation than α values for four pulsars in our sample. Similar to PSR B0329+54 and B1822−09, our α value for B2217+47 agrees with values reported in the literature (4.2 ± 0.1 , see KK17) but is slightly higher than our median due to a different IPM. For PSR B1839+56 and PSR B1842+14, this is the first time scattering spectral index has been estimated. In this study, we have considered no frequency evolution for three pulsars (for example PSR B0823+26, see Table 4.2) in our sample for which we suggest that the reported values should be on the higher end.

Table 4.3: Scattering Results

Pulsar	α	β
B0329+54	4.05 ± 0.14	3.95
B0823+26	1.55 ± 0.09	..
B0919+06	2.83 ± 0.18	..
B1822−09	4.18 ± 0.13	3.83
B1839+56	2.70 ± 0.16	..
B1842+14	3.24 ± 0.11	..
B2217+47	3.58 ± 0.10	..

Notes: α and β values are median values obtained in this study. α and β are scattering index and electron density index, respectively (refer Equation 4.3 and 4.4).

4.5.2 Deviation from theoretical models

PSR B0823+26 is the nearest source in our sample and shows large deviations in the scattering index from the thin screen model. There are three possible explanations for this observation. First, this pulsar shows intrinsic variation such as nulling,

sub-pulse drifting, and mode switching, which may affect the average profile and hence, the evaluation of scattering time. This pulsar also has a small scattering time in comparison to PSR B1822–09 even though both sources have the same DM. The second explanation for this observation is that since scattering time is small in comparison to the pulse width, it is difficult to obtain the true scattering time and hence, we get a flatter index. The third explanation is based on inner scale effects. Since at lower frequencies the diffraction scale can become smaller than the inner scale, which causes a flatter spectra as compared to the theoretical model. This explains the discrepancy in observed α value with that reported in [Daszuta et al. \(2013\)](#) since they had observed it at a higher frequency, implying steeper spectra.

As mentioned in the introduction, deviation from the theoretical models has been observed in many scattering observations across all ranges of DM, more often for high DM pulsars ([Lewandowski et al., 2013, 2015](#)). [KK17](#) claim that α estimates for DMs $< 50 \text{ pc cm}^{-3}$ are in good agreement with those expected for a Kolmogorov spectrum with an average value of 3.9 ± 0.5 . However, on an individual basis these sources show a deviation from the expected value.

There are various plausible explanations for these deviations. First of all, the thin screen model assumes an infinite thin screen. This assumption seems valid in the case of medium-range DMs. For large DMs, the probability of having multiple screens increases, hence, the assumption of the thin screen becomes less valid. In the literature, most of the scattering studies ([Lewandowski et al., 2013, 2015](#)) have been conducted for high DM pulsars ($\text{DM} > 300 \text{ pc cm}^{-3}$), where $\alpha < 4$ have been attributed to multiple finite scattering screens. For the low DM sources, the scattering screen can be finite which can lead to α values less than or equal to 4.0 ([Cordes and Lazio, 2001](#)). Spectra with $\alpha < 4$, are expected as a result of finite scattering screen by [Rickett et al. \(2009\)](#) and anisotropic scattering mechanisms by [Stinebring et al. \(2001\)](#).

In a recent simulation study, [Geyer and Karastergiou \(2016\)](#) find that for anisotropic scattering, spectral index of scattering time is < 4 with the infinite and finite screen. Anisotropy in scattering implies elongated scattering angle in one direction as com-

pared to other direction. However, the effect of anisotropy would be more distinctive in the case of image broadening as compared to temporal broadening. We note that in case of PSR B2217+47 where we see a change in scattering index with time, its velocity along Declination is only 2.5 times the RA which makes it difficult to interpret if the observed trend is due to change in anisotropy. We discuss this source further in more detail in Section 5.3. In order to conclusively determine the effect of anisotropy, in addition to measuring the temporal broadening, we either need to image the source simultaneously or study its dynamic spectrum. From this study, we suggest that low DM pulsars do not always follow Kolmogorov distribution or the Gaussian distribution. It is likely due to the deviation of the scattering model from the thin screen model even for the nearby pulsars.

Apart from DM, another important factor that will likely affect the scattering is the location of a pulsar in the Galaxy. Among the previous studies, Lewandowski, Kowalińska, and Kijak (2015) report no correlation between the scattering spectral index and the distance or the position of the source in our Galaxy. Similarly, KK17 do not suggest any trend in their data with respect to the location in our Galaxy and emphasize that to draw conclusions from such a plot, we need DM-independent distance measurements.

4.5.3 Time Evolution of Scattering parameters

The main focus of this paper is to study the evolution of α with time and to understand it in more detail we also obtain variation in DM in parallel for the same epochs. In our sample of seven pulsars, only B2217+47 shows a significantly varying α , whereas we see a variation in DM for all pulsars except PSR B1839+56. This variation in DM can be periodic, linear or a combination of both depending on the underlying effects. A linear trend in DM can be explained either due to the change in LOS due to the proper motion of a pulsar or a change in distance to the screen along the LOS (Lam et al., 2016, Petroff et al., 2013). Periodic variation in DM can be attributed to either ionosphere or the solar wind. We estimated the contribution of the ionosphere

to DM which is of the order of $< 10^{-4}$ pc cm $^{-3}$, about 10 times smaller than the DM variations we measured, hence would not affect our observations. We used an IONEX Global Ionosphere Model⁶ to model the slant total electron content in the ionosphere and converted that to a DM since they are the same measurement with different units. From our observations we note that solar wind will affect the DM for the slow pulsars with a minimum solar elongation of about 15° .

For PSR B0823+26, the δ DM plot shows periodic variation, which is mainly due to the change in solar elongation angle. Similarly, for B1822–09, we see smooth periodic rises and dips due to change in angular distance to the Sun, as well as an overall change of 0.001 pc cm $^{-3}$ per year in δ DM. This implies a slight variation in the column density along the LOS.

We note that we have derived these DM values from timing solutions which also depend on the intrinsic properties of a pulsar including the ISM. In such cases, the derived DM values may not represent the actual DM of the ISM. This is true for PSR B0329+54 and B0919+06 for which intrinsic variations in pulsar cause large timing residuals. The δ DM plot for PSR B0329+54 shows variation in δ DM, however, the actual variation is in the timing residuals due to the possibility of planets in its orbit (Starovoit and Rodin, 2017). The δ DM variation for B0919+06 also includes variation in pulsar frequency derivative. Since the trend in δ DM for both pulsars are due to intrinsic reasons, this requires further investigation and is beyond the scope of this paper. This, however, is beyond the scope of this analysis.

We expect a change in DM due to the change in LOS will also affect the scattering spectral index. This is the case of PSR B2217+47 which shows a decrement in α values with time. The α and δ DM are anti-correlated and the scattering time at higher frequencies is positively correlated with δ DM (Fig. 4.9). This pulsar is known to have an additional component, a trailing component in the main pulse (Michilli et al., 2018). However, we do not see this additional component at our frequencies. We see a similar change in DM as reported in Michilli et al. (2018) of 0.004pc cm $^{-3}$

⁶<ftp://cddis.gsfc.nasa.gov/gnss/products/ionex/>

over the same duration. This implies that this pulsar is encountering a gas cloud with a higher density and its structure is changing, which is affecting the pulse broadening.

We note that variations in DM may not affect the scattering spectral index if the motion is parallel to the LOS since the ISM structure would remain the same along the LOS (Lam et al., 2016). In the case of PSR B1842+14, there is a change in DM but no variation in the scattering index. This implies that this change is likely due to a change in electron density along the LOS and the structure of ISM remains the same.

4.6 Summary

We present a study of scattering spectral index and DM variation for seven pulsars over the timescale of ~ 3 years using the LWA1. This is the first time a systematic evolution of α has been reported according to our survey of the literature. Most of the pulsars in our sample exhibit constant α throughout the observations with the slope value consistent with zero. The exception to this is PSR B2217+47 where we measure a decrement in α over our observation period of three years which anti-correlates with a change in DM. For PSR B0823+26, we obtain the smallest α value of 1.55 ± 0.40 , indicating inner scale effects.

The median scattering spectral index for five of the seven studied pulsars is below 4, implying deviation from both Gaussian and Kolmogorov inhomogeneities for $DM < 50 \text{ pc cm}^{-3}$. α measurements at lower frequencies and their deviations from theoretical models have led to an improved understanding of correlations between ISM structure and pulsar scattering, but the detailed structure of the ISM and the physical interpretation still remain unclear. Anisotropy is another likely explanation for these deviations in scattering spectral index. However, to effectively understand the anisotropy in the ISM, we need to study the dynamic spectra parallel to the temporal broadening for a larger sample of pulsars. More observations of other pulsars at these low frequencies will be helpful in understanding the distribution of scattering

spectral index with DM. Similarly, DM-independent distance measurements will be helpful in obtaining the scattering index distribution across the Galaxy.

4.7 Acknowledgements

We would like to thank Joe Malins to help with the ionosphere DM estimations. We also thank the anonymous referee for valuable suggestions that has improved this paper. Construction of the LWA has been supported by the Office of Naval Research under Contract N00014-07-C-0147 and by the AFOSR. Support for operations and continuing development of the LWA1 is provided by the Air Force Research Laboratory and the National Science Foundation under grants AST-1835400 and AGS1708855.

Chapter 5

Detection of Echoes in PSR B1508+55 using the LWA1

Content of this chapter has been submitted to the Astrophysical Journal, and is currently under review.

Abstract: PSR B1508+55 is known to have a single component profile above 300 MHz. However, when we study it at frequencies below 100 MHz using the first station of the Long Wavelength Array, it shows multiple components. These include the main pulse, a precursor, and a trailing component. The separation of the trailing component from the main peak evolves over the course of a three year study. This evolution is likely an effect of the pulse signal getting refracted off an ionized gas cloud (acting as a lens) leading to what appears to be a trailing component in the profile as the pulsar signal traverses the interstellar medium. Using this interpretation, we identify the location and electron density of the lens affecting the pulse profile.

5.1 Introduction

Although individual pulses from pulsars are quite varied, pulsars typically have a stable integrated pulse profile over time-scales of years to decades (Helfand et al.,

1975, Liu et al., 2012). This is why they are also considered to be one of the best clocks in nature and are being incorporated for the search of gravitational waves by the pulsar timing arrays (EPTA¹, PPTA² and NanoGrav³). Despite this stability, numerous pulsars have been observed to manifest a continuous pulse profile evolution.

Pulse variations can be classified on the basis of the length of its timescale. Short scale variations such as nulling and mode change occur on timescales ranging from a few pulse periods to hours and days (Wang et al., 2007). Longer timescale variations such as intermittent pulsars where the spin down rate undergoes a quasi-periodic cycle between phases occur on the range of months to years (Lyne et al., 2017). This study concerns longer timescale variations and, therefore, only those will be discussed in the following. These variations can be due to various reasons such as variations in the pulsar magnetosphere (Hobbs et al., 2010). Some pulsars in binary systems have been observed to vary due to geodetic precession, free precession or propagation effects as the signal travels through the turbulent ionized interstellar medium (ISM, Keith et al., 2012). Recently, (Cordes and Shannon, 2008) mention a specific case when there is an asteroid in the pulsar orbit. This may affect the pulse profile either due to geodetic precession or if the debris of the asteroid interacts with the pulsar magnetosphere. Thus, studying pulse profile changes in radio pulsars can provide insights into the underlying physical mechanisms responsible for the observed changes and improve the precision of pulsar timing experiments.

To provide a few examples, PSR B1828–11, PSR J0738+4042, and recently, B2217+47 have all been found to show such profile variations. PSR B1828–11 shows quasi-periodic profile variation which has been interpreted to be due to free precession of the pulsar (Stairs et al., 2000). This interpretation, however, was later questioned by Lyne et al. (2010) when they found quasi-periodic profile changes in six pulsars (including PSR B1828–11), which are correlated with the spin-down rate, implying a relation to intrinsic processes of the pulsar. In the case of PSR J0738–4042, pulse

¹European Pulsar Timing Array (Stappers et al., 2006)

²Parkes Pulsar Timing Array (Manchester et al., 2013)

³North American Nanohertz Observatory for Gravitational Waves (McLaughlin, 2013)

variations were at first associated with a magnetospheric change (Karastergiou et al., 2011) and later due to an interaction between its magnetosphere and an asteroid (Brook et al., 2013). Recently, PSR B2217+47 has been found to show variations on the time scale of months to years in its pulse profile shape (Michilli et al., 2018). The authors list three plausible causes which include free spin of the pulsar, variations in pulsar emission due to perturbations in the plasma filling the magnetosphere, and structures in the ISM creating a transient component in the form of echoes, strongly favoring the last cause.

While studying scattering in pulsars below 100 MHz (Bansal et al., 2019), we noticed a variation in the pulse profile of PSR B1508+55 with time. We found this feature very intriguing and decided to explore this pulsar in more detail. PSR B1508+55 has been studied using the Very Long Baseline Array and has been found to be a hyperfast pulsar with a speed of about 1000 km s^{-1} (Chatterjee et al., 2005). It is known to be a single component pulsar above 300 MHz (Naidu et al., 2017). In this paper, we study PSR B1508+55 at three LWA1 frequencies: 49.8, 64.5, and 79.2 MHz. We analyze how the pulse profile evolves with frequency and time. The observations used in this study are described in Section 5.2 along with the data reduction methods employed. In Section 5.3, we analyze the changes in the different pulsar characteristics as a function of time. We discuss different ways for the origin of these variations and compare them with results from previous studies of PSR B2217+47 in Section 5.4. We conclude the study by summarizing our results in Section 5.5.

5.2 Observations and Data reduction

The LWA1 (Taylor et al., 2012) is a radio telescope array located near the Karl G. Jansky Very Large Array in central New Mexico. It consists of 256 dual-polarization dipole antennas operating in the frequency range of 10 to 88 MHz. The outputs of the dipoles can be formed into four fully independent dual-polarization beams. Each beam has two independent frequency tunings (chosen from the range of 10 – 88

MHz), each tuning with a bandwidth of up to 19.6 MHz. The ability of the LWA1 to observe multiple frequencies simultaneously provides a powerful tool for studying the frequency dependence of pulsar profiles (eg. Ellingson et al., 2013).

The LWA Pulsar Data Archive⁴ (Stovall et al., 2015) contains reduced data products for over 100 pulsars (Stovall et al., in prep) observed since 2011. The data products used for this study were produced by coherently de-dispersing and folding the raw LWA1 data using DSPSR⁵. We used archival observations at three frequencies: 49.8, 64.5, and 79.2 MHz with a bandwidth of 19.6 MHz. The archival data consists of 4096 phase bins, 30 s sub-integrations time sections, and 512 frequency channels. We excise RFI using a PSRCHIVE median zapping algorithm. It removes data points with an intensity more than six times compared to the median within a range of frequency channels. We then process this data in two different ways to obtain profile evolution and dispersion measure (DM) evolution over time.

5.2.1 Average pulse profile evolution

For this purpose, we average all the frequency channels and reduce the number of phase bins to 512 to smooth the average profiles. These tasks are performed using the PSRCHIVE command `pam` (van Straten et al., 2012). To further enhance the signal to noise ratio (S/N) of the trailing component, we average the data across epochs using a sliding window average with a width of three. We remove the offset baseline from the average profiles and then normalize them by their maximum amplitude at all frequencies. These normalized profiles are cross-correlated with a reference profile such that profiles at all the epochs are aligned with each other. We assume that flux density of this source is constant and the component separation is independent of the absolute flux value of pulsar. Moreover, these are archival observations, thus obtaining flux calibration is not possible.

We derive the reference profiles from higher frequency data at 79.2 (LWA1), 143,

⁴<https://lda10g.alliance.unm.edu/PulsarArchive/>

⁵<http://dspsr.sourceforge.net/index.shtml>

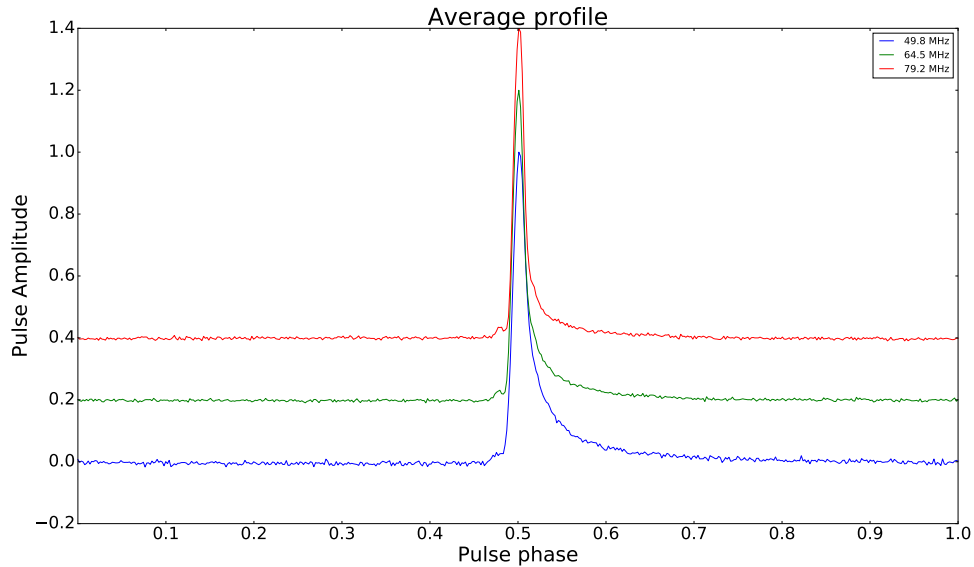


Figure 5.1: Average profiles of PSR B1508+55 at 49.8, 64.5, and 79.2 MHz.

and 151 MHz (EPN⁶). These higher frequency profiles are modeled using a sum of Gaussians as explained in Kramer et al. (1994). Using the width of the Gaussian component, we derive pulse width evolution parameters as a function of frequency. For more details about this technique refer to Bansal et al. (2019). Using these parameters, we obtain reference profiles at 49.8 and 64.5 MHz. To demonstrating the evolution of component separation with time we need to estimate the relative location of the post-cursor. This is why we only fit for the main component in the reference profiles as this is the component to be subtracted. After removing the main component, we fit the post-cursor component using a Gaussian profile. This yields the amplitude, width, and position of the post-cursor component. The position of the main component (its maximum) is subtracted from that of the post-cursor component for all the epochs to obtain the separation between the two.

⁶<http://www.epta.eu.org/epndb/> (Bilous et al., 2016)

Table 1. Ephemeris obtained for PSR B1508+55.

Parameter	Value
RA	$15^h 09^m 25.63^s \pm 0.002$
DEC	$55 : 31 : 32.38 \pm 0.01$
F0 (Hz)	$1.35193283734 \pm 0.00000000006$
F1 (sec^{-2})	$-9.19957\text{D}-15 \pm 8.8\text{D}-20$
POSEPOCH	52275.0000
DM (pc cm^{-3})	19.616

Note: RA - Right Ascension; DEC- Declination; F0 - Pulsar Frequency; F1: Rate of change of F0; DM - Dispersion Measure. Various parameters which were fitted for obtaining a variation in DM using pulsar timing.

5.2.2 DM Evolution

For the DM measurements of PSR B1508+55, the number of frequency channels in the archive files is reduced to 16 for every epoch at all three frequencies using `pam`. We then obtain profile templates by averaging profiles across all the epochs for each frequency using `psradd`, followed by smoothing the profile using `psrsmooth`. Profile templates are aligned in the phase before obtaining the TOAs. Using `pat` (a PSRCHIVE algorithm), we obtain the time of arrivals (TOAs) for these profiles. We combine these TOAs from all three frequencies into one file and then fit for the pulsar's spin, astrometric, and DMX values using the pulsar timing software `TEMPO`⁷ (Table 5.1). These measure an offset of DM from a fiducial value for multiple epochs each having a specified time span. Here, we have used a time span of about three years.

5.3 Variation in PSR B1508+55

In this paper, we explore various features such as the component separation, spectral index, and timing residuals of PSR B1508+55. Below we discuss each of them in more detail.

⁷<http://tempo.sourceforge.net/>

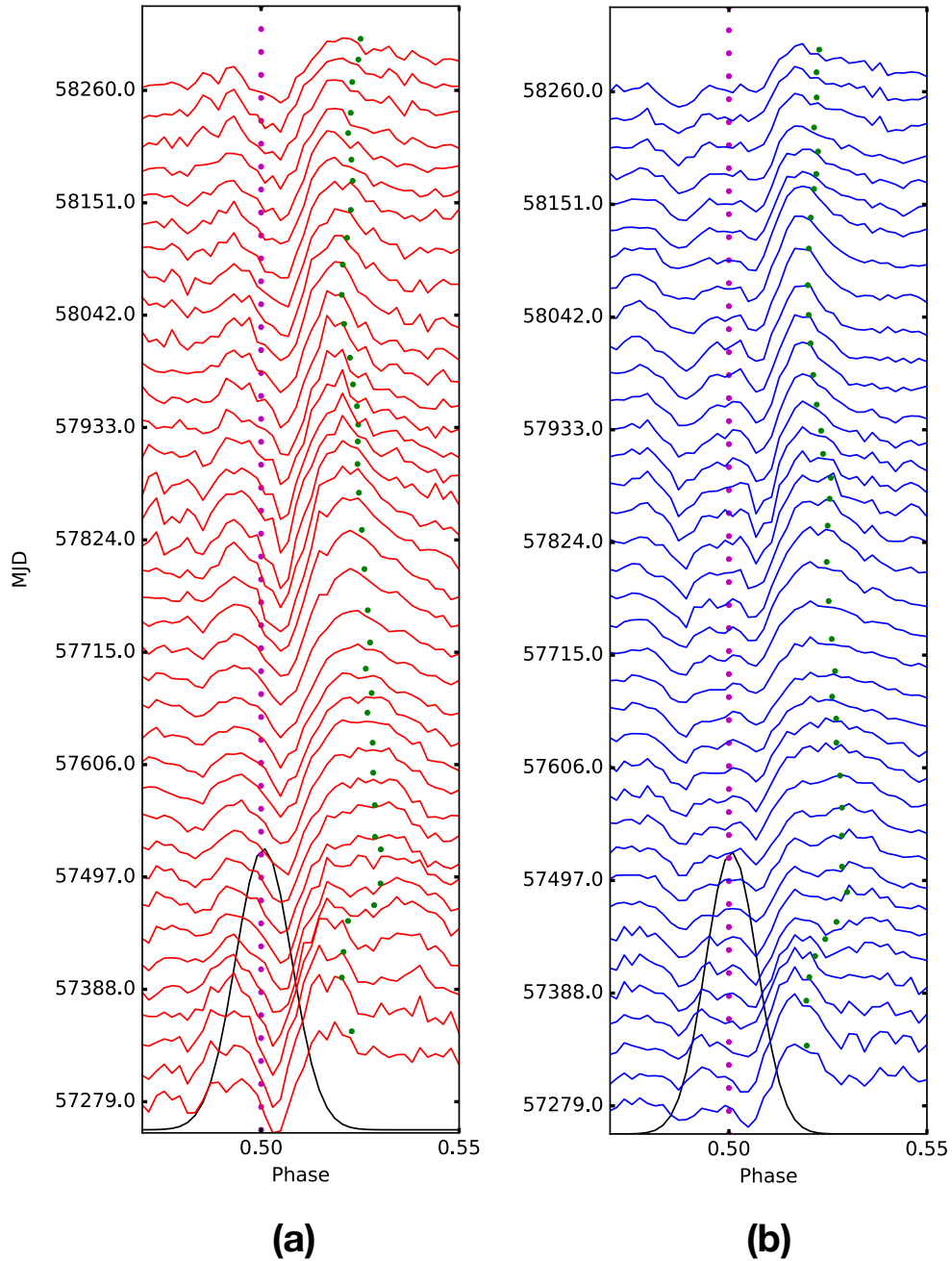


Figure 5.2: Stacked residual profiles at 49.8 MHz (a) and 64.5 MHz (b) from all the available epochs. The reference profile (black) has been subtracted from the original data. The magenta points denote the location of the main component and the green dots denote the location of the trailing component, changing relative to the magenta points with time. For more details see Section 5.3.1.

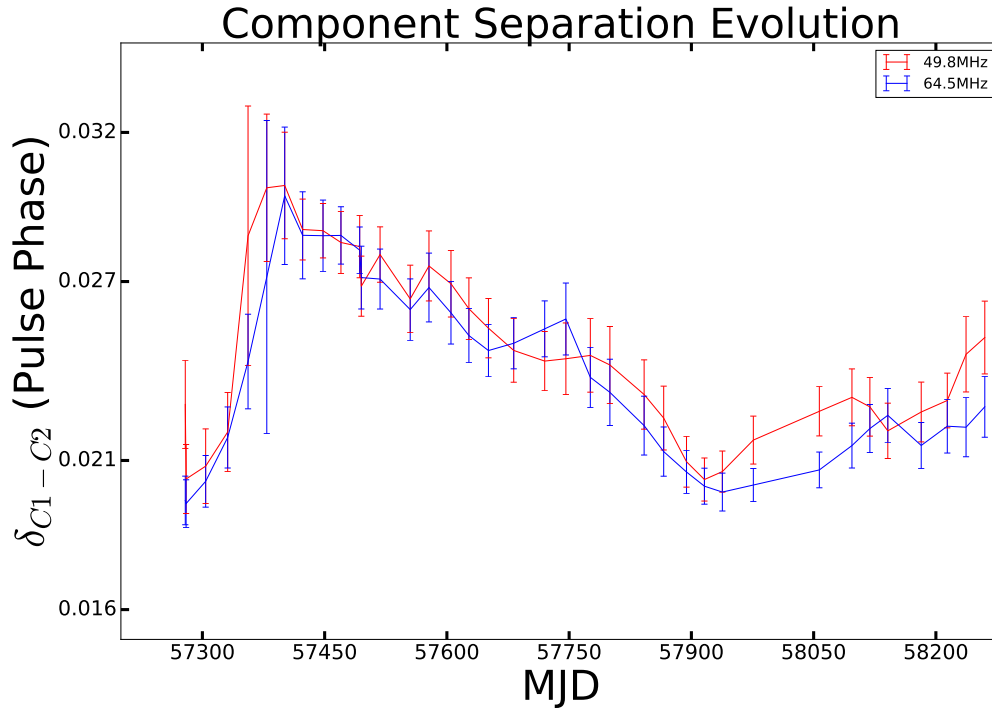
Fig. 5.1 shows averaged profiles at 49.8, 64.5, and 79.2 MHz obtained by averaging profiles at all the epochs available in the LWA1 archive. These profiles show a precursor

component present at all frequencies with no sign of a post-cursor component. The precursor is located about 9° before the main component and is not apparent for an individual epoch. It was detected only after averaging pulse profile over all available epochs. The amplitude of this precursor is about 3% of the main component amplitude, implying that this component is too weak to model accurately. Since it is not changing with time we believe it is intrinsic to the pulsar. Michilli et al. (2018) report a similar weak precursor for PSR B2217+47 at 150 MHz. Its detection at low frequencies is likely due to a broad emission region in the pulsar magnetosphere. This precursor for PSR B1508+55 has not been reported in the literature below 100 MHz.

Fig. 5.2 (a) and (b) show stacked residual profiles at 49.8 and 64.5 MHz. The reference profile (black profile) has been subtracted from the original data. At individual epochs, pulse profiles show a trailing component, which moves relative to the main component. The morphology of the trailing component is complex. It is difficult to determine the exact number of peaks in this component due to its low S/N as compared to the main component. Hence, for the sake of simplicity, we assume it to have one peak which is fitted using a Gaussian. We have cut the phase after 0.55 as we do not detect any other components beyond this point. Magenta colored dots represent the position of the main component and green colored dots have been placed at the location of the fitted trailing component to demonstrate its evolution relative to the main pulse. We note that a Gaussian may not necessarily fit the maxima of the trailing components, as these are not symmetric, unlike a Gaussian profile.

5.3.1 Profile Evolution

The relative amplitude of the second component for both the frequencies remains mostly constant. At all the epochs, the trailing component has a lower amplitude at 64.5 MHz as compared to 49.8 MHz. We find the median value of the relative amplitude to be 0.27 ± 0.02 at 49.8 MHz and 0.19 ± 0.01 at 64.5 MHz. Using these ratios, we estimate the relative spectral index of the trailing component to be



. Figure 5.3: Trailing component separation obtained from subtracting the main pulse component at two frequencies: 49.8 and 64.5 MHz.

-2.53 ± 0.18 , thus implying steep spectra. This is why it has poor S/N at 79.2 MHz and we were unable to include this frequency in this analysis.

We note that this source shows temporal broadening, however, it is difficult to fit for scattering parameters over time. Its pulse profile shows a trailing component at our frequencies and their separation from the main component changes over time. At certain epochs when this trailing component overlaps with the main component, we cannot distinguish the two. We believe that this would certainly affect the estimated component separation.

Fig. 5.3 shows the pulse separation evolution obtained from the pulse subtraction method. At both frequencies, component separation follows a similar trend which confirms the evolution of separation between the two components. Error bars on the pulse separation have been obtained from the least-square fitting algorithm. Michilli et al. (2018) report a paper in preparation as having similar results using LOFAR.

5.3.2 DM Variation

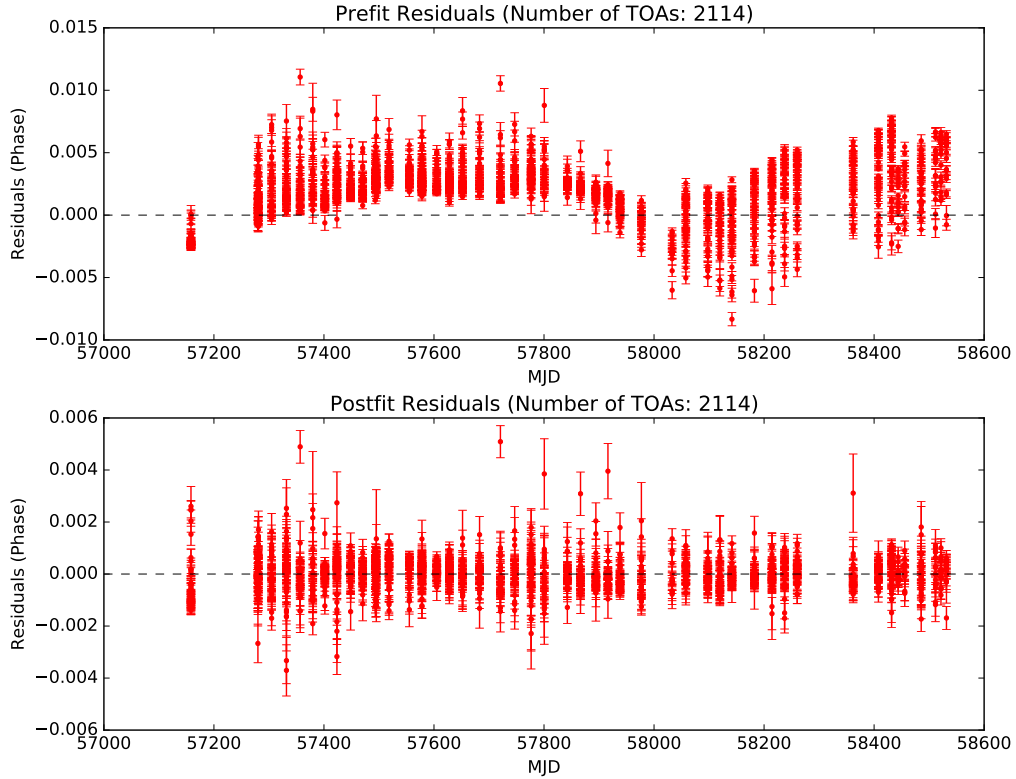


Figure 5.4: Timing Residual before (top) and after (bottom) accounting for the change in DM. The y-axis changes scale by a factor of a little over two between the pre-fit and post-fit panels

Our DM observations show changes in δDM across all three bands – 49.8, 64.5, and 79.2 MHz. Fig. 5.4 shows the timing residuals for this pulsar before and after fitting for the change in DM. Table 5.1 consists of pulsar timing fitting parameters. Fig. 5.4 shows that δDM values over the period of observation. DM values start out almost constant and then there is a gradual decline with the overall change of 6×10^{-3} pc cm^{-3} over 1000 days. We find that this variation is unlikely due to solar winds as the minimum solar elongation angle for this pulsar is 60° . We also note that there is an offset of about 250 days between the decay in δ DM and component separation. This suggests that the DM change is likely independent of the pulse variation.

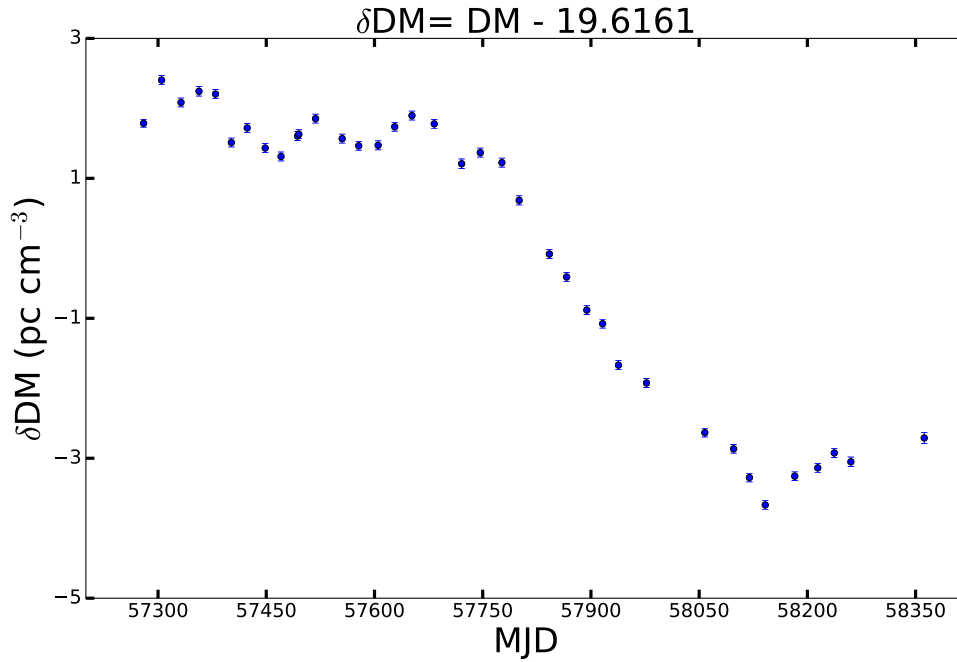


Figure 5.5: Above plot shows δDM variation over time. δDM values represent change in DM compared to the average DM value of $19.616 \text{ pc cm}^{-3}$ for PSR B1508+55. The error bars on δDM values are smaller than the size of the points.

5.4 Discussion

Michilli et al. (2018) discussed three plausible cases for their observation of shifting components in PSR B2217+47. Now we discuss how our results compare with these cases. The first plausible reason is the precession of a pulsar. Pulsar precession takes place when there is a misalignment between the angular momentum vector and the rotation axis. Plausible causes for this alignment include a non-symmetrical surface of the pulsar or a change in the magnetosphere. All the six pulsars studied by Lyne et al. (2010) show variations in their main pulse shape correlated with spin-down rate. We attempted to measure the spin down rate for PSR B1508+55 using a combination of three subsequent epochs. The value of the spin-down rate was constant within the errors.

Fig. 5.4 shows timing residuals for PSR B1508+55 before (top) and after (bottom) accounting for the changes in DM. In Fig. 5.4 top panel, there is no quasi-periodic variation in the timing residuals on the time scales of our measurements as expected

from a variation in spin-down rate due to geodetic precession. It shows that at each epoch the spread in the TOA residuals is due to different DM values as we have included three different frequencies. At some epochs, the TOA residuals clump together, when the DM value is equal to the true DM value. We find that the TOAs residuals are due to changes in DM only.

PSR 1508+55 is an old pulsar (~ 2.3 million years⁸), and thus we would expect the magnetosphere to be more stable as compared to a young pulsar. Moreover, we would expect the effect of both precession and magnetosphere to affect higher frequencies as they are closer to the surface and, in case of PSR B1508+55, no such variation at frequencies above 300 MHz has been observed. This is why both pulsar precession as well as a change in magnetosphere is unlikely to explain our observations.

Another plausible explanation includes the effect of ISM structures. When the pulsar signal travels through the ISM, structures near the line of sight (LOS) can reflect the pulse signal such that it manifests as a trailing component. Detection of the trailing component will depend on the nature of the ISM structure as it would affect the amplitude and spectral nature of the reflected pulse signal. PSR B2217+47, B0531+21, and PSR B1508+55 show similar characteristics where the trailing component moves relative to the main component. However, in the case of PSR B0531+21, it is thought not to be caused by the ISM structure since both the pulsar and the structures causing the echo are both inside the supernova remnant (Lyne et al., 2001).

PSR B1508+55, similar to PSR B2217+47, shows a change in DM of $\sim 6 \times 10^{-3}$ pc cm⁻³ over a period of three years (Fig. 5.5). However, in the case of PSR B2217+47, Michilli et al. (2018) associate it with the pulse profile evolution whereas in our case we see a clear offset of 250 days between the timescale of the two effects. Looking at Figures 4 and 5 in Michilli et al. (2018), it appears that there may be an offset for PSR B2217+47 as well. Another difference is that in case of PSR B2217+47, the

⁸Characteristic Age of a pulsar, $\tau_{age} = \frac{P}{2\dot{P}}$, Lyne (2006)

minimum phase delay between the main component and transient post-cursor is 1 ms at 150 MHz while in the case of PSR B1508+55 is 15.1 ms at 49.8 MHz. Since these observations differ in frequencies where we expect small dispersion at higher frequencies which will imply 9 times larger delay at 49.8 MHz as compared to 150 MHz (delay due to dispersion $\propto (\nu_1/\nu_2)^2$). We expect that the minimum delay will happen at the closest approach of the pulsar and the ISM structure. This could account for the remaining 6-ms delay at LWA frequencies if the closest approaches are different in the two cases. This implies that the change in DM and pulse shape will be correlated when the LOSs aligns. Hence, the observed DM change is likely independent of the pulsar profile change due to a misalignment of the LOS with the ISM structure.

The scattering from the ISM structure affects the amplitude of the pulse signal, and consequently, the amplitude of the trailing component. We compare the ratio of the trailing component amplitude with that of the main component for PSR B1508+55 with PSR B2217+47. We find the median value of the relative amplitude to be 0.27 ± 0.02 at 49.8 MHz and 0.19 ± 0.01 at 64.5 MHz. Using these ratios, we estimate the relative spectral index of the trailing component to be -2.53 ± 0.18 . In the case of PSR B2217+47, the relative spectral index of the trailing component has been found to be -1.60 ± 0.03 . Both observations suggest a steep spectral nature of the trailing component. This is probably why no observations above 300 MHz previously detected the trailing component.

The above discussion suggests that such observations are not intrinsic to the pulsar but due to the interaction of the pulsar signal with ISM. The steep spectral nature of the post-cursor for both pulsars explains our observations at low frequencies. Additionally, low frequencies are highly sensitive to ISM effects which makes them more suitable for this type of study. However, it requires high sensitivity to detect such an effect. In our scattering sample of eight pulsars over a span of three years only PSR B1508+55 shows variation in its component separation over time. The reason is likely due to high scattering at these frequencies, which obscures the trailing component, which makes it probably a rare phenomena.

5.4.1 Properties of ISM structure

From the above discussion, we find that echoes in the case of PSR B1508+55 best explain our observations. Considering this interpretation, we calculate the physical characteristics of this structure below.

We use the pulse delay (τ_d) to estimate the distance of this structure from the Earth. We use the ISM scattering model proposed by Michilli et al. (2018) and use their Equation A7. We fit for this equation using our measured component delay between MJD 57448 and MJD 57916. We use these two epochs as there are turnovers before and after them. The estimated distance between the lens and pulsar is between 220 – 450 pc (X2 in Fig. 5.6). This makes the average distance from Earth to the lens in the ISM about 10% in comparison to the pulsar (2.37 ± 0.23 kpc, refer Chatterjee et al., 2005), implying that the lens is relatively close to the Earth. We note that the large error in pulsar distance makes it difficult to estimate X2 more precisely.

We note that the component delay is roughly symmetric here as compared to the profile evolution presented by Michilli et al. (2018). If the lens causing these echoes was stationary and the pulsar was moving towards it, we would expect to see a decrement in the phase delay and then increment. However, in this case we see that first there is an increment in the phase delay followed by decrement and then a slow increment. This trend suggests that the lens is likely oscillating relative to the pulsar. To further test its periodicity, we would need to study this source over a longer period. We searched for nearby sources along the LOS and remained unable to find any at the estimated distance from Earth.

The ISM lens consists of plasma, which has refractive properties. An average electron density (n_e in cm^{-3}) of the lens can be obtained using the following relation (Hill et al., 2005),

$$n_e = 5.4\theta_r/\lambda^2, \tag{5.1}$$

where θ_r is the refracted angle in mas and λ is the observing wavelength in m. By using the geometrical relations, we estimate the deflection angle ($\delta = \theta_r$) by obtaining all three sides of the triangle (Fig. 5.6). We calculate the third side (X1) of the triangle using the extra path length measurement, traveled by light, using $X1 + X2 - D = \tau_d \times c$. We estimate the deflection angle to be ~ 404 mas. Using both observing frequencies (49.8 and 64.5 MHz), we obtain the electron density to be $\sim 60 - 100 \text{ cm}^{-3}$. This value is of the same order of magnitude as reported in Michilli et al. (2018) and consistent with the extreme scattering event electron density obtained in Hill et al. (2005).

In order for us to see the scattered signal, the angle θ_r (Fig. 5.6) needs to be within our beam size. We calculate this angle to be $0.36''$, which is much smaller than the beam size of LWA1 of 2.5 degrees at 64.5 MHz.

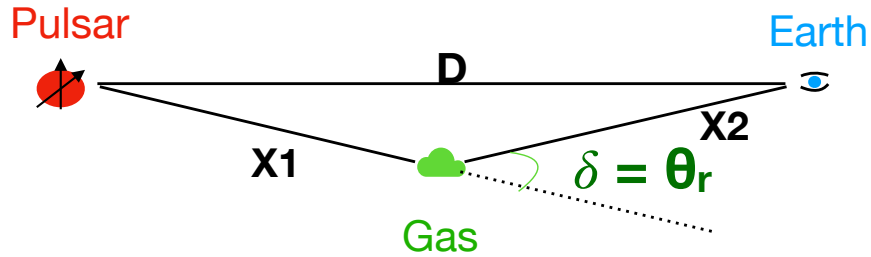


Figure 5.6: A simplified cartoon showing this scattering of pulsar signal from the ISM ionized gas cloud. The main component travels along D and the post-cursor along $X1$ - $X2$. The angle δ is the deflection angle, which is equal to the refractive angle. This figure has been adapted from Michilli et al. (2018).

5.5 Conclusion

In this paper we study pulse profile variation in PSR B1508+55. This variation was discovered serendipitously while studying the scattering for a sample of eight pulsars using the LWA1. We compare our results from Michilli et al. (2018), where they

have observed a similar phenomena for PSR B2217+47. Our analysis of component separation and DM evolution suggests that this observation is result of echoes due to presence of structures in the ISM. We estimate the distance of this structure from the Earth ~ 340 pc with an ionized density of $60 - 100 \text{ cm}^{-3}$. This study suggests that observing pulsars at lower frequencies enables us to explore such structures in the ISM which could be a rare phenomena. We also report on the discovery of a faint precursor component in the profile of PSR B1508+55 below 100 MHz, suggesting a possible broad magnetosphere at lower frequencies.

Chapter 6

Conclusions and Future Work

6.1 Summary

With the goal of detecting nano-Hz gravitational waves using pulsar timing arrays, we have covered two major aspects: their source of emission and reducing the noise in pulsar timing for increasing the chances of their detection using PTAs. We have observed and studied two very diverse sources: supermassive binary black holes (SMBBHs) and pulsars. Now, we reflect on the results we have obtained during this study.

Orbital Motion of 0402+379 We have searched for many SMBBHs, and so far 0402+379 is the only confirmed SMBBH. In Chapter 2, we have studied this source at multiple frequencies for a time span of about 12 years. We have obtained the orbital motion of its core components and estimated the combined mass to be $9 \times 10^9 M_{\odot}$ and the orbital period to be 28000 yr. Using the multi-frequency observations of this source, we also measured the core-shift effect for the jets originating from C2. We estimated the magnetic field near the base of the jet to be ~ 1 Gauss.

Searching for more SMBBHs: The above estimated orbital period is too long for astronomers to obtain the entire orbital motion within their lifetime. This is why we carried out a search for compact SMBBH candidates. In Chapter 3, we selected a

sample of 19 sources and studied them using the VLBA. Unfortunately, we found no new SMBBHs. Although it is a bit disheartening, it encourages us to understand them in more detail. This also raises the issue of why there are so few SMBBHs detected.

Scattering Study: SMBBHs are expected to emit GWs in the frequency range of nano-hertz. While the pulsar timing arrays attempt to improve their sensitivity by continuously monitoring millisecond pulsars (MSPs), there is a simultaneous need to understand their noise sources. One of the biggest timing noise contributors is the interstellar medium (ISM) due to its turbulent nature. The ISM introduces both chromatic and white noise. To probe the ISM, we have studied pulsar scattering in seven sources using the LWA1, as described in Chapter 4. To obtain the scattering index, we have developed software which deconvolves the expected pulse profile from the exponential scattering function. This is the first time a systematic variation in the scattering index over time has been reported. Our results suggest that the scattering index for the majority of sources in our sample remains constant except for PSR B2217+47. In the case of this pulsar, we measure a decrement in scattering spectral index over our observation period of three years. We simultaneously study a change in its DM which anti-correlates with the trend in scattering spectral index. This suggests that there is an ionized gas cloud along the path to the pulsar.

We measure the mean scattering index for the remaining pulsars. In most of the cases, there is a clear deviation from the theoretically expected value of 4 and 4.4. These deviations imply limitations of the thin-screen model with alternative explanations such as finite screen, anisotropic scattering, anomalous scattering, and the effect of inner scale effects at low frequencies. It suggests that the current scattering model, needs to be modified to accommodate these deviations.

In Chapter 5, we study the scattering in PSR B1508+55, where we see a variation in the separation between the main component and the trailing component over a span of three years. This observation is likely an effect of refraction off of an ionized gas cloud along the line of sight. We find its electron density to be 100 cm^{-3} and distance to the cloud to be about 400 pc.

We hope this understanding of scattering will help us improve the ISM models. This will help the PTA community to attain a better sensitivity.

6.2 Future Work

6.2.1 Search for SMBBHs

SMBBHs are rare and difficult to detect. A non-detection of SMBBHs in this study, emphasizes the need to develop approaches for their systematic search. Since only 10% of the quasars are radio loud, it implies that a multi-frequency approach extending to other frequencies such as optical or gamma-rays would be worth pursuing. Several SMBBH candidates have been identified using the double-peaked broad lines or by detecting a periodic variation in optical flux. We suggest that future searches should use a combination of multi-frequencies to select an initial sample and then observe them using the VLBI techniques.

We need to observe at least a thousand sources to identify one SMBBH candidate. New telescopes such as the Square Kilometer Array or the next generation Very Large Array (ngVLA) with their large collecting area will survey these sources faster. The long baselines of the proposed ngVLA will be useful to attain the required resolution.

A detection of GWs with PTAs will certainly confirm the supermassive black hole mergers as well as it will provide the timescale scale of their evolution. This can be used to determine the current evolution stage of a SMBBH. This will enable us to have a focused approach instead of blind surveys.

6.2.2 Role of Magnetic Field

In this thesis, we observed a sample of 19 sources to search for SMBBH. By comparing our observations with those at lower and higher frequencies, we can probe their morphologies based on their source structure and understand their properties. As we

have observed these sources at two radio frequencies, their core-shift effect can be used to measure the magnetic field intensity near the base of the jet. However, this would be limited to compact symmetric objects only. We can compare these values with archival observations, and see if there is any variation in the magnetic field over time. This would help us investigate the role of the magnetic field in jet dynamics.

6.2.3 Science at Low Frequencies

Scattering Study of MSPs: LWA is a unique system as it operates at frequencies below 100 MHz. This ability of LWA can be used to pursue various science goals which would not be possible with any other instrument. In this thesis, we obtained scattering measurements for normal pulsars using the LWA1. This study can be further extended by applying the same techniques to MSPs, which are the prime candidates of PTAs. In the case of PTAs, MSPs are used at frequencies above 1 GHz, where the effect of the ISM is weak. Thus, studying MSPs at low frequencies will enable us to probe the ISM along their line of sight.

Scintillation Measurements: LWA can be used to study scintillation for nearby pulsars. As mentioned earlier in Chapter 1 that scintillation arcs can help us probe the scale of inhomogeneities in the ISM. However, due to the large phase deviations at low frequencies, it is difficult to detect scintles. We have searched for scintles in several nearby pulsars using the LWA1, and have detected them in two sources. Currently, LWA has two operating stations and by combining their data, scintillation can be obtained with high S/N. These can later be used to obtain scintillation arcs.

Search for pulsars in globular clusters: Since LWA operates at low frequencies, DM can be measured very precisely. This can be used to measure the electron density of globular clusters by studying pulsars inside them. Globular clusters have a high density of stars which also increases the probability of finding binaries in them. However, as the signal travels through the ISM, it gets scattered, and as a result, its intensity is reduced. This makes the study of globular clusters at low frequencies very difficult due to their large distance from the Earth. If we successfully detect pulsars

in globular clusters, their timing residuals can be used to measure a change in DM over time. This will enable us to explore the physical properties of globular clusters and their evolutionary history.

References

- B. P. Abbott, R. Abbott, T. Abbott, M. Abernathy, F. Acernese, K. Ackley, C. Adams, T. Adams, P. Addesso, R. Adhikari, et al. Observation of gravitational waves from a binary black hole merger. *Physical review letters*, 116(6):061102, 2016. 17, 53
- K. Akiyama, A. Alberdi, W. Alef, K. Asada, R. Azulay, A.-K. Baczko, D. Ball, M. Baloković, J. Barrett, D. Bintley, et al. First m87 event horizon telescope results. iv. imaging the central supermassive black hole. *The Astrophysical Journal Letters*, 875(1):L4, 2019. 19, 53
- P. Amaro-Seoane, S. Aoudia, S. Babak, P. Binetruy, E. Berti, A. Bohé, C. Caprini, M. Colpi, N. J. Cornish, K. Danzmann, et al. elisa: Astrophysics and cosmology in the millihertz regime. *arXiv preprint arXiv:1201.3621*, 2012. 28, 53
- F. Andrade-Santos, Á. Bogdán, R. W. Romani, W. R. Forman, C. Jones, S. S. Murray, G. B. Taylor, and R. T. Zavala. Binary black holes, gas sloshing, and cold fronts in the x-ray halo hosting 4c+ 37.11. *The Astrophysical Journal*, 826(1):91, 2016. 28, 36, 38
- R. Archibald, V. Kaspi, A. Beardmore, N. Gehrels, and J. A. Kennea. On the braking index of the unusual high-b rotation-powered pulsar psr j1846–0258. *The Astrophysical Journal*, 810(1):67, 2015. 4
- P. J. Armitage and P. Natarajan. Eccentricity of supermassive black hole binaries coalescing from gas-rich mergers. *The Astrophysical Journal*, 634(2):921, 2005. 36
- J. Armstrong, B. Rickett, and S. Spangler. Electron density power spectrum in the local interstellar medium. 1994. 12

- Z. Arzoumanian, A. Brazier, S. Burke-Spolaor, S. J. Chamberlin, S. Chatterjee, B. Christy, J. M. Cordes, N. J. Cornish, K. Crowter, P. B. Demorest, et al. The nanograv nine-year data set: limits on the isotropic stochastic gravitational wave background. *The Astrophysical Journal*, 821(1):13, 2016. 21, 28
- Z. Arzoumanian, P. Baker, A. Brazier, S. Burke-Spolaor, S. Chamberlin, S. Chatterjee, B. Christy, J. M. Cordes, N. J. Cornish, F. Crawford, et al. The nanograv 11 year data set: Pulsar-timing constraints on the stochastic gravitational-wave background. *The Astrophysical Journal*, 859(1):47, 2018. 65
- W. Baade and F. Zwicky. Cosmic rays from super-novae. *Proceedings of the National Academy of Sciences*, 20(5):259–263, 1934. 2
- K. Bansal, G. B. Taylor, A. Peck, R. T. Zavala, and R. W. Romani. Constraining the orbit of the supermassive black hole binary 0402+ 379. *The Astrophysical Journal*, 843(1):14, 2017. 53
- K. Bansal, G. Taylor, K. Stovall, and J. Dowell. Scattering study of pulsars below 100 mhz using lwa1. *The Astrophysical Journal*, 875(2):146, 2019. 93, 95
- J. E. Barnes. Formation of gas discs in merging galaxies. *Monthly Notices of the Royal Astronomical Society*, 333(3):481–494, 2002. 26
- N. Bartel, D. Morris, W. Sieber, and T. Hankins. The mode-switching phenomenon in pulsars. *The Astrophysical Journal*, 258:776–789, 1982. 75
- S. D. Bates, D. R. Lorimer, and J. P. Verbiest. The pulsar spectral index distribution. *Monthly Notices of the Royal Astronomical Society*, 431(2):1352–1358, 2013. 7
- M. C. Begelman, R. D. Blandford, and M. J. Rees. Massive black hole binaries in active galactic nuclei. *Nature*, 287(5780):307, 1980. 20, 26, 53
- A. Bilous, V. Kondratiev, M. Kramer, E. Keane, J. Hessels, B. Stappers, V. Malofeev, C. Sobey, R. Breton, S. Cooper, et al. A lofar census of non-recycled pulsars: average profiles, dispersion measures, flux densities, and spectra. *Astronomy & Astrophysics*, 591:A134, 2016. 7, 95

- R. Blandford and A. Königl. Relativistic jets as compact radio sources. *The Astrophysical Journal*, 232:34–48, 1979. 31
- W. F. Brisken, J.-P. Macquart, J.-J. Gao, B. Rickett, W. Coles, A. Deller, S. Tingay, and C. West. 100 μ as resolution vlbi imaging of anisotropic interstellar scattering toward pulsar b0834+ 06. *The Astrophysical Journal*, 708(1):232, 2009. 16
- P. Brook, A. Karastergiou, S. Buchner, S. Roberts, M. Keith, S. Johnston, and R. Shannon. Evidence of an asteroid encountering a pulsar. *The Astrophysical Journal Letters*, 780(2):L31, 2013. 93
- S. Burke-Spolaor. A radio census of binary supermassive black holes. *Monthly Notices of the Royal Astronomical Society*, 410(4):2113–2122, 2011. 26, 38, 53
- S. Callegari, L. Mayer, S. Kazantzidis, M. Colpi, F. Governato, T. Quinn, and J. Wadsley. Pairing of supermassive black holes in unequal-mass galaxy mergers. *The Astrophysical Journal Letters*, 696(1):L89, 2009. 26
- S. Callegari, S. Kazantzidis, L. Mayer, M. Colpi, J. M. Bellovary, T. Quinn, and J. Wadsley. Growing massive black hole pairs in minor mergers of disk galaxies. *The Astrophysical Journal*, 729(2):85, 2011. 26
- S. Chandrasekhar. The maximum mass of ideal white dwarfs. *The Astrophysical Journal*, 74:81, 1931. 2
- S. Chatterjee, W. Vlemmings, W. Brisken, T. Lazio, J. Cordes, W. Goss, S. Thorsett, E. Fomalont, A. Lyne, and M. Kramer. Getting its kicks: a vlba parallax for the hyperfast pulsar b1508+ 55. *The Astrophysical Journal Letters*, 630(1):L61, 2005. 93, 104
- J. Chen, H. Wang, N. Wang, A. Lyne, Z. Liu, A. Jessner, J. Yuan, and M. Kramer. Long-term monitoring of mode switching for psr b0329+ 54. *The Astrophysical Journal*, 741(1):48, 2011. 75
- J. M. Cordes and T. J. W. Lazio. Ne2001. i. a new model for the galactic distribution of free electrons and its fluctuations. *arXiv preprint astro-ph/0207156*, 2002. 8, 64

- J. M. Cordes and R. Shannon. Rocking the lighthouse: Circumpulsar asteroids and radio intermittency. *The Astrophysical Journal*, 682(2):1152, 2008. 92
- J. M. Cordes and T. J. W. Lazio. Anomalous radio-wave scattering from interstellar plasma structures. *The Astrophysical Journal*, 549(2):997, 2001. 65, 86
- J. Cordes. Space velocities of radio pulsars from interstellar scintillations. *The Astrophysical Journal*, 311:183–196, 1986. 15
- J. Cordes, J. Weisberg, and V. Boriakoff. Small-scale electron density turbulence in the interstellar medium. *The Astrophysical Journal*, 288:221–247, 1985. 15
- J. M. Cordes. Observational limits on the location of pulsar emission regions. *The Astrophysical Journal*, 222:1006–1011, 1978. 6
- J. Cuadra, P. Armitage, R. Alexander, and M. Begelman. Massive black hole binary mergers within subparsec scale gas discs. *Monthly Notices of the Royal Astronomical Society*, 393(4):1423–1432, 2009. 20, 36
- M. Daszuta, W. Lewandowski, and J. Kijak. Scintillation observations of psr b0823+26. *Monthly Notices of the Royal Astronomical Society*, 436(3):2492–2499, 2013. 84, 86
- R. Deane, Z. Paragi, M. Jarvis, M. Coriat, G. Bernardi, R. Fender, S. Frey, I. Heywood, H.-R. Klöckner, K. Grainge, et al. A close-pair binary in a distant triple supermassive black hole system. *Nature*, 511(7507):57, 2014. 28, 38
- M. Dotti, A. Sesana, and R. Decarli. Massive black hole binaries: dynamical evolution and observational signatures. *Advances in Astronomy*, 2012, 2012. 27
- M. Dotti, M. Colpi, F. Haardt, and L. Mayer. Supermassive black hole binaries in gaseous and stellar circumnuclear discs: orbital dynamics and gas accretion. *Monthly Notices of the Royal Astronomical Society*, 379(3):956–962, 2007. 26
- A. Einstein. Näherungsweise Integration der Feldgleichungen der Gravitation. *Sitzungsberichte der Königlich Preußischen Akademie der Wissenschaften (Berlin)*, Seite 688-696., 1916. 27

- A. Einstein. Über Gravitationswellen. *Sitzungsberichte der Königlich Preussischen Akademie der Wissenschaften (Berlin)*, Seite 154-167., 1918. 27
- S. Ellingson, G. Taylor, J. Craig, J. Hartman, J. Dowell, C. Wolfe, T. Clarke, B. Hicks, N. Kassim, P. Ray, et al. The lwa1 radio telescope. *IEEE Transactions on Antennas and Propagation*, 61(5):2540–2549, 2013. 66, 94
- A. Escala, R. B. Larson, P. S. Coppi, and D. Mardones. The role of gas in the merging of massive black holes in galactic nuclei. i. black hole merging in a spherical gas cloud. *The Astrophysical Journal*, 607(2):765, 2004. 20, 26
- A. Escala, R. B. Larson, P. S. Coppi, and D. Mardones. The role of gas in the merging of massive black holes in galactic nuclei. ii. black hole merging in a nuclear gas disk. *The Astrophysical Journal*, 630(1):152, 2005. 27
- R. D. Ferdman, R. van Haasteren, C. G. Bassa, M. Burgay, I. Cognard, A. Corongiu, N. D’Amico, G. Desvignes, J. W. Hessels, G. H. Janssen, et al. The european pulsar timing array: current efforts and a leap toward the future. *Classical and Quantum Gravity*, 27(8):084014, 2010. 65
- E. B. Fomalont. Image analysis. In *Synthesis Imaging in Radio Astronomy II*, volume 180, page 301, 1999. 30
- R. Gangadhara and Y. Gupta. Understanding the radio emission geometry of psr b0329+ 54. *The Astrophysical Journal*, 555(1):31, 2001. 74
- M. Geyer and A. Karastergiou. The frequency dependence of scattering imprints on pulsar observations. *Monthly Notices of the Royal Astronomical Society*, 462(3): 2587–2602, 2016. 65, 86
- M. Geyer, A. Karastergiou, V. I. Kondratiev, K. Zagkouris, M. Kramer, B. W. Stappers, J.-M. Grießmeier, J. W. Hessels, D. Michilli, M. Pilia, et al. Scattering analysis of lofar pulsar observations. *Monthly Notices of the Royal Astronomical Society*, 470(3):2659–2679, 2017. 16

- M. Gitti, M. Giroletti, G. Giovannini, L. Feretti, and E. Liuzzo. A candidate supermassive binary black hole system in the brightest cluster galaxy of rbs 797. *Astronomy & Astrophysics*, 557:L14, 2013. 28, 38
- T. Gold. Rotating neutron stars as the origin of the pulsating radio sources. *Nature*, 218(5143):731, 1968. 2
- J. Han, J. Han, L.-X. Peng, D.-Y. Tang, J. Wang, J.-Q. Li, C. Wang, Y.-Z. Yu, and B. Dong. Jiamusi pulsar observations: I. abnormal emission events of psr b0919+06. *Monthly Notices of the Royal Astronomical Society*, 456(4):3413–3421, 2016. 77
- K. Hayasaki. A new mechanism for massive binary black-hole evolution. *Publications of the Astronomical Society of Japan*, 61(1):65–74, 2009. 27
- D. Helfand, R. Manchester, and J. Taylor. Observations of pulsar radio emission. iii-stability of integrated profiles. *The Astrophysical Journal*, 198:661–670, 1975. 91
- R. Hellings and G. Downs. Upper limits on the isotropic gravitational radiation background from pulsar timing analysis. *The Astrophysical Journal*, 265:L39–L42, 1983. 22
- J. W. Hessels, S. M. Ransom, I. H. Stairs, P. C. Freire, V. M. Kaspi, and F. Camilo. A radio pulsar spinning at 716 hz. *Science*, 311(5769):1901–1904, 2006. 4
- A. Hewish, S. J. Bell, J. D. Pilkington, P. F. Scott, and R. A. Collins. Observation of a rapidly pulsating radio source. *Nature*, 217(5130):709, 1968. 2
- A. S. Hill, D. R. Stinebring, C. T. Asplund, D. E. Berwick, W. B. Everett, and N. R. Hinkel. Deflection of pulsar signal reveals compact structures in the galaxy. *The Astrophysical Journal Letters*, 619(2):L171, 2005. 104, 105
- K. Hirotani. Kinetic luminosity and composition of active galactic nuclei jets. *The Astrophysical Journal*, 619(1):73, 2005. 34
- G. Hobbs, A. Lyne, and M. Kramer. An analysis of the timing irregularities for 366 pulsars. *Monthly Notices of the Royal Astronomical Society*, 402(2):1027–1048, 2010. 92

- M. Janssen, R. Schulmann, J. Illy, C. Lehner, and D. Kormos Buchwald. The collected papers of albert einstein. vol. 7: The berlin years: Writings, 1918–1921, 2002. 27
- F. Jenet, S. Anderson, and T. Prince. Single-pulse characteristics of the millisecond radio pulsar psr b1937+ 21 at 430 mhz. *The Astrophysical Journal*, 546(1):394, 2001. 23
- F. A. Jenet and J. D. Romano. Understanding the gravitational-wave hellings and downs curve for pulsar timing arrays in terms of sound and electromagnetic waves. *American Journal of Physics*, 83(7):635–645, 2015. xiv, 22
- A. Karastergiou, S. J. Roberts, S. Johnston, H.-j. Lee, P. Weltevrede, and M. Kramer. A transient component in the pulse profile of psr j0738- 4042. *Monthly Notices of the Royal Astronomical Society*, 415(1):251–256, 2011. 93
- M. Keith, W. Coles, R. Shannon, G. Hobbs, R. Manchester, M. Bailes, N. Bhat, S. Burke-Spolaor, D. Champion, A. Chaudhary, et al. Measurement and correction of variations in interstellar dispersion in high-precision pulsar timing. *Monthly Notices of the Royal Astronomical Society*, 429(3):2161–2174, 2012. 92
- F. M. Khan, A. Just, and D. Merritt. Efficient merger of binary supermassive black holes in merging galaxies. *The Astrophysical Journal*, 732(2):89, 2011. 27
- F. M. Khan, K. Holley-Bockelmann, P. Berczik, and A. Just. Supermassive black hole binary evolution in axisymmetric galaxies: the final parsec problem is not a problem. *The Astrophysical Journal*, 773(2):100, 2013. 20
- F. M. Khan, D. Fiacconi, L. Mayer, P. Berczik, and A. Just. Swift coalescence of supermassive black holes in cosmological mergers of massive galaxies. *The Astrophysical Journal*, 828(2):73, 2016. 20, 27
- P. Kharb, D. V. Lal, and D. Merritt. A candidate sub-parsec binary black hole in the seyfert galaxy ngc 7674. *Nature Astronomy*, 1(10):727, 2017. 56, 57

- F. Kirsten, N. Bhat, B. Meyers, J.-P. Macquart, S. Tremblay, and S. Ord. Probing pulsar scattering between 120 and 280 mhz with the mwa. *arXiv preprint arXiv:1903.02087*, 2019. [xiv](#), [13](#)
- B. Kiziltan, A. Kottas, M. De Yoreo, and S. E. Thorsett. The neutron star mass distribution. *The Astrophysical Journal*, 778(1):66, 2013. [2](#)
- A. Klein, E. Barausse, A. Sesana, A. Petiteau, E. Berti, S. Babak, J. Gair, S. Aoudia, I. Hinder, F. Ohme, et al. Science with the space-based interferometer elisa: Supermassive black hole binaries. *Physical Review D*, 93(2):024003, 2016. [28](#)
- J. Kormendy and L. C. Ho. Coevolution (or not) of supermassive black holes and host galaxies. *Annual Review of Astronomy and Astrophysics*, 51:511–653, 2013. [53](#)
- A. J. Kox, M. J. Klein, and R. Schulmann. The collected papers of albert einstein; volume 6 the berlin years: Writings 1914-1917. *European Journal of Physics*, 18(1):52, 1997. [27](#)
- M. Kramer, R. Wielebinski, A. Jessner, J. Gil, and J. Seiradakis. Geometrical analysis of average pulsar profiles using multi-component gaussian fits at several frequencies. i. method and analysis. *Astronomy and Astrophysics Supplement Series*, 107:515–526, 1994. [69](#), [95](#)
- M. Kramer and D. J. Champion. The european pulsar timing array and the large european array for pulsars. *Classical and Quantum Gravity*, 30(22):224009, 2013. [23](#)
- M. Kramer, K. M. Xilouris, D. R. Lorimer, O. Doroshenko, A. Jessner, R. Wielebinski, A. Wolszczan, and F. Camilo. The characteristics of millisecond pulsar emission. i. spectra, pulse shapes, and the beaming fraction. *The Astrophysical Journal*, 501(1):270, 1998. [7](#)
- M. Krishnakumar, D. Mitra, A. Naidu, B. C. Joshi, and P. Manoharan. Scatter broadening measurements of 124 pulsars at 327 mhz. *The Astrophysical Journal*, 804(1):23, 2015. [67](#), [68](#)

- M. Krishnakumar, B. C. Joshi, and P. Manoharan. Multi-frequency scatter broadening evolution of pulsars. i. *The Astrophysical Journal*, 846(2):104, 2017. 78
- A. Kuzmin and B. Y. Losovsky. Measurements of the scattering of pulsars radio emission. statistical uniformity of large-scale plasma turbulence in the near galaxy. *Astronomical and Astrophysical Transactions*, 26(6):597–604, 2007. 84, 85
- A. Kuzmin, V. Izvekova, Y. P. Shitov, W. Sieber, A. Jessner, R. Wielebinski, A. Lyne, and F. Smith. Catalogue of time aligned profiles of 56 pulsars at frequencies between 102 and 10500 mhz. *Astronomy and Astrophysics Supplement Series*, 127(3):355–366, 1998. 82
- M. T. Lam, J. M. Cordes, S. Chatterjee, M. L. Jones, M. A. McLaughlin, and J. W. Armstrong. Systematic and stochastic variations in pulsar dispersion measures. *The Astrophysical Journal*, 821(1):66, 2016. 87, 89
- H. Lambert and B. Rickett. On the theory of pulse propagation and two-frequency field statistics in irregular interstellar plasmas. *The Astrophysical Journal*, 517(1):299, 1999. 64
- K. R. Lang. Interstellar scintillation of pulsar radiation. *The Astrophysical Journal*, 164:249, 1971. 12
- K. Lazaridis, N. Wex, A. Jessner, M. Kramer, B. Stappers, G. Janssen, G. Desvignes, M. Purver, I. Cognard, G. Theureau, et al. Generic tests of the existence of the gravitational dipole radiation and the variation of the gravitational constant. *Monthly Notices of the Royal Astronomical Society*, 400(2):805–814, 2009. 21
- W. Lewandowski, M. Dembska, J. Kijak, and M. Kowalińska. Pulse broadening analysis for several new pulsars and anomalous scattering. *Monthly Notices of the Royal Astronomical Society*, 434(1):69–83, 2013. 16, 63, 64, 86
- W. Lewandowski, M. Kowalińska, and J. Kijak. The analysis of the largest sample of multifrequency pulsar scatter time estimates. *Monthly Notices of the Royal Astronomical Society*, 449(2):1570–1583, 2015. 16, 63, 64, 86, 87

- K. Liu, E. Keane, K. Lee, M. Kramer, J. Cordes, and M. Purver. Profile-shape stability and phase-jitter analyses of millisecond pulsars. *Monthly Notices of the Royal Astronomical Society*, 420(1):361–368, 2012. 92
- A. Lobanov. Ultracompact jets in agn. *arXiv preprint astro-ph/9712132*, 1997. 29, 31, 32, 33, 34
- O. Löhmer, M. Kramer, D. Mitra, D. Lorimer, and A. Lyne. Anomalous scattering of highly dispersed pulsars. *The Astrophysical Journal Letters*, 562(2):L157, 2001. 16, 63, 64
- O. Löhmer, D. Mitra, Y. Gupta, M. Kramer, and A. Ahuja. The frequency evolution of interstellar pulse broadening from radio pulsars. *Astronomy & Astrophysics*, 425(2):569–575, 2004. 16, 63
- D. R. Lorimer, M. Kramer, et al. *Handbook of pulsar astronomy*, volume 4. Cambridge university press, 2005. 4
- A. Lyne. Pulsar astronomy. pulsar astronomy, by ag lyne and f. graham-smith. *Cambridge astrophysics series. Cambridge, UK: Cambridge University Press*, 2006. xiii, 2, 3, 4, 69, 102
- A. Lyne and B. Rickett. Measurements of the pulse shape and spectra of the pulsating radio sources. *Nature*, 218(5139):326, 1968. 15
- A. Lyne, R. Pritchard, and F. Graham-Smith. Pulsar reflections within the crab nebula. *Monthly Notices of the Royal Astronomical Society*, 321(1):67–70, 2001. 102
- A. Lyne, B. Stappers, P. Freire, J. Hessels, V. Kaspi, B. Allen, S. Bogdanov, A. Brazier, F. Camilo, F. Cardoso, et al. Two long-term intermittent pulsars discovered in the palfa survey. *The Astrophysical Journal*, 834(1):72, 2017. 92
- A. Lyne, G. Hobbs, M. Kramer, I. Stairs, and B. Stappers. Switched magnetospheric regulation of pulsar spin-down. *Science*, 329(5990):408–412, 2010. 92, 101

- R. Manchester. The international pulsar timing array. *Classical and Quantum Gravity*, 30(22):224010, 2013. 23
- R. Manchester, G. Hobbs, M. Bailes, W. Coles, W. van Straten, M. Keith, R. Shannon, N. Bhat, A. Brown, S. Burke-Spolaor, et al. The parkes pulsar timing array project. *Publications of the Astronomical Society of Australia*, 30, 2013. 23, 92
- H. Maness, G. B. Taylor, R. Zavala, A. Peck, and L. Pollack. Breaking all the rules: the compact symmetric object 0402+ 379. *The Astrophysical Journal*, 602(1):123, 2004. xv, 28, 30, 41, 46
- T. Matsubayashi, J. Makino, and T. Ebisuzaki. Orbital evolution of an imbh in the galactic nucleus with a massive central black hole. *The Astrophysical Journal*, 656(2):879, 2007. 36
- N. J. McConnell, C.-P. Ma, K. Gebhardt, S. A. Wright, J. D. Murphy, T. R. Lauer, J. R. Graham, and D. O. Richstone. Two ten-billion-solar-mass black holes at the centres of giant elliptical galaxies. *Nature*, 480(7376):215, 2011. 39
- R. McGary, W. Brisken, A. Fruchter, W. M. Goss, and S. Thorsett. Proper-motion measurements with the vla. i. wide-field imaging and pulse-gating techniques. *The Astronomical Journal*, 121(2):1192, 2001. 31
- M. A. McLaughlin. The north american nanohertz observatory for gravitational waves. *Classical and Quantum Gravity*, 30(22):224008, 2013. 23, 92
- D. Merritt and M. Milosavljević. Massive black hole binary evolution. *Living Reviews in Relativity*, 8(8), 2005. 26, 27
- D. Merritt and E. Vasiliev. Orbits around black holes in triaxial nuclei. *The Astrophysical Journal*, 726(2):61, 2010. 27
- D. Merritt, S. Mikkola, and A. Szell. Long-term evolution of massive black hole binaries. iii. binary evolution in collisional nuclei. *The Astrophysical Journal*, 671(1):53, 2007. 27, 36

- D. Michilli, J. W. Hessels, J. Donner, J. Griebmeier, M. Serylak, B. Shaw, B. Stappers, J. Verbiest, A. Deller, L. Driessen, et al. Low-frequency pulse profile variation in psr b2217+ 47: evidence for echoes from the interstellar medium. *Monthly Notices of the Royal Astronomical Society*, 476(2):2704–2716, 2018. xviii, 82, 88, 93, 98, 99, 101, 102, 104, 105
- M. C. Miller and J. H. Krolik. Alignment of supermassive black hole binary orbits and spins. *The Astrophysical Journal*, 774(1):43, 2013. 37
- M. Milosavljević and D. Merritt. Long-term evolution of massive black hole binaries. *The Astrophysical Journal*, 596(2):860, 2003. 20, 26, 27
- R. Morganti, S. Veilleux, T. Oosterloo, S. H. Teng, and D. Rupke. Another piece of the puzzle: The fast h i outflow in mrk 231. *Astronomy & Astrophysics*, 593:A30, 2016. 57
- A. Naidu, B. C. Joshi, P. Manoharan, and M. KrishnaKumar. Simultaneous multi-frequency single pulse observations of pulsars. *Astronomy & Astrophysics*, 604:A45, 2017. 93
- S. P. O’Sullivan and D. C. Gabuzda. Magnetic field strength and spectral distribution of six parsec-scale active galactic nuclei jets. *Monthly Notices of the Royal Astronomical Society*, 400(1):26–42, 2009. 34
- F. Özel and P. Freire. Masses, radii, and the equation of state of neutron stars. *Annual Review of Astronomy and Astrophysics*, 54:401–440, 2016. 2
- B. Perera, B. Stappers, P. Weltevrede, A. Lyne, and C. Bassa. Understanding the spin-down rate changes of psr b0919+ 06. *Monthly Notices of the Royal Astronomical Society*, 446(2):1380–1388, 2014. 78
- E. Petroff, M. Keith, S. Johnston, W. van Straten, and R. Shannon. Dispersion measure variations in a sample of 168 pulsars. *Monthly Notices of the Royal Astronomical Society*, 435(2):1610–1617, 2013. 87

- M. Pilia, J. Hessels, B. Stappers, V. Kondratiev, M. Kramer, J. Van Leeuwen, P. Weltevrede, A. Lyne, K. Zagkouris, T. Hassall, et al. Wide-band, low-frequency pulse profiles of 100 radio pulsars with lofar. *Astronomy & astrophysics*, 586:A92, 2016. 82
- L. K. Pollack, G. Taylor, and R. Zavala. Vlbi polarimetry of 177 sources from the caltech-jodrell bank flat-spectrum survey. *The Astrophysical Journal*, 589(2):733, 2003. 28
- A. Pushkarev, M. Lister, Y. Kovalev, and T. Savolainen. Apparent parsec-scale jet opening angles and γ -ray brightness of active galactic nuclei. *arXiv preprint arXiv:1205.0659*, 2012. 34, 45
- V. Radhakrishnan and D. Cooke. Magnetic poles and the polarization structure of pulsar radiation. 1969. 6
- J. M. Rankin and N. Rathnasree. Polarization-mode separation and the emission geometry of pulsar 0823+ 26: A new pattern of pulsar emission? *Journal of Astrophysics and Astronomy*, 16(3-4):327–355, 1995. 75
- J. M. Rankin, C. Rodriguez, and G. A. Wright. Bistable profile illumination in pulsars b0919+ 06 and b1859+ 07. *Monthly Notices of the Royal Astronomical Society*, 370(2):673–680, 2006. 77
- V. Ravi, J. Wyithe, R. Shannon, and G. Hobbs. Prospects for gravitational-wave detection and supermassive black hole astrophysics with pulsar timing arrays. *Monthly Notices of the Royal Astronomical Society*, 447(3):2772–2783, 2015. 38
- C. Reynolds, B. Punsly, G. Miniutti, C. P. O’Dea, and N. Hurley-Walker. The relativistic jet-accretion flow–wind connection in mrk 231. *The Astrophysical Journal*, 836(2):155, 2017. 57, 58
- D. Richstone, E. Ajhar, R. Bender, G. Bower, A. Dressler, S. Faber, A. Filippenko, K. Gebhardt, R. Green, L. Ho, et al. Supermassive black holes and the evolution of galaxies. *Nature*, 395(6701):A14–A19, 1998. 26, 52

- B. Rickett, S. Johnston, T. Tomlinson, and J. Reynolds. The inner scale of the plasma turbulence towards psr j1644- 4559. *Monthly Notices of the Royal Astronomical Society*, 395(3):1391–1402, 2009. 64, 65, 86
- B. J. Rickett. Interstellar scattering and scintillation of radio waves. *Annual review of astronomy and astrophysics*, 15(1):479–504, 1977. 12
- B. J. Rickett. Radio propagation through the turbulent interstellar plasma. *Annual review of astronomy and astrophysics*, 28(1):561–605, 1990. 16
- D. H. Roberts, L. F. Brown, and J. F. C. Wardle. Linear polarization sensitive VLBI. In T. J. Cornwell and R. A. Perley, editors, *IAU Colloq. 131: Radio Interferometry. Theory, Techniques, and Applications*, volume 19 of *Astronomical Society of the Pacific Conference Series*, pages 281–288, 1991. 31
- C. Rodriguez, G. B. Taylor, R. Zavala, A. Peck, L. Pollack, and R. Romani. A compact supermassive binary black hole system. *The Astrophysical Journal*, 646(1):49, 2006. xv, 28, 30, 33, 41, 46
- C. Rodriguez, G. Taylor, R. Zavala, Y. Pihlström, and A. Peck. Hi observations of the supermassive binary black hole system in 0402+ 379. *The Astrophysical Journal*, 697(1):37, 2009. 34, 36, 37, 45
- C. Roedig, A. Sesana, M. Dotti, J. Cuadra, P. Amaro-Seoane, and F. Haardt. Evolution of binary black holes in self gravitating discs-dissecting the torques. *Astronomy & Astrophysics*, 545:A127, 2012. 27, 36
- R. W. Romani, R. Narayan, and R. Blandford. Refractive effects in pulsar scintillation. *Monthly Notices of the Royal Astronomical Society*, 220(1):19–49, 1986. 12, 63
- R. W. Romani, W. Forman, C. Jones, S. Murray, A. Readhead, G. B. Taylor, and R. Zavala. A multi-wavelength study of the host environment of smbhb 4c+ 37.11. *The Astrophysical Journal*, 780(2):149, 2013. 37, 38
- P. Scheuer. Amplitude variations in pulsed radio sources. *Nature*, 218(5145):920, 1968. 63

- J. D. Schnittman. Astrophysics of super-massive black hole mergers. *Classical and Quantum Gravity*, 30(24):244007, 2013. 27, 37
- A. Sesana, F. Haardt, and P. Madau. Interaction of massive black hole binaries with their stellar environment. i. ejection of hypervelocity stars. *The Astrophysical Journal*, 651(1):392, 2006. 27
- A. Sesana, F. Haardt, and P. Madau. Interaction of massive black hole binaries with their stellar environment. ii. loss cone depletion and binary orbital decay. *The Astrophysical Journal*, 660(1):546, 2007. 19, 27
- R. M. Shannon, V. Ravi, L. Lentati, P. D. Lasky, G. Hobbs, M. Kerr, R. N. Manchester, W. A. Coles, Y. Levin, M. Bailes, et al. Gravitational waves from binary super-massive black holes missing in pulsar observations. *Science*, 349(6255):1522–1525, 2015. 28, 53, 65
- M. C. Shepherd, T. J. Pearson, and G. B. Taylor. DIFMAP: an interactive program for synthesis imaging. In B. J. Butler and D. O. Muhleman, editors, *Bulletin of the American Astronomical Society*, volume 27 of *BAAS*, page 903, March 1995. 29
- W. Sieber. Pulsar Spectra. *A&A*, 28:237, October 1973. 65
- C. Sobey, N. J. Young, J. W. T. Hessels, P. Weltevrede, A. Noutsos, B. W. Stappers, M. Kramer, C. Bassa, A. G. Lyne, and V. I. Kondratiev. LOFAR discovery of a quiet emission mode in PSR B0823+26. *MNRAS*, 451(3):2493–2506, Aug 2015. doi: 10.1093/mnras/stv1066. 76
- K. Sokolovsky, Y. Kovalev, A. Pushkarev, and A. Lobanov. A vlba survey of the core shift effect in agn jets-i. evidence of dominating synchrotron opacity. *Astronomy & Astrophysics*, 532:A38, 2011. 29, 31, 32, 39
- I. H. Stairs. Pulsar Observations II. – Coherent Dedispersion Polarimetry, and Timing. In S. Stanimirovic, D. Altschuler, P. Goldsmith, and C. Salter, editors, *Single-Dish Radio Astronomy: Techniques and Applications*, volume 278 of *Astronomical Society of the Pacific Conference Series*, pages 251–269, December 2002. 8

- I. Stairs, A. Lyne, and S. Shemar. Evidence for free precession in a pulsar. *Nature*, 406(6795):484, 2000. 92
- I. H. Stairs. Pulsars in binary systems: probing binary stellar evolution and general relativity. *Science*, 304(5670):547–552, 2004. 2
- E. Standish. Jpl planetary and lunar ephemerides, de405/le405 (memo iom 312. f-98-048; pasadena: Jpl), 1998. 73
- B. Stappers, M. Kramer, A. Lyne, N. D’Amico, and A. Jessner. The european pulsar timing array. *Chinese Journal of Astronomy and Astrophysics*, 6(S2):298, 2006. 92
- E. Starovoit and A. Rodin. On the existence of planets around the pulsar psr b0329+54. *Astronomy Reports*, 61(11):948–953, 2017. 75, 88
- K. R. Stewart, J. S. Bullock, R. H. Wechsler, and A. H. Maller. Gas-rich mergers in lcdm: Disk survivability and the baryonic assembly of galaxies. *The Astrophysical Journal*, 702(1):307, 2009. 26
- D. R. Stinebring, B. J. Rickett, and S. K. Ocker. The frequency dependence of scintillation arc thickness in pulsar b1133+16. *The Astrophysical Journal*, 870(2):82, 2019. xiv, 14
- D. R. Stinebring. Scintillation arcs: Probing turbulence and structure in the ism. *Chinese Journal of Astronomy and Astrophysics*, 6(S2):204, 2006. 16
- D. Stinebring, M. McLaughlin, J. Cordes, K. Becker, J. E. Goodman, M. Kramer, J. Sheckard, and C. Smith. Faint scattering around pulsars: probing the interstellar medium on solar system size scales. *The Astrophysical Journal Letters*, 549(1):L97, 2001. 15, 65, 86
- K. Stovall, P. Ray, J. Blythe, J. Dowell, T. Eftekhari, A. Garcia, T. Lazio, M. McCrackan, F. Schinzel, and G. Taylor. Pulsar observations using the first station of the long wavelength array and the lwa pulsar data archive. *The Astrophysical Journal*, 808(2):156, 2015. 66, 67, 82, 94

- C. Tan, C. Bassa, S. Cooper, T. Dijkema, P. Esposito, J. Hessels, V. Kondratiev, M. Kramer, D. Michilli, S. Sanidas, et al. Lofar discovery of a 23.5-second radio pulsar. *arXiv preprint arXiv:1809.00965*, 2018. 5
- G. B. Taylor, S. W. Ellingson, N. E. Kassim, J. Craig, J. Dowell, C. N. Wolfe, J. Hartman, G. Bernardi, T. Clarke, and A. Cohen. First Light for the First Station of the Long Wavelength Array. *Journal of Astronomical Instrumentation*, 1:1250004-284, Dec 2012. doi: 10.1142/S2251171712500043. 66, 93
- G. Taylor, C. Silver, J. Ulvestad, and C. Carilli. The starburst in the central kiloparsec of markarian 231. *The Astrophysical Journal*, 519(1):185, 1999. 57
- G. Taylor. Astrophysics: A tight duo in a trio of black holes. *Nature*, 511(7507):35, 2014. 38
- S. Tremblay, G. Taylor, A. Ortiz, C. Tremblay, J. Helmboldt, and R. Romani. Compact symmetric objects and supermassive binary black holes in the vlba imaging and polarimetry survey. *Monthly Notices of the Royal Astronomical Society*, 459(1): 820–840, 2016. 26, 38, 53
- A. V. Tuntsov, H. E. Bignall, and M. A. Walker. Power-law models of totally anisotropic scattering. *MNRAS*, 429(3):2562–2568, Mar 2013. doi: 10.1093/mnras/sts527. 16
- J. Ulvestad, E. Greisen, and A. Mioduszewski. Aips memo 105: Aips procedures for initial vlba data reduction, 2001. 29
- J. Ulvestad, J. Wrobel, and C. Carilli. Radio continuum evidence for outflow and absorption in the seyfert 1 galaxy markarian 231. *The Astrophysical Journal*, 516 (1):127, 1999. xvi, 57, 60
- G. van Moorsel, A. Kemball, E. Greisen, G. Jacoby, and J. Barnes. Asp conf. ser. vol. 101, astronomical data analysis software and systems v. 1996. 29
- W. van Straten, P. Demorest, and S. Osłowski. Pulsar data analysis with psrchive. *arXiv preprint arXiv:1205.6276*, 2012. 9, 66, 94

- N. Wang, R. Manchester, and S. Johnston. Pulsar nulling and mode changing. *Monthly Notices of the Royal Astronomical Society*, 377(3):1383–1392, 2007. 92
- C. M. Will. Recent publications. *Living Reviews in Relativity*, 17:4, 2014. 2, 21
- I. P. Williamson. Pulse broadening due to multiple scattering in the interstellar medium. *Monthly Notices of the Royal Astronomical Society*, 157(1):55–71, 1972. 10, 68
- S. Xu and B. Zhang. Scatter broadening of pulsars and implications on the interstellar medium turbulence. *The Astrophysical Journal*, 835(1):2, 2017. 84
- W. Xu, A. Readhead, T. Pearson, A. Polatidis, and P. Wilkinson. The first caltech-jodrell bank vlbi survey. iii. vlbi and merlin observations at 5 ghz and vla observations at 1.4 ghz. *Astrophysical Journal Supplement Series*, 99:297–348, 1995. 28
- C.-S. Yan, Y. Lu, X. Dai, and Q. Yu. A probable milli-parsec supermassive binary black hole in the nearest quasar mrk 231. *The Astrophysical Journal*, 809(2):117, 2015. 58
- J. Yao. Manchester rn wang n., 2017. *ApJ*, 835:29. 64
- A. A. Zdziarski, P. Lubiński, and M. Sikora. The mev spectral tail in cyg x-1 and optically thin emission of jets. *Monthly Notices of the Royal Astronomical Society*, 423(1):663–675, 2012. 34
- A. A. Zdziarski, M. Sikora, P. Pjanka, and A. Tchekhovskoy. Core shifts, magnetic fields and magnetization of extragalactic jets. *Monthly Notices of the Royal Astronomical Society*, 451(1):927–935, 2015. 34, 45
- W. Zhu, I. Stairs, P. Demorest, D. J. Nice, J. Ellis, S. Ransom, Z. Arzoumanian, K. Crowter, T. Dolch, R. Ferdman, et al. Testing theories of gravitation using 21-year timing of pulsar binary j1713+ 0747. *The Astrophysical Journal*, 809(1):41, 2015. 21